LAPPEENRANTA
UNIVERSITY OF TECHNOLOGY

MASTER'S THESIS

Ali Halabia

Hyväksytty energia- ja
ympäristötekniikan osaston
osastoneuvoston kokouksessa
8 / 3.06 "4" arvosanalla
"Erittäin hyvä"

LAPPEENRANTA UNIVERSITY OF TECHNOLOGY
Department of Energy and Environmental Technology

DRAG FORCE AND FRICTIONAL RESISTANCES IN VERTICALLY VIBRATED DENSE GRANULAR MEDIA

Supervisor: Professor Piroz Zamankhan
Examiner: Professor Lasse Koskelainen

The Energy and Environmental Technology Department Council has approved the topic of this thesis on 7.9.2005.

Lappeenranta, January 31, 2006

Ali Halabia
Leirikatu 2 C 7, 53600 Lappeenranta
GSM 050-5960567

ABSTRACT

LAPPEENRANTA UNIVERSITY OF TECHNOLOGY
Department of Energy and Environmental Technology

Ali Halabia

DRAG FORCE AND FRICTIONAL RESISTANCES IN VERTICALLY VIBRATED DENSE GRANULAR MEDIA

Thesis for the degree of Master of Science in Technology, 2006

101 pages, 33 figures, 10 tables and 2 appendices

Supervisor: Professor Piroz Zamankhan
Examiner: Professor Lasse Koskelainen

Keywords: granular materials; drag force; vibration; friction

The objective of this thesis is to shed light on the vertical vibration of granular materials for potential interest in the power generation industry. The main focus is investigating the drag force and frictional resistance that influence the movement of a granular material (in the form of glass beads) contained in a vessel, which is subjected to sinusoidal oscillation.

The thesis is divided into three parts: theoretical analysis, experiments and computer simulations. The theoretical part of this study presents the underlying physical phenomena of the vibration of granular materials. Experiments are designed to determine fundamental parameters that contribute to the behavior of vibrating granular media. Numerical simulations include the use of three different software applications: FLUENT, LS-DYNA and ANSYS Workbench. The goal of these simulations is to test theoretical and semiempirical models for granular materials in order to validate their compatibility with the experimental findings, to assist in predicting their behavior, and to estimate quantities that are hard to measure in laboratory.

TIIVISTELMÄ

LAPPEENRANNAN TEKNILLINEN YLIOPISTO
Energia- ja Ympäristötekniikan osasto

Ali Halabia

VASTUSVOIMA JA KITKAVASTUKSET PYSTYSUUNTAISESSA VÄRÄHTELYSSÄ OLEVASSA TIIVIISSÄ RAKEISESSA MATERIAALISSA

Diplomityö, 2006

101 sivua, 33 kuvaa, 10 taulukkoa ja 2 liitettä

Ohjaaja: Professori, TkT Piroz Zamankhan
Tarkastaja: Professori, TkT Lasse Koskelainen

Hakusanat: rakeinen materiaali; vastusvoima; värähtely; kitka

Rakeisilla materiaaleilla on mahdollisia energiateollisuuden sovellutuksia, kuten esimerkiksi leijukerrospoltto. Tämän diplomityön tavoitteena on valaista rakeisen materiaalin käyttäytymistä pystysuuntaisen värähtelyn alaisena. Erityisesti työssä on keskitytty tarkastelemaan vastus- ja kitkavoimia, jotka vaikuttavat rakeisen materiaalin liikkeeseen astiassa, joka on sinimuotoisessa värähtelyliikkeessä.

Diplomityö koostuu kolmesta osasta: teoreettisesta tarkastelusta, kokeellisesta osasta ja tietokonesimulaatioista. Teoriaosassa käsitellään värähtelevään rakeiseen materiaaliin liittyviä fysikaalisia ilmiöitä ja kokeellisessa osassa pyritään vastaavasti määrittelemään perusparametrit, jotka vaikuttavat värähtelyssä olevan rakeisen materiaalin käyttäytymiseen.

Simulaatio-osan numeerisessa laskennassa on käytetty FLUENT, LS-DYNA ja ANSYS Workbench ohjelmistoja. Tämän simulaatio-osan tavoitteena on testata teoreettisten ja puoliempiiristen rakeisen materiaalin mallien soveltuvuutta kokeiden tuloksien avulla. Simulaatioiden tavoitteena on myös ennustaa kyseisten mallien käyttäytymistä ja arvioida suureita joita on vaikea mitata kokeellisesti.

ACKNOWLEDGMENTS

This thesis work has been carried out in the Laboratory of Computational Fluid Dynamics at Lappeenranta University of Technology during the second half of year 2005.

I would like to express my sincere thanks to my supervisors Professor Piroz Zamankhan and Professor Lasse Koskelainen for reviewing this thesis and for their continuous help and professional guidance. I wish to thank Lappeenranta University of Technology for providing me with a stipend and giving me the chance to make this thesis. I am also grateful for Docent Pertti Kolari for the support he has offered. Very kind thanks go to all my friends in Lappeenranta and to my colleagues at the Laboratory of CFD.

I owe my family in Finland and Palestine special warm thanks for their patience, love and encouragement, especially my parents to whom I dedicate this work.

”Mie ite!”
Ali Halabia
Lappeenranta, January, 2006

TABLE OF CONTENTS

NOMENCLATURE 3
1. INTRODUCTION 8
1.1 Motivation and Background 8
1.2 Static and Dynamic Behavior of Granular Materials 10
1.3 Review of Previous Related Work 11
1.4 Objectives and Thesis Structure 13
2. SINGLE-PARTICLE DYNAMICS 15
2.1 Drag Force: A Continuum Approach 15
2.1.1 Drag of Immersed Bodies 15
2.2.2 Fluid Flow Over A Sphere: Friction and Pressure Drag 16
2.2 Drag Force: A Statistical Mechanics Approach 19
2.3 Viscosity 21
2.3.1 Viscosity of Gases 22
2.3.2 Viscosity of Liquids 23
2.3.3 Viscosity of Solids 23
2.4 Elastic Binary Collisions and Hertz Contact Theory 23
2.4.1 Geometry of Solid Surfaces in Contact 24
2.4.2 Hertz Theory of Elastic Contact 28
2.5 Inelastic Binary Collisions 29
2.5.1 The Coefficient of Restitution 29
2.5.2 Experiment Setup for Binary Collision 31
2.5.3 Experiment With The Ultrasonic Motion Detector 34
2.5.4 Analysis of Experiment Results 36
2.5.5 Simple Viscoelastic Material Models 39
2.5.6 Finite Element Analysis 40
3. DYNAMICS OF A SYSTEM OF PARTICLES 46
3.1 General Overview 46
3.2 Vertical Vibration of Granular Materials 46
3.3 Experimental Techniques for Studying Granular Materials 48
3.4 Procedure and Setup of the Vibro-Fluidized Bed Experiment 49

3.5 Experimental Results 53
3.6 Discrete and Continuum Formulation of Granular Flows 57
3.6.1 Introductory Remarks 57
3.6.2 Computer Simulation and Modeling Methods 58
3.6.3 Lagrangian Models 58
3.6.4 Eulerian versus Lagrangian Description of Particle Motion 63
3.6.5 Continuum Theory of Granular Flows 64
3.6.6 Continuum Modeling of Granular Flows 65
3.7 CFD Eulerian Multiphase Model 67
3.7.1 Volume Fractions 67
3.7.2 Governing Conservation Equations 68
3.7.3 Interphase Exchange Coefficient 71
3.7.4 Solids Pressure 74
3.7.5 Solid Shear Stresses 75
3.7.6 Granular Temperature 76
3.7.7 Turbulence Models 76
3.7.8 RSM Dispersed Turbulence Model 77
3.8 CFD Simulations and Results 78
4. MODAL ANALYSIS OF VIBRO-FLUIDIZED BEDS 86
4.1 Background about Modal Analysis 86
4.2 Model Construction in ANSYS Workbench 86
4.3 Results of Modal Simulations 88
5. CONCLUSIONS AND FUTURE WORK 91
5.1 Summary of the Thesis Core Points 91
5.2 Future Research Work 93
REFERENCES 95
APPENDICES

NOMENCLATURE

Symbols

Symbol	Meaning	Units
A	Characteristic area	[m^2]
A	Vertical vibration amplitude	[m]
A, A_1	Positive constants	[–]
a	Radius of contact area	[m]
a	Acceleration	[m/s^2]
B	Horizontal vibration amplitude	[m]
B, B_1	Positive constants	[–]
C_1	Positive constant	[–]
C_D	Drag coefficient	[–]
C_{fric}	Friction coefficient	[–]
d	Diameter	[m]
d	Deformation within contact zone	[m]
E	Elastic modulus	[Pa]
e	Restitution coefficient	[–]
F	Force	[N]
f	Frequency of vibration,	[Hz]
f_D	Model-dependent drag function	[–]
G	Shear modulus	[Pa]
g	Acceleration due to gravity	[m/s^2]
g_0	Radial distribution coefficient	[–]
h	Height	[m]
h	Enthalpy	[J/kg]
h	Separation between two contacting surfaces	[m]
$\bar{\bar{I}}$	Unit tensor	[–]
K	Interphase momentum exchange coefficient	[kg/ m^3·s]
k	Ratio of particle masses in Equation (29)	[–]
k	Turbulence kinetic energy	[m^2/s^2]
k_0	Spring elastic constant	[N/m]
k_B	Boltzmann constant = 1,3807 × 10^{-23} J/K	[J/K]
k_Θ	Diffusion coefficient	[kg/ m·s]
L	Characteristic length	[m]
l	Length of suspension cord in Newton's cradle device	[m]
l	Contact body dimension: laterally and in depth	[m]
m	Mass	[kg]
$\dot{m}$	Mass flow rate	[kg/s]
N	Number of grain layers /particles	[–]
O	Origin	[–]
P	Normal load	[N]
p	Pressure	[Pa]
p_0	Maximum contact pressure	[Pa]
p_m	Average contact pressure	[Pa]
Q	Heat exchange intensity between phases	[W]
q	Heat flux	[W/m^2]

q	Tangential traction (due to friction)	[Pa]
R	Interphase force	[N]
Re	Reynolds number	[—]
Re_s	Relative Reynolds number	[—]
R, R_1' and R_1''	Principal radii of curvature of a surface	[m]
$\tilde{R}$	Reynolds stresses	[Pa]
S	Stress	[Pa]
S	A point on the surface of a contact solid body	[—]
S_q	Source term	[kg/m·s^2], [kg·m/s] etc.
T	Temperature	[K], [ºC]
T	A distant point from origin inside a contact solid body	[—]
t	Time	[s]
u	Velocity	[m/s]
$\overline{u}_z$	Positive displacement of a point on the surface of a contacting solid body parallel to z-axis	[m]
V	Volume	[m^3]
x	Position vector, distance along the x-axis	[m]
x	Coordinate of a point on the x-axis	[—]
x_i	Spatial coordinate in i direction	[m]
y	Position vector, distance along the y-axis	[m]
y	Coordinate of a point on the y-axis	[—]
z	Position vector, distance along the z-axis	[m]
z	Coordinate of a point on the z-axis	[—]
Z	Vertical displacement of vibration	[m]

Greek Letters

Symbol	Meaning	Units
α	Angle of impact particle before collision,	[º]
α	Volume fraction	[—]
β	Angle of impacted particle after collision	[º]
β	Decay constant	[s^{-1}]
δ	Displacement of a point in a contacting solid body	[m]
δ	Infinitesimal quantity like force, velocity…	[—]
ε	Turbulence dissipation rate	[m^2/s^3]
ϕ_{ls}	Energy exchange between phases	[kg/ms^3]
Γ	Dimensionless acceleration	[—]
γ	Viscous contact damping coefficient	[kg/s]
γ_Θ	Collisional dissipation of energy	[kg/ms^3]
λ	Bulk viscosity	[Pa·s]
μ	Dynamic viscosity, Shear viscosity	[Pa·s]
ν	Kinematic viscosity	[m^2/s]
ν	Poisson's ratio	[—]
$\Pi_{R,ij}$	Interaction between continuous phase and dispersed phase turbulences	[m^2/s^3]

π	3.14159	[–]
Θ	Granular temperature	[m^2/s^2]
θ	Step function	[–]
ρ	Physical density, Bulk density	[kg/m^3]
$\hat{\rho}_q$	Effective density of phase q	[kg/m^3]
τ	Shear stress	[Pa]
τ	Particulate relaxation time	[s]
$\bar{\bar{\tau}}$	Stress-strain tensor	[Pa]
υ	Velocity	[m/s]
$\upsilon_{r,s}$	Solid phase terminal velocity correlation	[–]
ω	Angular frequency of vibration	[rad/s]

Subscripts

Subscript	Meaning
∞	Long-time (infinite)
0	Short-time
1	First particle or contact surface
2	Second particle or contact surface
air	Interstitial air
bed	Granular bed
c	Critical
col	Collision
D	Drag
f	Fill
fric	Friction
glass	Glass beads
i	Particle *i*
imp	Impact
j	Particle *j*
kin	Kinetic
Lift	Lift (force)
l	Fluid or solid phase, l^{th} phase
ls	Between fluid or solid phase *l* and solid phase *s*
ℓ	Layer
p	Peak
p	Phase *p* in a multiphase model
particle	Single glass bead
pq	From phase *p* to phase *q*
press	Pressure
q	Phase *q* in a multiphase model
qp	From phase *q* to phase *p*

qq	Between the *q* phases
rq	Reference (density) of phase *q*
s	s^{th} solid phase
vm	Virtual mass
x	Parallel to the *x*-axis direction
y	Parallel to the *y*-axis direction
yx	*y*-*x* plane or surface

Superscripts

Superscript	Meaning
' (prime)	Velocity after collision
$\bar{}$ (over-bar)	Average, time-averaged variable
→	Vector
· (dot)	Rate of change
n (in summation)	Upper summation limit defining the nth phase
ˆ (over-hat)	Effective, in relation to density
N (in summation)	Upper summation limit defining the total number of phases
T	Transposition of a vector or matrix.
~ (tilde)	Phase averaged variable
* (star)	Modified elastic modulus (*E*)

Acronyms

Acronym	Meaning
BOP	Bond Order Potentials
CFB	Conventional Fluidized Bed
CFD	Computational Fluid Dynamics
CGM	Conjugate-Gradient Method
CM	Continuum Mechanics
CPU	Central Processing Unit
DEM	Discrete Element Method
DFT	Density Functional Theory
DNS	Direct Numerical Simulation
DPM	Discrete Particle Method
FEA	Finite Element Analysis
FEM	Finite Element Method
FEMB	Finite Element Model Builder
G	Gidaspow (drag law)
LES	Large Eddy Simulation
MC	Monte-Carlo (method)
MD	Molecular Dynamics
MRI	Magnetic Resonance Imaging

PC	Phase Coupled
PDE	Partial Differential Equation
PEM	Particle Element Model
PEPT	Positron Emission Particle Tracking
RSM	Reynolds-Stress Model
SN	Schiller-Naumann (drag law)
SO	Syamlal-O'Brien (drag law)
TB	Tight-Binding (approximations)
UDF	User-Defined Function
USB	Universal Serial Bus
VFB	Vibro-Fluidized Bed
WY	Wen and Yu (drag law)

1. INTRODUCTION

1.1 Motivation and Background

Forests cover 76 % of Finland's land area and wood is the country's most important natural resource. Waste wood and wood produced for combustion are used as a fuel for heat and electricity generation. The only fossil energy source in Finland is peat, which accounted for 7 % of total electricity supply in 2004. Combined, the share of wood, peat, waste and other biofuels was around 20 % of Finland's total electricity consumption in 2004, while coal accounted for 18 %. Therefore, the use of coal, peat, and biomass fuels is an important factor in Finland's energy supply, and intensive research and development is done to enhance the efficiency of their combustion and to reduce pollutant emissions. /9/, /21/, /22/

Gas-fluidized beds are used in industry for mixing, catalysis, combustion, and other applications. In particular, bubbling fluidized bed systems have been successfully applied to the combustion of coal, wood, peat and waste materials in industrial power plants because of their economical and environmental advantages. Fluidized bed boilers offer a suitable alternative for burning low-grade coal and improve the efficiency of energy utilization compared to conventional boiler furnaces. Moreover, high rates of heat and mass transfer between gas and particles can be achieved in fluidized bed and hence heat exchangers within the bed medium require relatively small surface areas. /1/, /9/

The efficiency of combustion is strongly affected by the gas and particle mixing inside the bed. Therefore, the design and control of combustion in fluidized bed reactors requires extensive knowledge about the dynamic behavior of the fluidization process. Fluidization can be defined as the process by which solid particles are transformed into fluid-like state through suspension in a gas or liquid. It occurs when the drag force exerted by the fluid on the particles exceeds gravity. The ease by which particles fluidize and the range of operating conditions that sustain fluidization vary greatly among gas-solid systems and several factors might affect this. Size and size distribution of solids, fluid-solid density ratio, and vessel geometry are among such factors that influence the fluidization quality. /1/, /2/, /9/

In general, fine granular particles tend to agglomerate and form clusters, especially if they are moist or sticky; thus, the bed must be agitated to maintain satisfactory fluidizing conditions. This can be done with a mechanical stirrer or by operating at relatively high gas velocities and using the kinetic energy of the entering gas jets to agitate the solids. However, high gas flow rates induce instability in the bed and some of the gas passes through the bed in the form of bubbles or slugs. Bubbles are created at the bottom of the bed and traverse the granular layer causing destruction to the uniform fluidization state, which is, practically, the most desirable state in many industrial applications. /2/, /3/

The need to achieve homogeneous structure for the gas-fluidized bed determines the use of various fluidization methods. Vertical vibration, which can be used as a strategy to improve the kinetics of fluidization and to avoid problems like channeling, defluidization and slug flow, is one of these methods.

Vibration may be produced by mechanical shaking of the entire apparatus or just the gas distributor grid. The Vibro-Fluidized Bed (VFB) of solid particles is a modification of the Conventional Fluidized Bed (CFB), wherein vibration energy is transferred to the bed of particles by a mechanical generator. Commercial application of VFBs has been increasing over the past decade for economic drying of wide range of particle sizes and difficult-to-fluidize sticky powders.

The application of VFB in several industries is growing due to the following advantages:

1. Compared to the conventional fluidized bed, the minimum fluidization velocity is much lower and pressure drop at the onset of fluidization is much smaller for VFB; thus the energy consumption and entrainment of fines are reduced significantly;
2. Residence time, intensity of mixing and heat and mass transfer properties are controllable in VFB by changing amplitude and/or frequency of vibration;
3. Good conditions for heat/mass transfer can be insured due to the possibility of independent control of gas velocity and vibration parameters;

4. Cohesive, sticky materials can be processed with higher efficiency in a VFB than in a CFB, in which these types of materials are seldom fluidizable.

The study of mechanisms of bed instabilities is an active research area in the physics and engineering community. But in spite of the numerous publications and even more industrial processes, VFB dynamic and transport properties are very complicated and far from being fully understood.

The complexity of solid movements and the fluid-dynamic behavior of vibrated granular materials under fluidized conditions depend mainly on the physical properties of the particles, acceleration of vibration, multiphase flow parameters, in addition to the container geometry (as mentioned above). A small difference in those parameters can cause a sever change in terms of the efficiency of fluidized bed reactors and it is not known in detail how granular dynamics depend on those parameters. Therefore, empirical correlations are still basic features of the practical design of fluidized beds, but since the mid-20th century there has been greater interest in a more fundamental approach such as the modeling of the fluid motion and particle phases. /2/, /4/, /7/, /10/, /11/

1.2 Static and Dynamic Behavior of Granular Materials

Granular media, of which sand is one example, are unique in that they can exhibit both solid- and fluid-like properties. Under weak shear they deform plastically and under high shear they flow. For instance

- Unlike solids, granular materials conform to the shape of the container in which they are placed;
- Unlike liquids, a pile of sand on a flat surface will remain stationary, while an equivalent volume of fluid would rapidly spread out to cover the surface;
- Conversely, if the surface holding the sand pile is sufficiently tilted the sand will show a superficial resemblance of liquid flow;
- A contained granular medium (like a bucket full of sand) can support the weight of an object placed on top of the medium even when that object is much denser than the medium. /5/, /6/, /7/, /8/

Highly agitated systems of particles are often modeled in a manner similar to a rarefied gas. An important difference, though, is that, unlike collisions between gas molecules, solid particle interactions in a granular flow dissipate energy because of static friction, inelasticity of collisions and drag between the fluid and particles. Therefore, ordinary thermodynamic temperature is too small to allow relative particle motion and a granular material "gas" can quickly reach to a zero effective temperature. As an example, a typical small stainless steel sphere of mass m = 10 [mg], moving at a speed of 10 [cm/s] in a fluidized granular medium has a kinetic energy of the order 10^{17} times greater than the thermodynamic energy scale k_BT at room temperature, where k_B is Boltzmann constant. The kinetic energy associated with granular motion (called granular temperature) is not constant. Instead, it is continually and irrecoverably transferred by collisions to internal (thermal or non-kinetic) degrees of freedom. Nevertheless, there have been significant efforts to use the kinetic theory of gases and statistical mechanics to investigate the dynamics of nonequilibrium steady-state granular systems. /13/, /17/, /18/, /19/, /36/

Experiments and simulations reveal that the behavior of a granular bed can be classified into two characteristic categories known as shallow and deep beds. For example, when a shallow bed consisting of less than six layers of glass spheres is subjected to oscillations with acceleration amplitudes greater than approximately 2.0 g, where g is the acceleration due to gravity, the particles in the container are fluidized and do not display coordinated movement. Further, when more than six particle layers are used, the particle bed moves as coherent inelastic mass and the deep bed exhibit complex and unusual phenomena like, convection, bubbling, surface waves, segregation, heap formation, and so on. /13/, /14/

1.3 Review of Previous Related Work

At the present, there is no well-established unifying model or equation of motion, analogous to the Navier-Stokes equation for fluids that describes all those nonequilibrium dynamical states involved during the phase change between solid and fluid-like behavior and vice-versa. Additionally, little is known about an apparently simple quantity: the drag force (F_D) resisting a solid object moving slowly through a granular medium. As for a viscous fluid, F_D is a fundamental property of a granular

material and is important to any industrial process involving objects moving through granular matter. /20/

Previous direct studies of the granular drag force have been quite limited, although long experience in soil physics suggests that, due to its frictional origin, the velocity dependence will be much weaker than that in fluids. Albert *et al* demonstrated experimentally that the drag force resisting a vertical cylinder traveling in a granular material at low velocity is determined by the static properties of the granular medium, despite the fact that drag force is a dynamic quantity. They found that it is linearly dependent on the cylinder diameter, quadratically dependent on the depth of insertion, and independent of velocity. Studies by Wieghhardt found that F_D depended non-monotonically on the object's velocity (first decreasing and then increasing with increasing velocity) and was proportional to the $\frac{5}{2}$ power of the depth of insertion and the square root of its horizontal dimension. Tardos *et al* observed the same non-monotonic velocity dependence as Wieghhardt, confirming the equivalence of the measurement regimes. Experiments performed by Zik *et al*, reported measurements of the mobility/friction coefficients of a sphere dragged horizontally through a vertically vibrated granular system. They observed a linear dependence of the drag force on the sphere velocity. /15/, /16/, /20/, /26/

Work by Pak *et al* regarding heap formation indicates that the interstitial fluid is very important for the formation of heaps and the associated convection pattern in vibration fluidized beds, although they recognize that other mechanisms such as wall friction or inhomogeneous forcing can still produce the observed heap and convection patterns. They also observed that the interstitial gas effects (effect of lift and drag force) were most important for deep beds and for small particles (glass spheres, $d < 1$ [mm]) which would accord with the studies of interstitial fluid effects by Zeininger and Brennen. Laroche *et al* also found that these effects were important for the formation of heaps for particle beds comprised of glass spheres with diameters between 0.63 and 0.8 [mm], but they do not mention how beds with larger particles are affected. Evesque however reports that in experiments using 0.2, 0.4 and 1 [mm] diameter glass spheres the interstitial fluid effects were negligible. These experiments did not show any

appreciable difference in heap shape or convection pattern for evacuated containers or for containers with mesh walls that allow air to be drawn in from the sides instead of throughout the particle bed. Discrete element simulations performed by Wassgren *et al*, in which the interstitial fluid effects were not included, have reproduced all of the mentioned bed phenomena except for the heaping behavior. /50/

1.4 Objectives and Thesis Structure

The original aim of this thesis was to explore the effect of drag force on a sphere that is immersed in a granular bed which is subjected to vertical oscillations, and ultimately to develop a simple drag model for the drag force in such environment. Due to time limitations and complexity of the subject, with the current research oriented toward specific areas, this Master's thesis is favored to serve as a guide for a future research in this field. Hence, we attempt here to fill a gap in current literature by presenting a problem of practical importance and provide the reader with good theoretical information and experimental results, combined with the necessary simulations that form a rigid foundation to build on.

With the above objectives kept in mind, the remainder of this thesis has the following organization:

Chapter two describes a number of topics related to the dynamics of single particle motion. These include a discussion about the drag force from the continuum and statistical points of view, Hertz theory, and inelastic contact between particles. Experimental measurements of the coefficient of restitution, along with finite element simulations representing different material models and applied to a sample test data from experiment, are also issues that are addressed in this chapter.

In Chapter three we shift to a more global picture, showing the case in which a contained system particles is set in motion by forced vertical vibration. Early in that chapter we introduce the subject of vertical vibration of granular materials and its industrial applications, besides the experimental techniques which are used to probe into granular flows. Next, we present an experiment designed to study the factors that influence the behavior of vertically-shaken granular media and then interpret the results of this experiment. Continuum and discrete models of granular flow are

discussed in detail with concentration on the Eulerian multiphase model, which is subsequently used in the Computational Fluid Dynamics (CFD) simulations that follow.

Alternatively, Chapter four focuses on the modal analysis simulations done with ANSYS Workbench™ software. The mode shapes of a granular bed, modeled as a coherent rigid mass that symbolizes the experiment in Chapter three, are investigated when the friction coefficient between the container walls and the bed material is varied. By comparison between the resonance frequency of the bed extracted from simulations and experimental results, we could predict an approximate value for the friction factor.

The last chapter summarizes the main points and conclusions obtained in this thesis. It denotes some useful facts and recommendations that may need to be taken into account for conducting further future research in the same field.

2. SINGLE-PARTICLE DYNAMICS

2.1 Drag Force: A Continuum Approach

2.1.1 Drag of Immersed Bodies

The individual motion of an object in different fluids is predominantly influenced by drag and gravity. While the latter, gravity, is known exactly, the former is harder to characterize. By physical definition, drag is the component of force acting parallel to the direction of motion. It is essentially a flow loss and must be overcome if the body is to move against the fluid stream.

In low-speed flow past geometrically similar bodies with identical orientation and relative roughness, the drag coefficient should be a function of the body Reynolds number:

$$C_D = f(\mathrm{Re}) \tag{1}$$

The Reynolds number is defined as:

$$\mathrm{Re} = \frac{\upsilon L}{\nu} \tag{2}$$

where υ is the free-stream velocity, L is the characteristic length of the body, and ν is the kinematic viscosity of the fluid. The drag coefficient can be defined by using a characteristic area A, which may differ depending upon the body shape:

$$C_D = \frac{F_D}{\frac{1}{2}\rho\upsilon^2 A} \tag{3}$$

where ρ is the fluid density. It must be remembered that the effects of compressibility or free-surface effects are not considered in the discussion about drag force.
/23/, /24/, /25/

2.2.2 Fluid Flow Over A Sphere: Friction and Pressure Drag

Boundary-layer theory gives us a great qualitative grasp of viscous-flow behavior, but, because of flow separation, the theory does not generally allow a quantitative computation of the complete flow field. It can predict, for example, the separation point but cannot accurately estimate the (usually low) pressure distribution in the separated region. The difference between the high pressure in the front stagnation region and the low pressure in the rear separated region causes a large drag contribution called pressure drag. This is added to the integrated shear stress or friction drag of the body, which gives the total drag coefficient:

$$C_D = C_{D,\text{press}} + C_{D,\text{fric}} \tag{4}$$

The relative contribution of friction and pressure drag depends on the body's shape, especially its thickness

The drag coefficient for flow over a smooth sphere is shown in Figure 1 as a function of Reynolds number. At very low Reynolds number, $Re \leq 1$, there is no flow separation from the sphere; the wake is laminar and the drag is essentially a friction drag. Stokes (1851) has shown analytically, for very low Reynolds number flows that drag force acting on a sphere of diameter d, moving at speed υ, through a fluid of viscosity μ, is given by:

$$F_D = 3\pi\mu\upsilon\, d \tag{5}$$

The drag coefficient, defined by Equation (3), is then:

$$C_D = \frac{24}{\text{Re}} \tag{6}$$

As shown in Figure 1, this expression agrees with experimental values only at low Reynolds number.

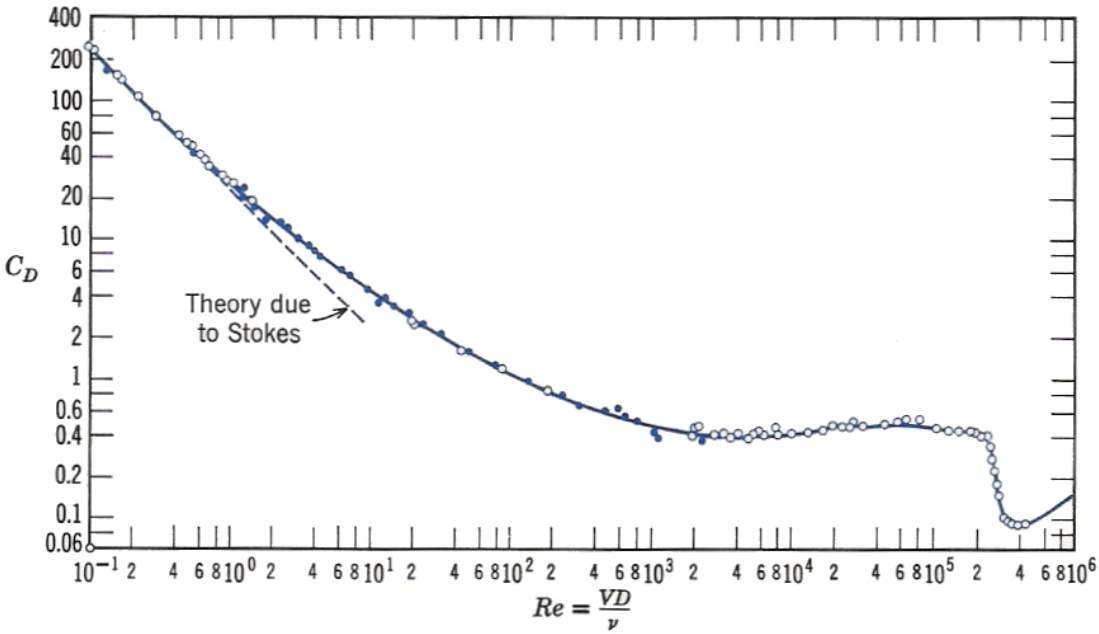

Figure 1 *Drag coefficient of a smooth sphere as a function of Reynolds number.* /25/

As the Reynolds number is increased up to about 10^3, the drag coefficient drops continuously and it is value is a combination of friction and pressure drag. In the range $10^3 < Re < 3\times10^5$ the drag coefficient curve is relatively flat, but it undergoes a rather sharp drop at the critical Reynolds number of about 3×10^5. For Reynolds numbers larger than 3×10^5, transition occurs and the boundary layer on the forward portion of the sphere becomes turbulent.

Figure 2 illustrates the sharp differences between laminar separation and turbulent separation for a sphere. The laminar flow is characterized by a broad wake, drag coefficient $C_D = 0.5$, and very low pressure in the separated region behind the sphere. The turbulent flow has smaller wake, $C_D = 0.2$, and higher pressure on the rear. The drag coefficient in the turbulent boundary layer flow is 2.5 times less than that for laminar flow. /23/, /25/

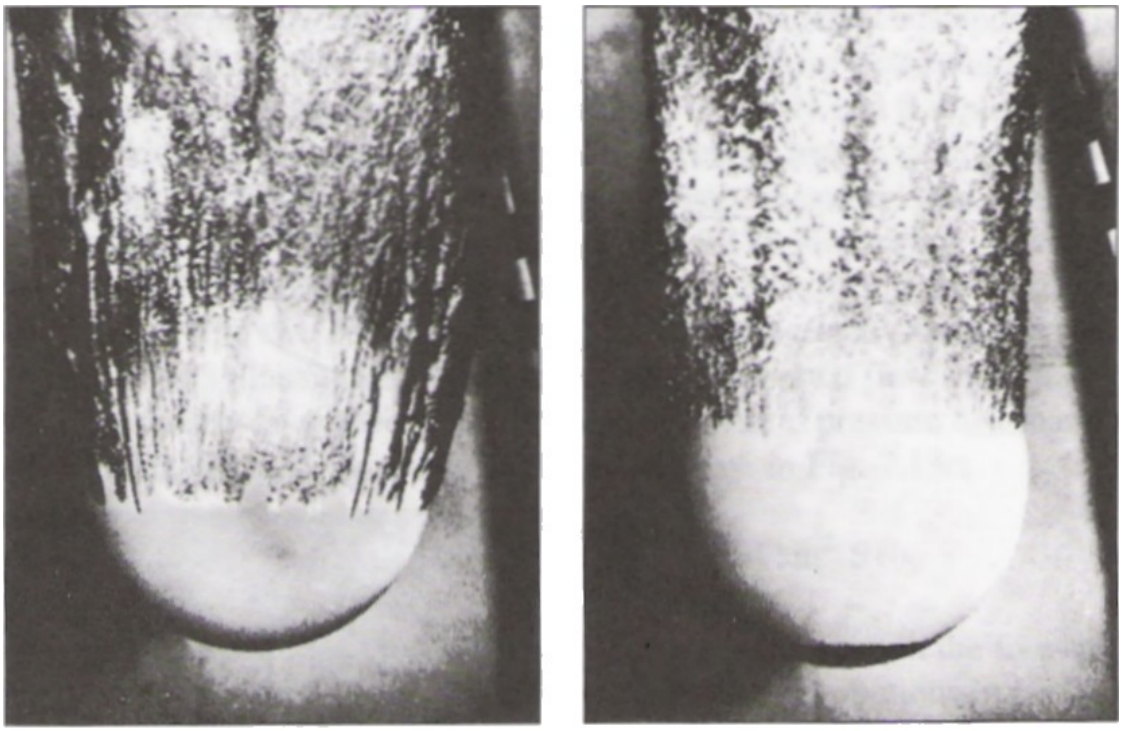

(*a*) (*b*)

Figure 2 *Strong differences in laminar and turbulent separation on 0.216 [m] bowling ball entering water at 7.62 [m/s]:* (*a*) *smooth ball, laminar boundary layer;* (*b*) *same entry, turbulent flow induced by patch of sand roughness at the nose of the ball.* /23/

If the sphere is spinning as it moves through the fluid, the drag force will have a different assessment than a non-rotating translational sphere. The Magnus effect has the influence of generating a peculiar lifting force, also called Magnus force, that rotating objects experience when they move through a medium. A spinning object creates a sort of whirlpool of rotating fluid about itself, see Figure 3. On the side where the motion of the whirlpool is in the same direction as that of the stream to which the object is exposed the velocity will be enhanced. On the other side, where the motion is opposed, the velocity will be decreased. According to Bernoulli's principle, the pressure is lower on the side where the velocity is greater, and consequently there is an unbalanced force at right angles to the streamlines. This is the Magnus force. /27/

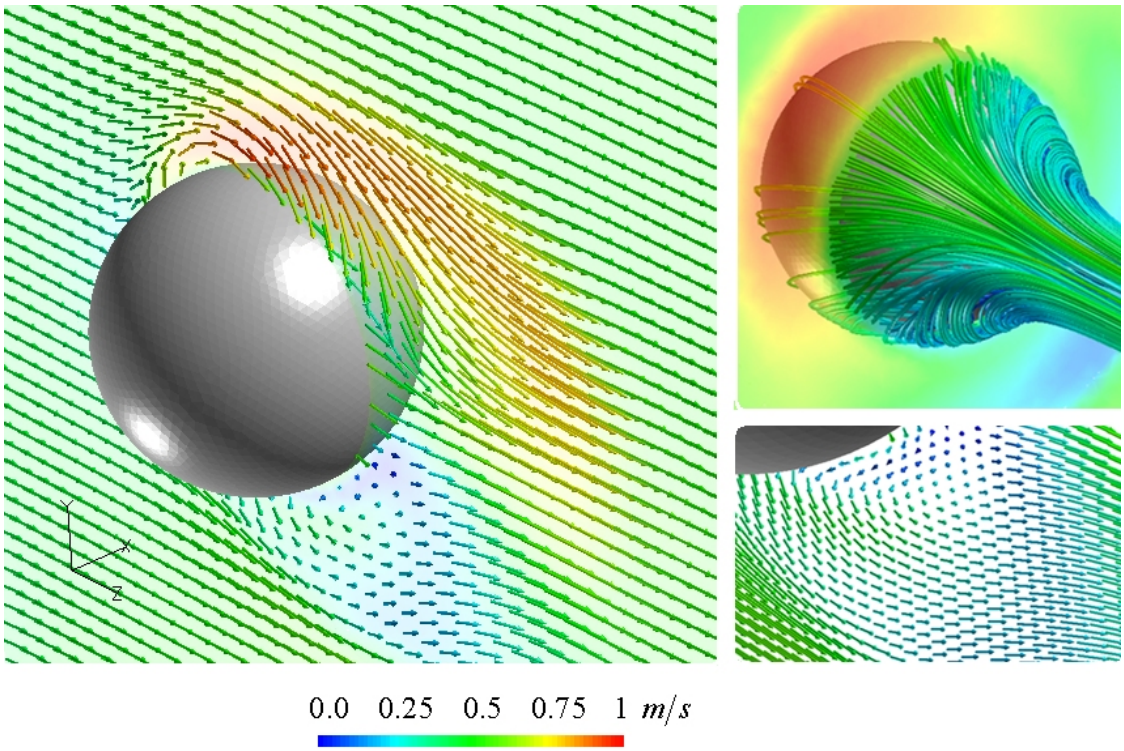

Figure 3 *Velocity vectors of a rotating sphere. The stream lines are shown in the upper right corner picture and circulation rolls behind the sphere are magnified in the lower right corner.*

It can be concluded from the preceding paragraphs that the drag force exerted on a sphere is directly proportional to the viscosity of the fluid, and velocity and size of the sphere, for low speeds of the sphere. But what is the drag force that is resisting a ball in a vibro-fluidized granular material bed? Specifically, what is the "granular viscosity" that is depicted from viscous drag in fluids, and can the continuum macroscopic concept adopted for classical fluid mechanics predict for us an equation similar to Stokes law of Drag?

2.2 Drag Force: A Statistical Mechanics Approach

The questions rose at the end of the previous section clearly indicate that there are fundamental differences between granular materials and fluids. The continuum assumption of fluids disregards the behavior of individual molecules at the microscopic scale. This has a dramatic impact that penetrates to the core of the dynamics of granular materials.

The most important difference between a ‘‘gas’’ of granular particles and a regular gas (or liquid) is the inelastic nature of the interparticle collisions. The steady removal of kinetic energy from the granular gas due to dissipative collisions causes a variety of nonequilibrium processes that have been subjects of experimental and theoretical interest. Particularly, in recent time many of the experimental results have been reproduced and investigated using various techniques such as cellular automata, Monte Carlo methods, lattice-gas models, and molecular dynamics in two and three dimensions, and hybrid methods. /28/

Unlike the elastic collision between liquid or gas molecules, collision between particles in the fluidized state is inelastic and plays a significant role in determining the granular materials behavior. The statistical point of view can assist at this stage in understanding.

Fluid-like behavior in granular materials can only be achieved by continuously driving the system with some external source of energy. Some examples of energy sources used in experiments with granular systems are gravity, shear, air flows, electric and magnetic fields, and mechanical vibrations. Mechanical vibrations are probably the most widely used method to fluidize dilute systems of grains. In vibro-fluidized systems particles confined in a container get energy from collisions with an oscillating boundary. The energy is further transported through inter-particle collisions to the bulk of the system.

The chaotic motion of the grains in a vibro-fluidized steady-state regime very much resembles that of molecules in a gas, thus the name “granular gas” or “inelastic gas” is given to such granular systems. The granular gas is by no means in a state of thermodynamical equilibrium. Nevertheless, there have been significant efforts to use kinetic theory and statistical mechanics to investigate the dynamics of steady-state granular systems. /19/

2.3 Viscosity

A fluid may be defined as a substance that deforms continuously under the action of a shear stress. From a classical dynamics viewpoint, to derive the motion of a collection of particles it is required to know the forces acting on them. One may then use Newton's equations of motion to solve for the particle positions and momentum. From a statistical mechanics viewpoint, the knowledge of the state of an ensemble of particles is related to the energy of the particles, which allows the derivations of probabilities relative to that state.

Shear viscosity is one of the Navier-Stokes transport coefficients, which relate thermodynamic fluxes to their conjugate thermodynamic forces. Fluid mechanics is able to determine the macroscopic behaviour of non-equilibrium systems, but its laws need to be supplemented with the specification of adequate boundary conditions and with thermo-physical constants like the above mentioned transport coefficients. These quantities are usually obtained through experiments. One of the aims of statistical mechanics, devoted to non-equilibrium systems, is to derive these quantities from a microscopic description of the system. /65/

The behaviour of an infinitesimal fluid element between two infinite plates is shown in Figure 4. The upper plate moves at constant velocity, δu, under the influence of a constant applied force, δF_x. It can be proven that the fluid element, when subjected to shear stress, τ_{yx}, will experience a rate of deformation (shear rate) given by du/dy. Fluids in which shear stress is directly proportional to rate of deformation are called Newtonian fluids. The term non-Newtonian is used to classify all fluids in which shear stress is not proportional to shear rate. Then, for a Newtonian fluid:

$$\tau_{yx} \propto \frac{du}{dy} \tag{7}$$

The constant of proportionality is the dynamic (or shear) viscosity, μ. For one-dimensional flow, Newton's law of viscosity, in terms of the coordinates in Figure 4, is given by:

$$\tau_{yx} = \mu \frac{du}{dy} \tag{8}$$

Viscosity is, therefore, a measure of the resistance of a fluid to deformation under shear stress. It describes a fluid's internal resistance to flow and may be thought of as a measure of fluid friction. The mechanism of gas viscosity is reasonably well understood, but the theory is poorly developed for liquids. In the following subsections the viscosity of gases, liquids and solids is briefly discussed (for comparison purposes). /25/, /66/

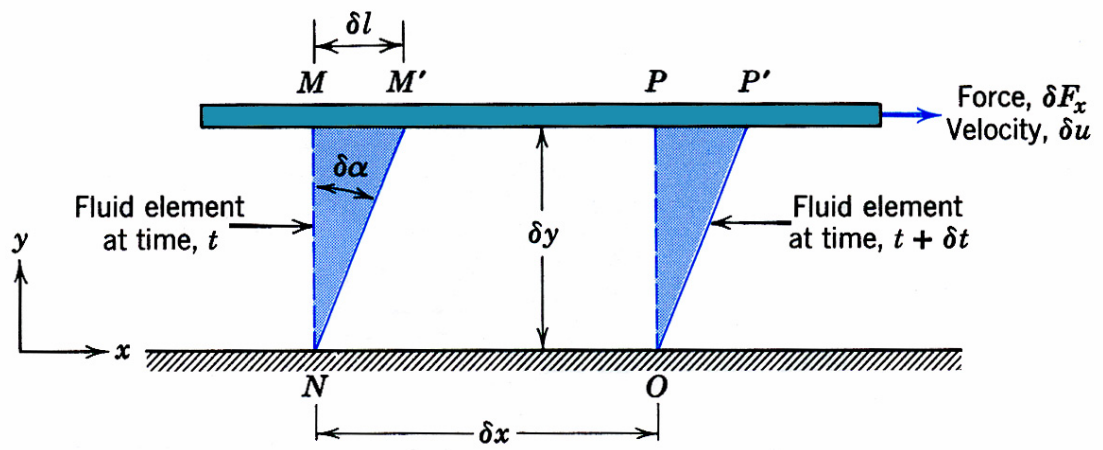

Figure 4 *Deformation of a fluid element.* /25/

2.3.1 Viscosity of Gases

Viscosity in gases arises principally from the molecular diffusion that transports momentum between layers of flow. The kinetic theory of gases allows accurate prediction of the behaviour of gaseous viscosity, in particular that, within the regime where the theory is applicable:

- Viscosity is independent of pressure (except at very high pressures, the viscosity increases with pressure or density); and
- Viscosity increases as temperature increases (analysis based on kinetic theory predict $\mu \propto \sqrt{T}$). /25/, /66/

2.3.2 Viscosity of Liquids

In liquids, the additional forces between molecules become important. This leads to an additional contribution to the shear stress, though the exact mechanics of this are still controversial. Thus, in liquids:

- Viscosity is independent of pressure (except at very high pressure); and
- Viscosity tends to fall as temperature increases.

The dynamic viscosities of liquids are typically several orders of magnitude higher than that of gases. /66/

2.3.3 Viscosity of Solids

It is commonly asserted that amorphous solids, such as glass, have viscosity, arguing on the basis that all solids flow, to some possibly minute extent, in response to shear stress. Advocates of such a view hold that the distinction between solids and liquids is unclear and that solids are simply liquids with a very high viscosity. However, others argue that solids are, in general, elastic for small stresses while fluids are not. Even if solids flow at higher stresses, they are characterized by their low-stress behavior. Viscosity may be an appropriate characteristic for solids in a plastic regime. The situation becomes somewhat confused as the term viscosity is sometimes used for solid materials, for example Maxwell materials, to describe the relationship between stress and the rate of change of strain, rather than rate of shear.

These distinctions may be largely resolved by considering the constitutive equations of the material in question, which take into account both its viscous and elastic behaviors. Materials for which both their viscosity and their elasticity are important in a particular range of deformation and deformation rate are called viscoelastic. The solids shear viscosity, within the context of granular materials, is discussed in more detail in Chapter 3. /66/

2.4 Elastic Binary Collisions and Hertz Contact Theory

There are two types of contacts that we have to distinguish when the surfaces of two solid bodies are brought into touch: conforming and non-conforming contacts. A

contact is said to be conforming if the surfaces of the two bodies "fit" exactly or even closely together without deformation. Journal bearings and flat slider bearings are examples of conforming contacts. Bodies which have dissimilar profiles are said to be non-conforming. When two non-conforming solids are brought into contact they touch initially at a single point or along a line. Under the action of the slightest load they deform in the vicinity of their point of first contact so that they touch over an area which is finite, though small compared with the dimensions of the two bodies.

A mathematical contact model is required to predict the shape of this contact area and how it grows in size with increasing load; the distribution; and magnitude of surface tractions, normal and possibly tangential, transmitted across the interface. Finally it should enable the components of deformation and stress in both bodies to be calculated in the vicinity of the contact region. The classical theory of collision between two frictionless elastic bodies is due to Hertz and follows directly from his statical theory of elastic contact. /64/

2.4.1 Geometry of Solid Surfaces in Contact

A description of the geometry of the contacting surfaces is necessary before the problem in elasticity can be formulated. It is agreed in literature to take the point of first contact as the origin of a rectangular coordinate system in which the *x*-*y* plane is the common tangent plane to the two surfaces and the *z*-axis lies along the common normal directed positively into the lower solid, Figure 5a.

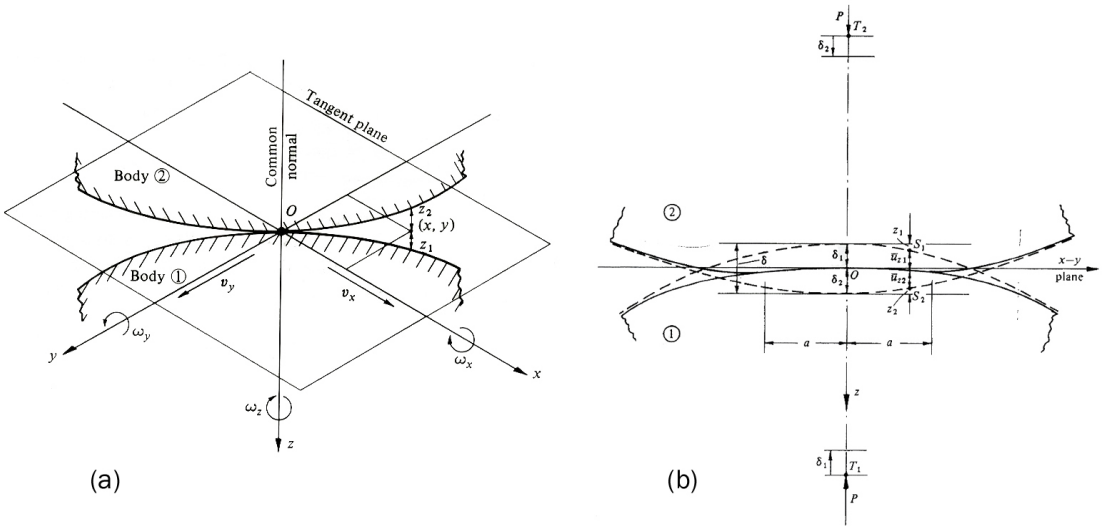

Figure 5 *Geometry of two bodies in Contact*: (a) *3D*; (b) *2D*. /64/

Thus we may express the profile of each contacting surface in the region close to the origin approximately by an expression of the form:

$$z_1 = A_1 x^2 + B_1 y^2 + C_1 xy + \ . \ . \ . \tag{9}$$

where higher order terms in x and y are neglected. By choosing the orientation of the x and y axes, x_1 and y_1, so that the term in xy vanishes, Equation (9) may be written:

$$z_1 = \frac{1}{2R_1'} x_1^2 + \frac{1}{2R_1''} y_1^2 \tag{10}$$

where R_1' and R_1'' are the principal radii of curvature of the surface at the origin. A similar expression may be written for the second surface:

$$z_2 = -\left(\frac{1}{2R_2'} x_2^2 + \frac{1}{2R_2''} y_2^2 \right) \tag{11}$$

The separation between the two surfaces is given by $h = z_1 - z_2$, hence:

$$h = Ax^2 + By^2 = \frac{1}{2R'} x^2 + \frac{1}{2R''} y^2 \tag{12}$$

where A and B are positive constants and R' and R'' are defined as the principal relative radii of curvature. In this description of the initial separation between the two surfaces, a convex surface is assumed to have a positive radius and a negative sign to concave curvatures.

When a normal compressive load is applied to the two solids the point of contact spreads into an area. If the two bodies are solids of revolution (e.g. spheres), then $R_1' = R_1'' = R_1$ and $R_2' = R_2'' = R_2$, whereupon $A = B = \frac{1}{2}\left(1/R_1 + 1/R_2\right)$. In Figure 5b a normal load P is applied to two solids of general shape (but chosen convex for convenience) and shown in cross section after deformation. The separation between

two corresponding surface points $S_1(x, y, z_1)$ and $S_2(x, y, z_2)$ before deformation is given by Equation (12). From the symmetry of this expression about O the contact region must extend an equal distance on either side of O. During the compression distant points in the two bodies T_1 and T_2 move towards O, parallel to the z-axis, by displacements δ_1 and δ_2 respectively. If the solids did not deform their profiles would overlap as shown by the dotted lines in Figure 5b. Due to the contact pressure the surface of each body is displaced parallel to Oz by an amount $\bar{u}_{z1}$ and $\bar{u}_{z2}$ (measured positive in each body) relative to the distant points T_1 and T_2. If, after deformation, the points S_1 and S_2 are coincident within the contact surface then:

$$\bar{u}_{z1} + \bar{u}_{z2} + h = \delta_1 + \delta_2 \tag{13}$$

Writing $\delta = \delta_1 + \delta_2$ and making use of Equation (12) we obtain an expression for the elastic displacements:

$$\bar{u}_{z1} + \bar{u}_{z2} = \delta - Ax^2 + By^2 \tag{14}$$

where x and y are the common coordinates of S_1 and S_2 projected onto the x-y plane. If S_1 and S_2 lie outside the contact area so that they do not touch, it follows that:

$$\bar{u}_{z1} + \bar{u}_{z2} > \delta - Ax^2 - By^2 \tag{15}$$

To examine how the deformations and stresses grow as the load is applied on the basis of elementary dimensional reasoning, we note that in Figure5b, $\delta_1 = \bar{u}_{z1}(0)$ and $\delta_2 = \bar{u}_{z2}(0)$, so Equation (13) can be written in the dimensionless form as:

$$\left\{\frac{\bar{u}_{z1}(0)}{a} - \frac{\bar{u}_{z1}(x)}{a}\right\} + \left\{\frac{\bar{u}_{z2}(0)}{a} - \frac{\bar{u}_{z2}(x)}{a}\right\} = \frac{1}{2}\left(\frac{1}{R_1} + \frac{1}{R_2}\right)\frac{x^2}{a} \tag{16}$$

Substituting $x = a$ and writing $\bar{u}_z(0) - \bar{u}_z(a) = d$, the deformation within the contact zone, Equation (16) becomes:

$$\frac{d_1}{a} + \frac{d_2}{a} = \frac{a}{2}\left(\frac{1}{R_1} + \frac{1}{R_2}\right) \tag{17}$$

Provided that the deformation is small, i.e. $d \ll a$, the state of the strain in each solid is characterized by the ratio d/a. The magnitude of the strain will be proportional to the contact pressure divided by the elastic modulus E; therefore, if p_m is the average contact pressure acting mutually on each solid, Equation (17) becomes:

$$\frac{p_m}{E_1} + \frac{p_m}{E_2} \propto a\left(\frac{1}{R_1} + \frac{1}{R_2}\right) \Rightarrow p_m \propto \frac{a\left(1/R_1 + 1/R_2\right)}{1/E_1 + 1/E_2} \tag{18}$$

Thus, for a given geometry and materials, the contact pressure and the associated stresses increase in direct proportion to the linear dimension of the contact area. In the contact of spheres the compressive load is $P = \pi a^2 p_m$. Hence from Equation (18):

$$a \propto \left\{\frac{P\left(1/E_1 + 1/E_2\right)}{\left(1/R_1 + 1/R_2\right)}\right\}^{1/3} \tag{19}$$

$$p_m \propto \left\{\frac{P\left(1/R_1 + 1/R_2\right)^2}{\left(1/E_1 + 1/E_2\right)^2}\right\}^{1/3} \tag{20}$$

For three-dimensional contact the compressions of each solid δ_1 and δ_2 are proportional to the local indentations d_1 and d_2, hence the approach of distant points is:

$$\delta = \delta_1 + \delta_2 \propto d_1 + d_2 \propto \left\{P^2\left(1/E_1 + 1/E_2\right)^2\left(1/R_1 + 1/R_2\right)\right\}^{1/3} \tag{21}$$

The approach of two bodies due to elastic compression in the contact region is therefore proportional to $(\text{load})^{2/3}$. /64/

2.4.2 Hertz Theory of Elastic Contact

So far it was shown that the contact area, stress and deformation might be expected to grow with increasing load and we have also found the influence of curvature and elastic moduli by simple dimensional reasoning. To obtain absolute values for these quantities we must turn to the theory of elasticity.

The first satisfactory analysis of the stresses at the contact of two elastic solids is attributed to Hertz (1882). Hertz formulated the conditions expressed by Equations (14) and (15) which must be satisfied by the normal displacements on the surface of the solids. Denoting the significant dimension of the contact area by *a*, the relative radius of curvature by *R*, the significant radii of each body by R_1 and R_2 and the significant dimensions of the bodies both laterally and in depth by *l*, we may summarize the assumptions made in the Hertz theory as follows:

- The surfaces are continuous and non-conforming: $a \ll R$;
- The strains are small: $a \ll R$;
- Each solid can be considered as an elastic half-space: $a \ll R_{1,2}$, $a \ll l$;
- The surfaces are frictionless: $q_x = q_y = 0$.

For solids of revolution having a circular contact area, Hertz found that the radius of this contact circle can be expressed as:

$$a = \left(\frac{3PR}{4E^*} \right)^{1/3} \tag{22}$$

where:

$$\frac{1}{E^*} = \frac{1-\nu_1^2}{E_1} + \frac{1-\nu_2^2}{E_2} \tag{23}$$

where v is Poisson's ratio.

The mutual approach of distant points in the two solids is given by:

$$\delta = \frac{a^2}{R} = \left(\frac{9P^2}{16RE^{*2}} \right)^{1/3} \tag{24}$$

The maximum pressure p_0 is 3/2 times the mean pressure p_m

$$p_0 = \frac{3P}{2\pi a^2} = \left(\frac{6PE^{*2}}{\pi^3 R^2} \right)^{1/3} \tag{25}$$

The expressions in (22), (24) and (25) have the same form as (19), (20) and 21), however these equations also provide absolute values for the contact size, compression and maximum pressure. /64/

2.5 Inelastic Binary Collisions

2.5.1 The Coefficient of Restitution

The collision between objects can, normally, be classified as elastic or inelastic. The degree of elasticity for collision between particles is quantified by the coefficient of restitution (e), which is defined as the ratio of the difference in relative velocities of particles after and before collision, see Figure 6:

$$e = \left| \frac{\upsilon'_{12}}{\upsilon_{12}} \right| \tag{26}$$

$$\begin{aligned} \upsilon_{12} &= \upsilon_1 - \upsilon_2 \qquad (\textit{Before Collision}) \\ \upsilon'_{12} &= \upsilon'_1 - \upsilon'_2 \qquad (\textit{After Collision}) \end{aligned} \tag{27}$$

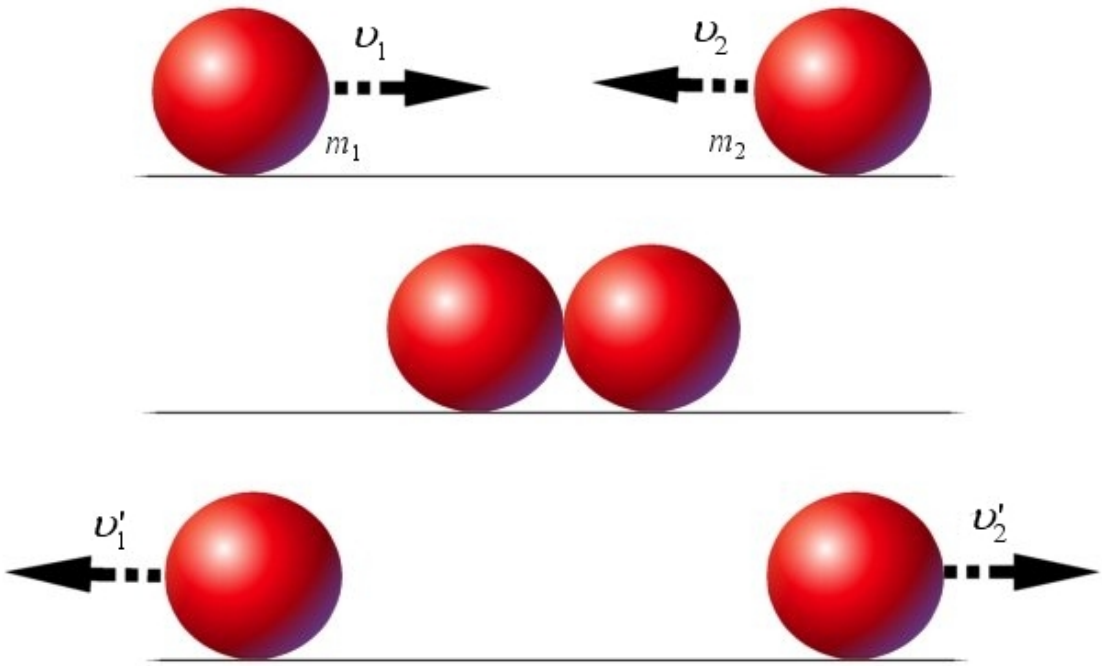

Figure 6 *Collision between two identical spheres in one dimension showing velocities of particles before and after the collision.*

The coefficient of restitution also characterizes the change (loss or gain) in kinetic energy during particle interactions. The table below describes what different values of *e* designate for one-dimensional collision.

Table 1 *A denotation of the restitution coefficient values for one-dimensional collision.*

Restitution Coefficient	**Collision Type**	**Kinetic Energy**
$e = 1$	Perfectly Elastic	Conserved
$0 < e < 1$	Partially Elastic	Not Conserved
$e = 0$	Perfectly Inelastic (plastic)	Maximum Possible Loss
$e > 1$	Hyperelastic	Energy Gained

Granular materials can be treated as a collection of inelastic hard spheres. Before developing any model for granular collisions, one needs first to have some information about the restitution coefficient that governs the relationship of contact forces between

impacting bodies. Since such data is scarcely available in literature, it is therefore necessary to conduct experiments to acquire this data.

Experiments by using the traditional Newton's cradle apparatus, illustrated in Figure 7, facilitated the measurement of the restitution coefficient for collision between spherical particles that have different material properties. From the principle of conservation of momentum and geometrical configuration of the Newton's device, it is possible to derive an expression for the coefficient of restitution.

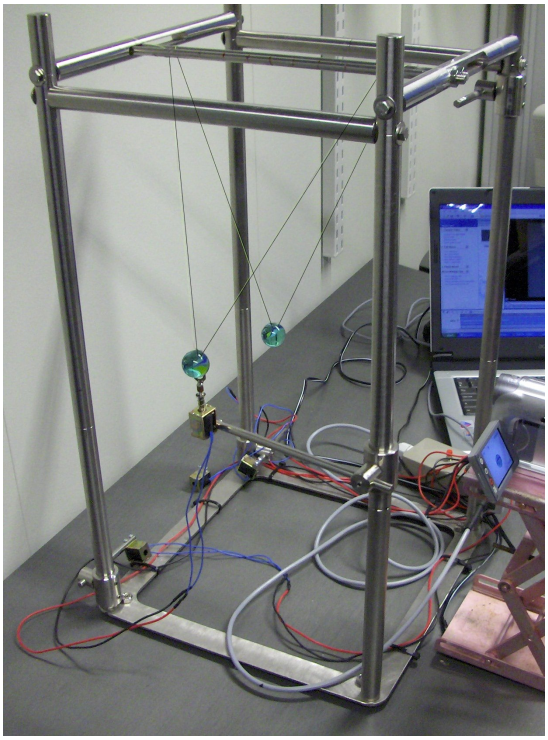

Figure 7 *Experimental setup for measuring the coefficient of restitution showing the Newton's cradle device.*

2.5.2 Experiment Setup for Binary Collision

The Newton's cradle device is made up of two swinging glass ball pendulums suspended from a sturdy frame by a V-shaped elastic wires, as shown in Figure 7. One of the balls is pulled back and maintained on a fork that is linked to a relay, while the second ball is hanging downwards under its own weight and is initially at rest ($\upsilon_2 = 0$). When the relay is released, the first ball is allowed to swing and collide with the stationary ball, thus increasing its velocity and elevation, see Figure 8. The maximum

velocity υ_2' and height h_2 that the second ball can reach are less than the initial impact velocity υ_{imp} and height h_1 of the first ball. This implies that there is a loss in mechanical energy due to collision.

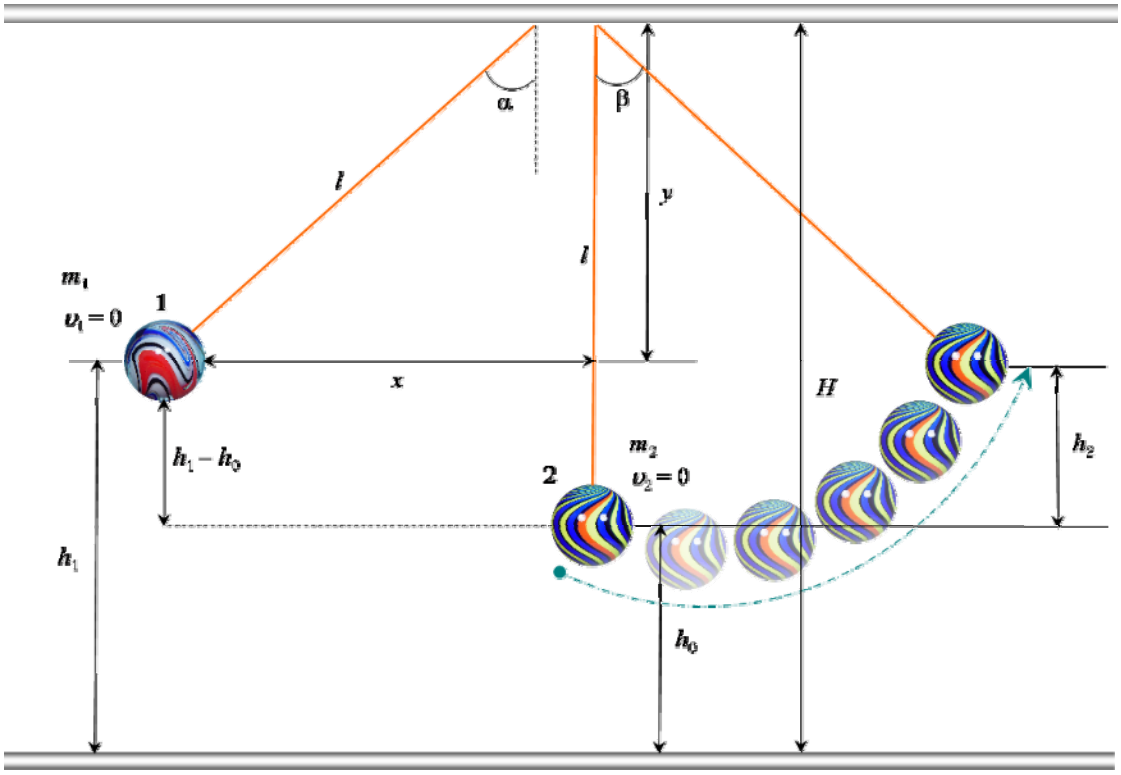

Figure 8 *A schematic layout of Newton's cradle device.*

The centers of the balls are carefully aligned before the experiment is started, in order to achieve a direct head-on collision at the point of contact. The left side ball is placed on the support fork of the relay, such that it is on the verge to fall under the effect of gravity when the relay's power is switched on. Care is taken to minimize rotation of the balls. This is done by:

- Using the V-shaped wires instead of a single wire;
- Checking that the ball and the fork are not skewed left or right;
- Keeping a balanced tension in the wires.

With a meter stick placed behind the glass balls, their initial position and height were precisely measured by snap-shooting with a digital video camera. The motion of the

spheres is recorded by a standard digital camcorder (Sony Handycam DCR-HC17E) at 30 frames per second and the exposure rate is approximately 1/33 millisecond. This sampling rate is believed to be accurate enough for capturing the motion of the balls. A frame by frame playback of the resulting animation (by using Microsoft® Windows Movie Maker) shows the position of the center of mass of each ball at different moments. In this respect, it is worth emphasizing the importance of adjusting the axis of the camera lens so it coincides with the center of the ball in every measurement that was done.

The objective is to develop an expression for the coefficient of restitution in terms of geometrical information collected from the recorded digital images, and simple trigonometry as sketched in Figure 8 above. The left ball makes an angle α with the vertical before it is released. After collision the right ball retards until it reaches a maximum height with an angle β from its equilibrium position. If the resistance of air and the ball's surface roughness are assumed to have minimum effect on the loss of energy, and hence neglected, the principle of conservation of momentum in one dimension can be used to verify that the coefficient of restitution for particles with identical masses is given by the following equation:

$$e = 2\frac{\sin(\beta/2)}{\sin(\alpha/2)} - 1 \tag{28}$$

For an ideal elastic impact of two balls, the angles α and β are equal and the value of e is one. Similarly, for spheres with different masses, the coefficient of restitution can be expressed as:

$$e = (1+k)\frac{\sin(\beta/2)}{\sin(\alpha/2)} - 1 \tag{29}$$

where k is the ratio of the masses of the two particles $k = m_2/m_1$, $m_1 > m_2$. The impact velocity of the left side ball in Figure 8 is defined as:

$$\upsilon_{\text{imp}} = 2\sqrt{gl}\sin\left(\alpha/2\right) \tag{30}$$

where l is the distance between the center of mass of the ball and its suspension point from the frame, and $g = 9.81$ [m/s^2] is the acceleration of gravity.

2.5.3 Experiment With The Ultrasonic Motion Detector

Elaborated efforts were made to ensure that the camera lens axis and the ball's center are not asymmetric. Measurements were repeated when it is found that the centers are not aligned. This necessitated that we seek for a different technique to measure the velocity before and after collision. The ultrasonic motion detector shown in Figure 9 was tried as an alternative method for that purpose.

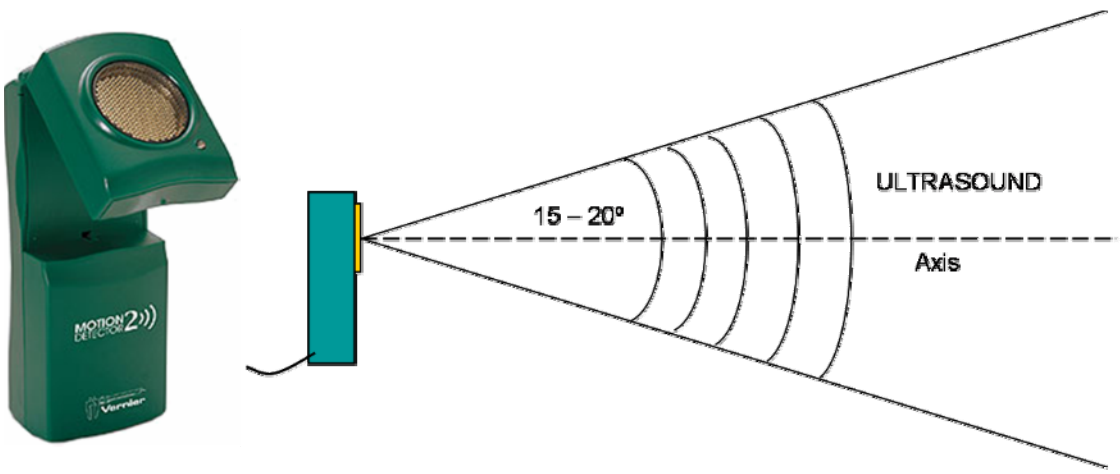

Figure 9 *The ultrasonic motion detector.*

The motion detector (manufactured by Vernier Software & Technology under the code MD-BTD) is designed to collect continuously position, velocity, and acceleration data of moving objects, without disturbing their motion. It emits bursts of 40 [kHz] ultrasonic sound waves from the gold foil of the transducer. These waves fill a cone-shaped area about 15 to 20° off the axis of the centerline of the beam. The motion detector uses the Doppler Effect to detect the echo of these ultrasonic waves returning to it. The equipment measures how long it takes for the ultrasonic waves to make the trip from the motion detector to an object and back. Using this time and the speed of sound in air (at room temperature), the distance to the nearest object is determined. It should be pointed out that the motion detector will report the distance to the closest

object that produces a sufficiently strong echo. Objects such as chairs and tables in the cone of ultrasound can be picked up by the detector. Its minimum range of object detection is about 0.15 [m] and maximum range is about 6 [m]. /29/

In the experiments, two motion detectors are connected to the digital channels of Vernier LapPro® data-acquisition interface, which is in turn connected to the USB port of a laptop computer running Logger Pro software, see Figure 10.

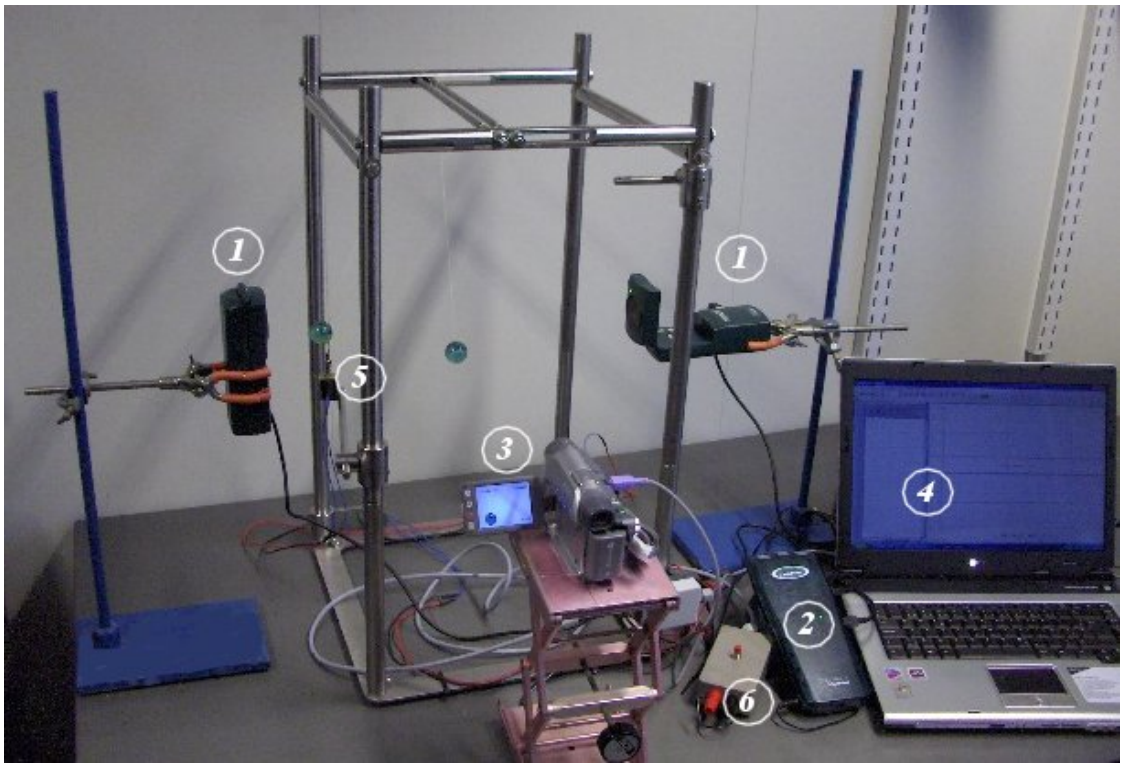

Figure 10 *Experimental setup with the ultrasound motion detector installed*: ① *motion detector*; ② *Vernier LapPro® interface*; ③ *digital video camera*; ④ *Vernier Logger Pro software*; ⑤ *relay*; ⑥ *relay release switch*.

The data collection starts simultaneously when the relay switch is pressed to release the ball. The collection time period length and sampling rate are set in the program according to the experiment's need. The data collected is represented graphically as a plot in Logger Pro or as a data table. A screen shot from the program's results is shown in Figure 11.

The motion detector used in the experiments for velocity measurements has some limitations. First, at high impact velocities it could not predict accurately the resulting post impact velocity of the ball. Secondly, the balls used in the experiments are quite small to be adequately detected by the motion detector and their round shape makes it tricky for the detector, which works better for more flat objects. Lastly, the moving ball went sometimes out of the motion detector's range, which gave inaccurate results. Nevertheless, it was noticed that the motion detector works well when the ball is swinging at low speeds.

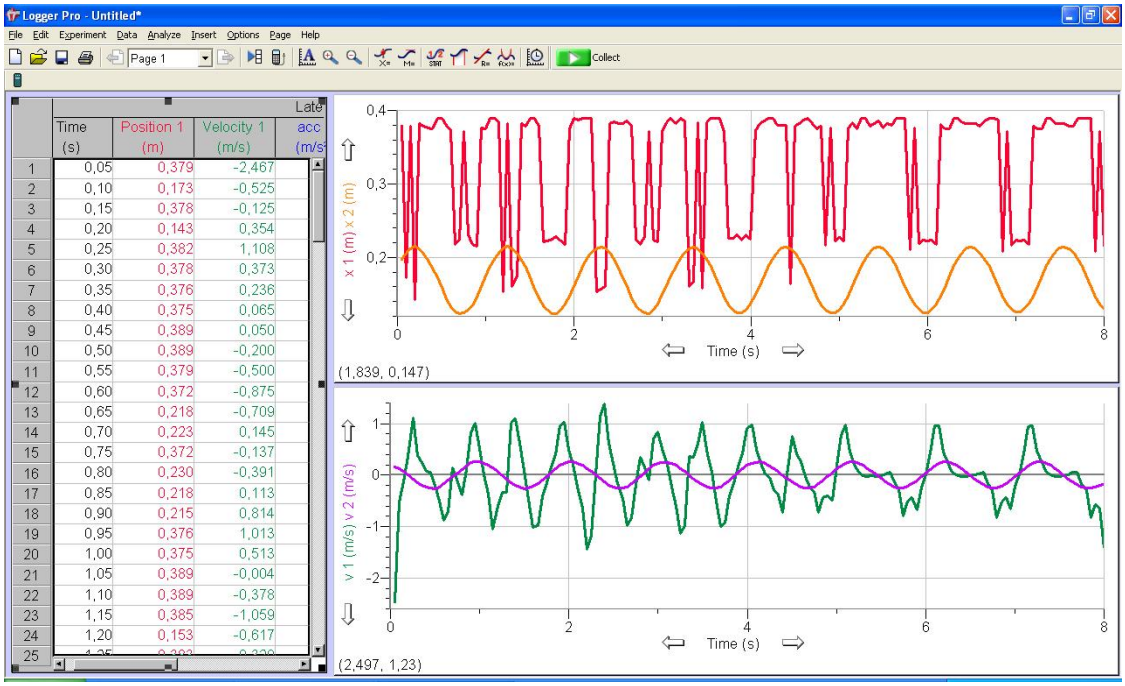

Figure 11 *A screen shot of collision data obtained from Logger Pro Software.*

2.5.4 Analysis of Experiment Results

We carried out a series of experiments that cover combination of a wide selection of ball sizes and material properties at different impact velocities. For the purposes and scope of this thesis, the main focus is on glass beads, the physicist's equivalent of sand. Other materials like steel and coated steel balls were considered for comparison of the results with glass balls and for a concurrent research that was taking part at same time as this work, see reference /67/. The chemical and physical properties of the glass balls (Sigmund Linder GmbH, Germany) are summarized in Table 2.

Table 2 *Material properties of glass balls.*

Properties	**Symbol**	**Value**
Elastic modulus	E	6.3×10^{10} [Pa]
Density	ρ	2390 [kg/m^3]
Poisson's ratio	ν	0.244
Short-time shear modulus	G_0	2.53×10^{10} [Pa]
Long-time shear modulus	G_∞	0 [Pa]
Decay constant	β	5.9666×10^3 [s^{-1}]
Relaxation time	τ	1.6760×10^{-4} [s]
Chemical composition	SiO_2	66 %
	Na_2O	16 %
	CaO	7 %
	Al_2O_3	5 %
	Bi_2O_3	3 %
	Others	3 %

Here, the aim is to investigate the relationship that ties the two quantities, i.e. impact velocity and the coefficient of restitution. This relationship is recognized by many researchers (Gorham and Kharaz, 2000; Rosa *et al*; 1999; Labous *et al*,1997 and Brilliantov *et al*, 1996). From theses studies, it is speculated that granular flow properties may depend on the details of the contact force model that is used to describe the grain collision process accurately. /30/

In the first set of experiments, relatively large monosize glass balls of 22.1 [mm] diameter and 14.2 [g] average mass are brought in contact by collision using Newton's cradle devise. Table 3 below presents the results of impact velocity and restitution coefficient for this test. The results of collision tests for medium and small monosize glass balls are shown in Tables 4 and 5 respectively.

Table 3 *Collision test data for large monosize glass balls.*

Measurement No.		**Impact Velocity v_{imp} [m/s]**		**Coefficient of Restitution e**	
1		0.524		0.986	
2		0.657		0.960	
3		1.172		0.943	
4		1.329		0.919	
5		1.609		0.903	
Material 1	Glass	m_1	14.3 [g]	d_1	22.1 [mm]
Material 2	Glass	m_2	14.1 [g]	d_2	22.1 mm

Table 4 *Collision test data for medium monosize glass balls.*

Measurement No.		**Impact Velocity v_{imp} [m/s]**		**Coefficient of Restitution e**	
1		0.626		0.979	
2		1.103		0.950	
3		1.407		0.840	
4		1.495		0.830	
Material 1	Glass	m_1	5.3 [g]	d_1	15.9 [mm]
Material 2	Glass	m_2	5.3 [g]	d_2	15.9 [mm]

It can be concluded from these results that the coefficient of restitution decreases with increasing impact velocity. A nonlinear dependence of the coefficient of restitution on the impact velocity is remarkable, which confirms with previous studies made by Bridges *et al*, 1984, Brilliantov *et al*, 1996 and Gugan, 2000. The size of the particle has no significant effect on the final value of the restitution coefficient. Additional experimental data from collision tests for multisize balls and different ball materials than glass is included in Appendix 1. /31/

Table 5 *Collision test data for small monosize glass balls.*

Measurement No.	Impact Velocity v_{imp} [m/s]	Coefficient of Restitution e
1	0.686	0.958
2	0.886	0.952
3	1.314	0.951
4	1.400	0.947
5	1.547	0.944

Material 1	Glass	m_1	1.3 [g]	d_1	10 [mm]
Material 2	Glass	m_2	1.3 [g]	d_2	10 [mm]

2.5.5 Simple Viscoelastic Material Models

The collision between deformable objects has been the subject of intensive investigation by many researchers using theoretical, numerical, and experimental methods. When plastic deformation of objects is involved, the collision and contact problem become so complicated that an accurate theoretical solution is difficult to obtain. /32/

Many real bodies, exhibit mixed behaviors of elasticity, viscosity, and plasticity. For better physical understanding of the equations of state of real materials, it is sometimes easier to visualize them in terms of elements analogous to mechanical systems (e.g., springs, dashpots, or sliders). The spring, dashpot, and slider indicate the effect of elasticity, viscous resistance and friction respectively.

Rheological models of rigid body deformation have been developed to quantify the stress-strain relationship of materials under loading and/or unloading conditions. For some solid materials, treating the material body as an elastic spring suffices for many practical purposes. In classical elasticity, such a material body is referred to as a Hookean body, and it is considered to be a linearly viscoelastic material if the stress is proportional to strain at a given load. More elaborate rheological models exist and they

are built by a suitable combination of one or more springs and dashpots. The Maxwell model, for example, is composed of a linear spring in series with a linear viscous dashpot and it describes the stress relaxation of a viscoelastic solid to a first approximation. The Kelvin/Voigt model consists of a spring in parallel with a dashpot, and it better represents the creep behavior of materials that do not exhibit significant instantaneous strain upon loading or unloading, see Figure 12. However, neither model adequately represents the general behavior of a viscoelastic material where it is necessary to describe both stress relaxation and creep. The two models show a finite initial strain rate whereas the apparent initial strain rate for many materials is very rapid. Thus, a more complex system, like the standard linear solid model shown in Figure 12c, might be required. /33/, /34/

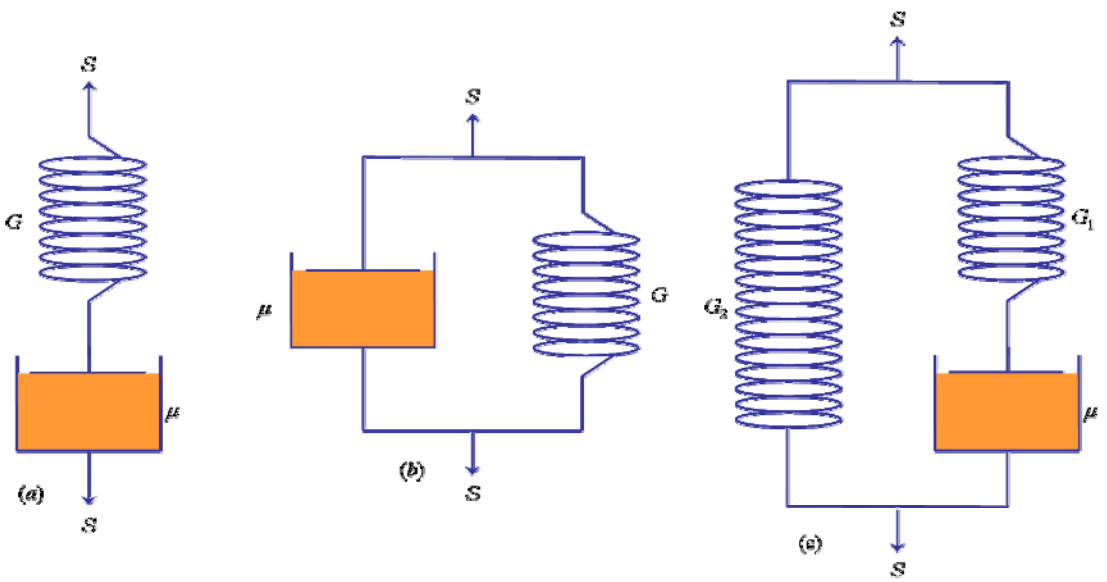

Figure 12 *Models for linear viscoelasticity*: (*a*) *Maxwell model*, (*b*) *Kelvin/Voigt model*, (c) *Standard linear solid model*. *Here*, *S is the shear stress*, μ *is viscosity coefficient*, *and G is the shear modulus.*

2.5.6 Finite Element Analysis

The glass balls used in the Newton's cradle experiment may be modeled as a viscoelastic material for which the shear relaxation modulus is assumed to be of the form:

$$G(t) = G_\infty + \left(G_0 - G_\infty\right)e^{-\beta t} \tag{31}$$

where t is time, G_∞ is the long-time (infinite) shear modulus, G_0 is the short-time shear modulus and β is the decay constant.

The dynamic response of a material modeled by one of the linear viscoelastic models mentioned above cannot be obtained analytically and numerical methods are, therefore, employed to carry out the analysis. Finite Element Analysis (FEA) is a software technique used to study stresses and strains on flexible parts or components. In the current work the nonlinear LS-DYNA code is used to model the transient dynamic event of collision between two deformable glass spheres.

LS-DYNA, by Livermore Software Technology Corporation (LSTC), is a suite of engineering simulation programs, based on the Finite Element Method (FEM), for analyzing the large deformation dynamic response of structures. A contact-impact algorithm allows difficult contact problems to be easily treated with heat transfer included across the contact interfaces. LS-DYNA contains an extensive library of material models and elements and it features many contact algorithms with a high level of accuracy. It contains approximately one hundred constitutive models and ten equations of state to cover a wide range of material behavior.

LS-DYNA comes with a third-party Finite Element Model Builder (FEMB) Developed by Engineering Technology Associates ETA, Inc., USA. ETA/FEMB is a general purpose pre and postprocessor that is comprised of three software modules all designed specifically for use with LS-DYNA. These programs are ETA/FEMB-PC preprocessor, ETA/PostGL, and ETA/Graph plot postprocessors. In addition, the original LS-PrePost postprocessor that comes with LS-DYNA was the main tool for conveying the results from LS-DYNA.

LS- DYNA has been used to simulate the first experimental measurement in Table 3. The spheres are modeled in three dimensions as a viscoelastic material (linear standard solid model) with material properties taken from Table 2. In building the simulation

model, elastic threads of polyethylene terephthalate material are used to connect the spheres at fixed points. This material is the same as the actual wire material used in the experiments. Boundary conditions are applied in order to constrain the motion of the threads, and hence the glass spheres, to be free in Cartesian coordinates only, without rotation. Figure 13 illustrates the user interface of ETA/FEMB Pre-processor where the geometry and the collision model are created.

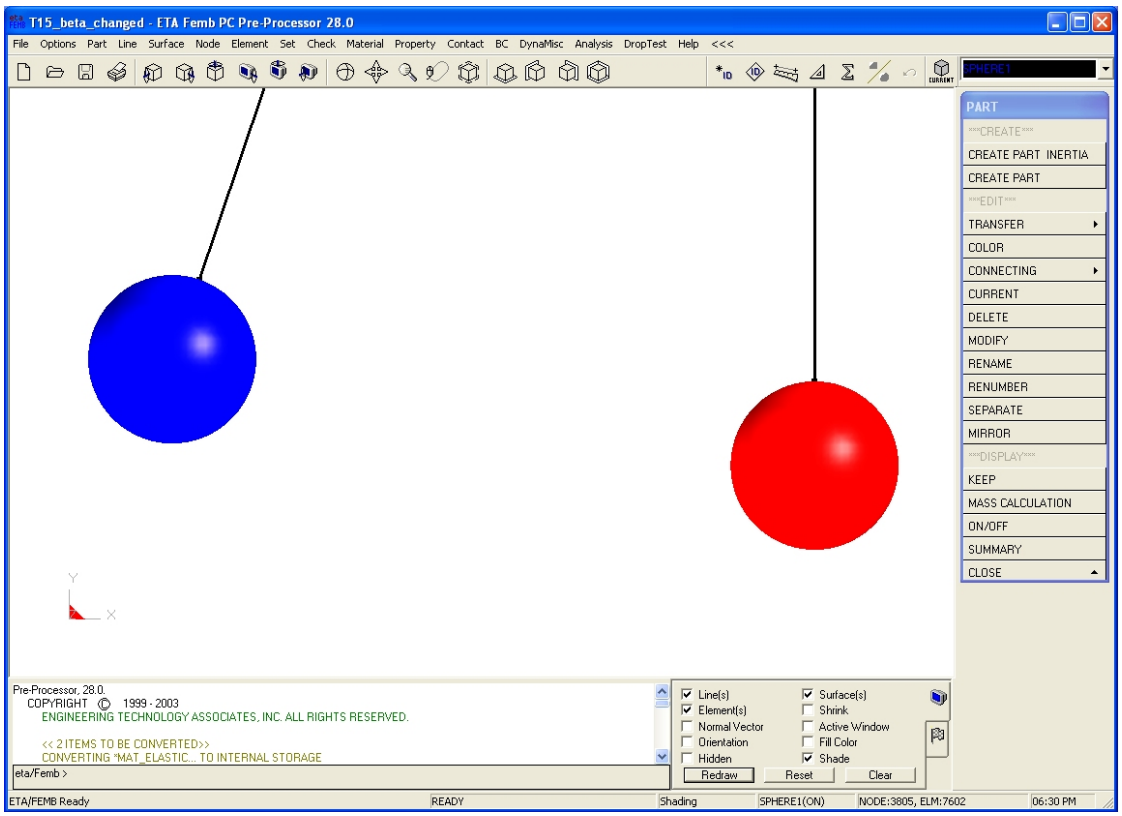

Figure 13 *Finite element model of collision between two identical glass balls developed in ETA/FEMB preprocessor version 28.0*

It is found from this model that the impact velocity is 0.5036 [m/s] and the coefficient of restitution is calculated to be e = 0.9293 with percentages of error of 3.91 % and 5.75 % respectively. The total processing time (CPU time) required to complete the simulation is 15.4 [h].

In order to simplify the simulation and reduce the computation time and error, new models are employed, in which the glass spheres are almost in contact with each other

instead of being far apart. These models represent the instant at which the left glass sphere impacts the one on the right side. Figure 14 shows an example of such a model and also shows the graphical window of LS-PrePost postprocessor. In these models, the left ball is given an initial velocity in only one direction (here taken as the *x*-direction) similar to its experimental counterpart, i.e. 0.524 [m/s] while the second ball is at rest. The glass balls are assumed to be smooth and therefore the friction between them is neglected. Also, air resistance and gravity are assumed to have a minor effect during the short time period of collision. Different material models that cover the basic models described in the preceding section are used to represent the glass balls. The finite element models are discretized by 61350 constant stress, 4-node tetrahedron solid elements with a total number of 11712 nodes.

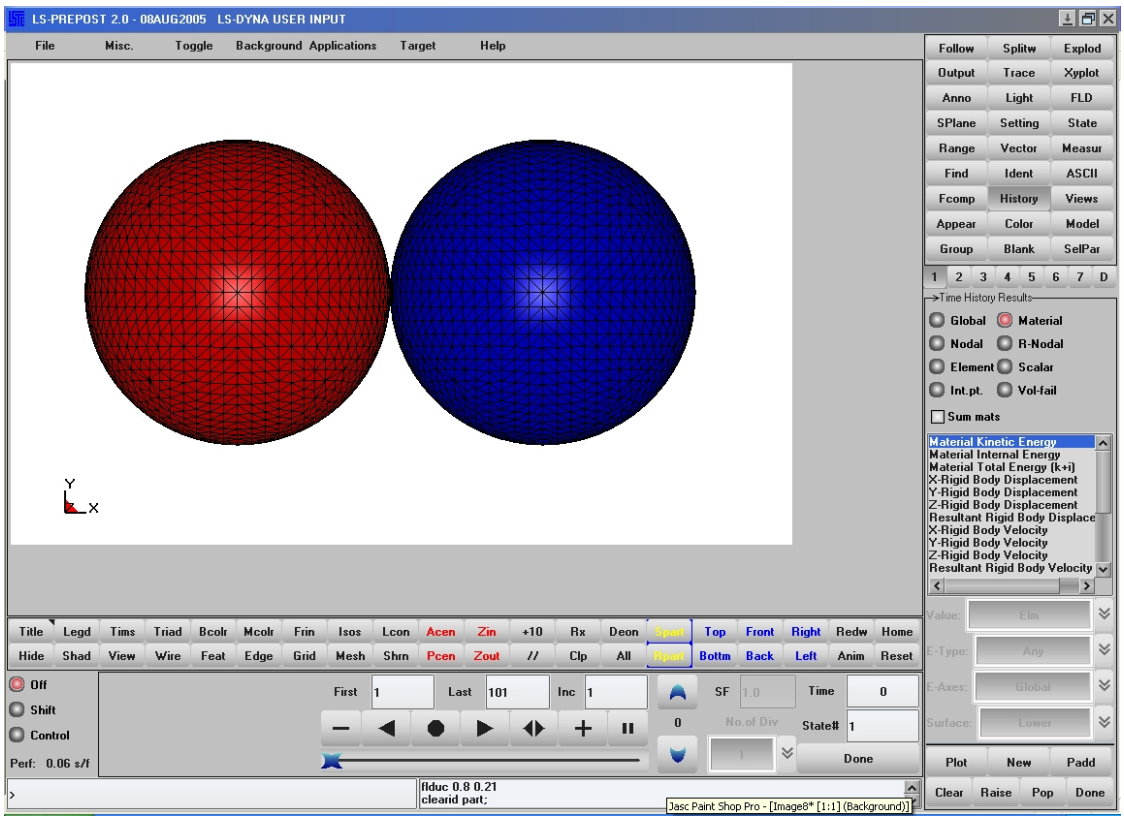

Figure 14 *New collision model showing the glass balls at the impact moment, the graphical interface is for ETA/PostGL.*

An important result from our dynamic FEA of collision between glass spheres is the coefficient of restitution, which is defined by Equation (26). The post-impact

velocities of the glass spheres are found from analysis of history plots of velocity versus time. Figure 15 illustrates the velocity output of LS-DYNA simulations. The results show that velocity of the left glass ball (Particle No.1 in the figures) decreases with time, while the right side ball velocity increases simultaneously until both velocities reach steady values. The points at which the velocities become constant define the collision time and indicate the end of collision. The collision time is approximately 8×10^{-5} [s] for the elastic, viscoelastic, and Maxwell models, and about $9.75\ 8 \times 10^{-5}$ [s] for Kelvin model. This difference may be attributed to the fast relaxation response of the elastic springs in the models and the delayed response in the dashpot due to its viscosity parameter.

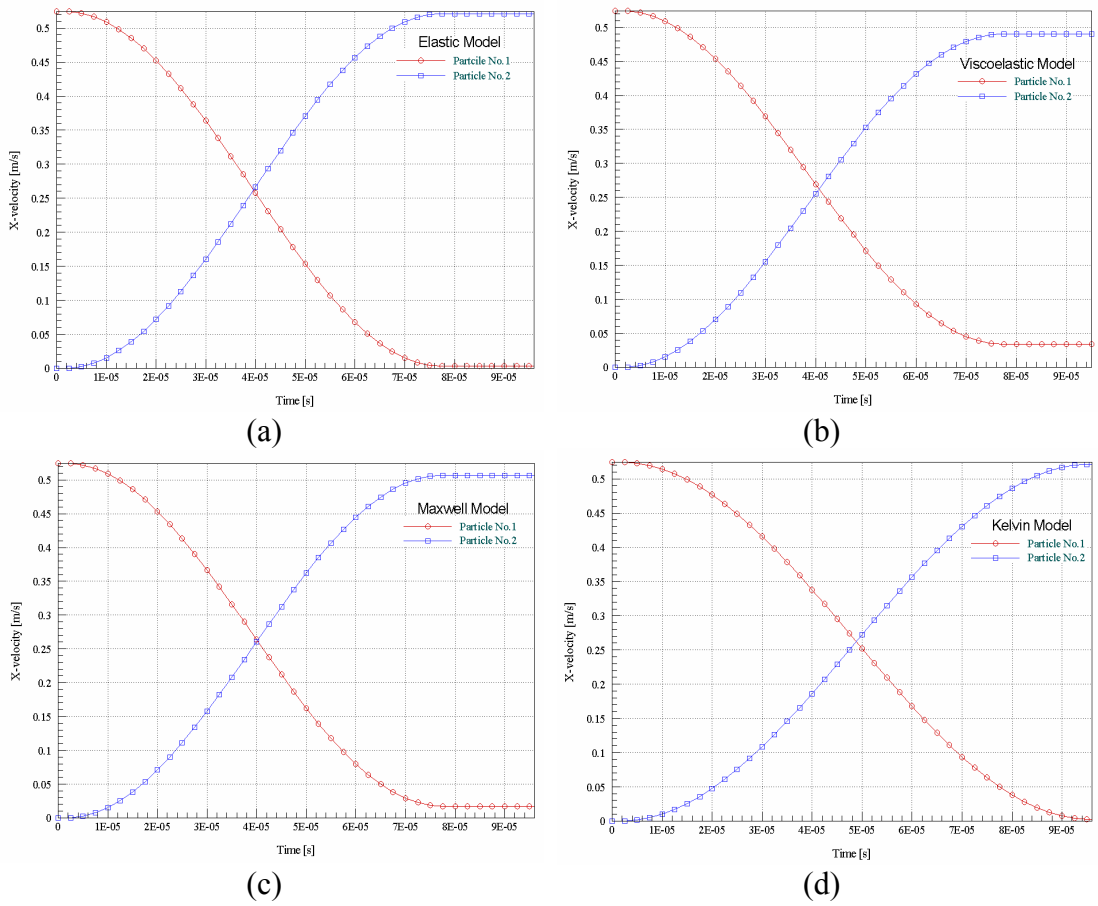

Figure 15 *LS-DYNA history plot of the x-velocity component when the glass balls material is represented by*: (a) *elastic model*; (b) *viscoelastic model*; (c) *Maxwell model*; (d) *Kelvin model*.

The highest material deformation occurs at the point where the velocity curves intersect each other, here the stress (pressure) has a maximum value and after that it decreases to some value depending on the model. It is beyond the scope of this thesis to discuss in depth the contact forces relationships; although a profound understanding of these relationships is crucial for studying impact.

Table 6 below summarizes the calculations of restitution coefficient for the various material models, obtained from LS-DYNA analysis. It shows the percentage of error in comparison with experiment. These results suggest that the elastic model is the closest model to describe sphere balls, since it has the minimum error. However, it should be remarked that the value of the viscous damping (decay) parameter (β) in viscoelastic, Maxwell, and Kelvin models is usually selected in advance before simulation starts. Changing this parameter to a different value alters the restitution coefficient. The amount of this change is not accurately predictable and further investigation need to be done by fitting the models to laboratory stress relaxation data. Also, the calculation of restitution coefficient is very sensitive to changes in velocity; a small difference in the velocity measurement can cause a considerable change in the value of restitution coefficient. This is especially important in the experimental setup, when the velocity is calculated from the geometry arrangement of the experiment.

Table 6 *Summary of LS-DYNA simulation results.*

	Elastic Model	**Viscoelastic Model**	**Maxwell Model**	**Kelvin Model**
υ_1 [m/s]	0.52409	0.52409	0.52409	0.52409
υ_1' [m/s]	0.00313	0.033572	0.017209	0.0026573
υ_2 [m/s]	0	0	0	0
υ_2' [m/s]	0.52096	0.49053	0.50689	0.52144
e	0.994	0.872	0.934	0.931
Error in e [%]	0.811	11.56	5.27	5.58
Collision time [s]	8×10^{-5}	8×10^{-5}	8×10^{-5}	$9.75\ 8 \times 10^{-5}$
CPU time [h]	2.17	2.15	3.07	1.73

3. DYNAMICS OF A SYSTEM OF PARTICLES

3.1 General Overview

In the previous chapter we have discussed the interaction between two spherical particles and computed the value of restitution coefficient from the experiment's geometry and by finite element analysis. However, industrial applications of granular materials usually involve thousands or millions of particles with different particle shapes and sizes. Normal as well as oblique contacts between particles are possible in such granular system. Theoretical analyses of granular flows examine frictionless inelastic spheres, but there exist no frictionless particles, just as there are no elastic particles, friction provides another mode of energy dissipation (in addition to inelastic collision). Moreover, air that fills the interstices between the solid particles can play a significant role in the transport of momentum between particles and it acts as a buffer film, preventing direct contact between the particle surfaces, an effect known as the "lubrication force". The air friction is usually neglected in simulation and in the interpretation of experiments. In contrast, granular systems in industrial processes, air resistance and buoyancy are often important, although the air effects can be, sometimes, neglected for large particles, say greater than 1 [mm], if the velocity is not too large and when air is not considered a determinant factor that affects dynamic and static properties of the system. /17/, /35/, /36/

The previous work on vertical vibration of granular materials has focused on showing that a number of complex phenomena exist. On the other hand, detailed measurements of the phenomena and the mechanisms that cause them are still lacking. The aim of this chapter is to help fill this gap and provide some information by characterizing the collective behavior of a vertically vibrated dense granular medium maintained in a steady state regime using experiment and simulations designed for this purpose.

3.2 Vertical Vibration of Granular Materials

It has been shown experimentally that many interesting flow patterns appear when beds of granular materials are subjected to external, vertical oscillations, see Figure 16. Chlandi (1787) was perhaps the first to systematically study the behavior of vibrated bed of particles. He found that when sand is scattered on a vibrating

membrane, the sand particles collect in heaps corresponding to the vibration anti-nodes. Faraday (1831) also examined these patterns and found that particles move in circulation patterns within the piles. He related the granular convection to the trapping of interstitial fluid. Heaps and convection cells similar to those described by Faraday have been reproduced in a number of experimental devices. Faraday's experiment used a vibrating membrane with fixed boundaries giving rise to vibration amplitudes. Other researchers have found equally interesting phenomena using rigid vibrating bases with both fixed and oscillating side wall boundaries. /13/, /17/

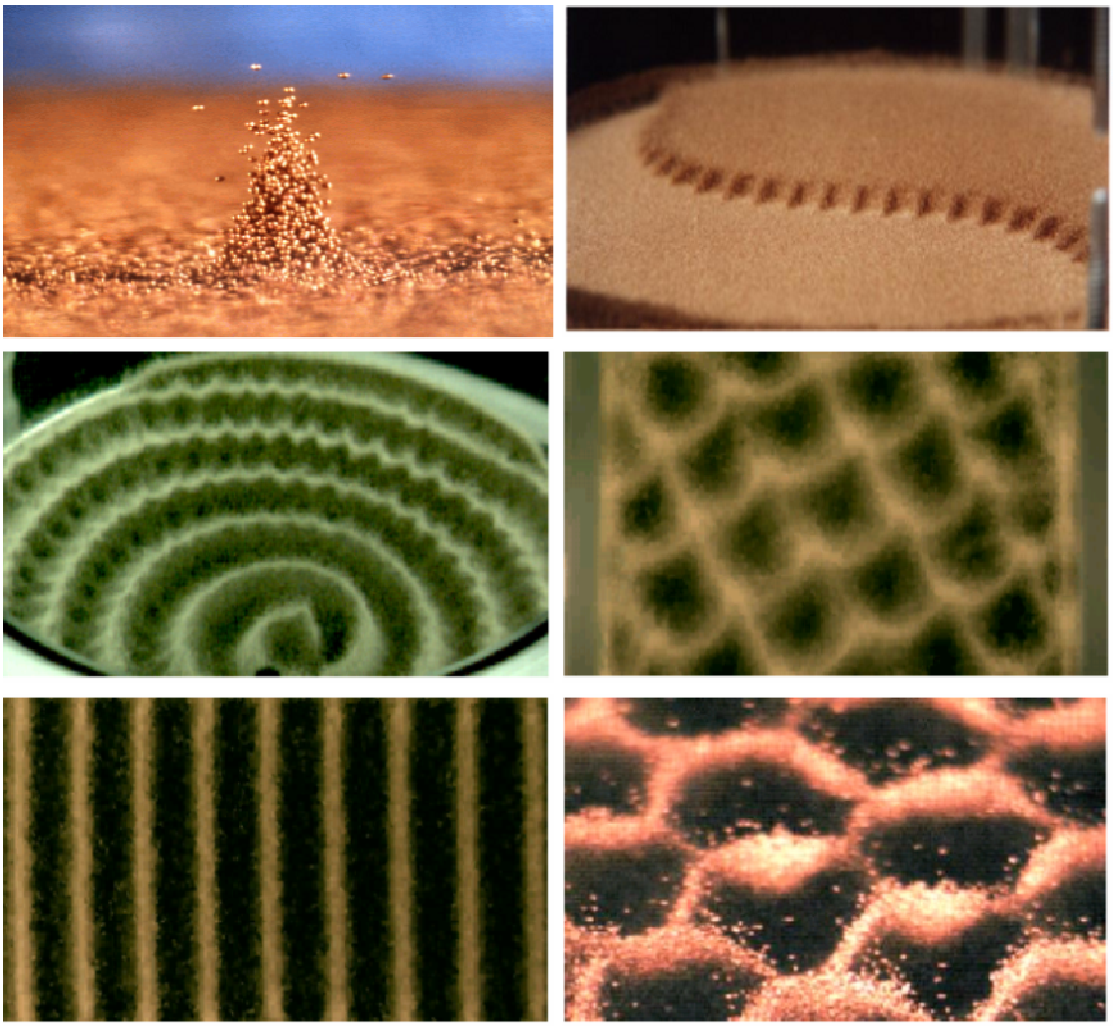

Figure 16 *Pattern formations in vertically oscillated granular layers*. /37/

Granular materials vibration is also encountered in many practical applications like drying, mixing, and separation processes. It is commonly used in industrial settings as an aid to handling and transporting particulate materials such as foodstuffs, coal, and

pharmaceuticals. Examples of devices that often utilize vibration include conveyor belts, hoppers, sorting and packing tables, fluidized beds, and drying plates. Vibration of a granular material may also play an important role in natural events such as earthquakes and avalanches. Therefore, clearly knowing how a granular material responds when subjected to vibration can provide valuable design information. For example, in fluidized bed reactors a quantitative understanding of the hydrodynamics of fluidization is needed for the design and scale-up of efficient new reactors in the petroleum, chemical, and power generation industries./13/, /36/

In spite of the resurgence of interest in granular science and the large number of theoretical and experimental studies, a poor understanding still remains of how granular materials behave in general. For instance, while fluids are processed in industry with high efficiency, the efficiency of handling and controlling granular materials is estimated to be well below optimum. Still, much of the knowledge on how to maneuver particulates is empirical and a standard approach to analyze rapid granular flows needs to be developed. /13/, /35/

3.3 Experimental Techniques for Studying Granular Materials

Experimental observations of granular flows were naturally limited due to the difficulties of obtaining information from deep within the bed and complications caused by the opacity of the material. As a consequence, most work on granular convection in three dimensions has focused on external features of the flow, such as heaping. Alternatively, individual particles can be easily tracked in two-dimensional systems. The applicability of results from these studies to actual three-dimensional flow is, however, limited because of the additional frictional interactions with the front and back container walls and by phenomena that is unique to flows in two dimensions.

Fully three-dimensional flows have earlier been studied invasively with tracer particles or with aggregate probes such as capacitance and mutual inductance, and diffusing-wave spectroscopy. Noninvasive low-resolution imaging techniques like x-rays, and radioactive tracer particles have also been used, but neither approach has resulted in an established tool for the study of granular flows.

Recently, Magnetic Resonance Imaging (MRI) and Positron Emission Particle Tracking (PEPT) have been successfully applied as high-resolution, noninvasive probes for studying granular dynamics. The PEPT and MRI methods are complementary as the former traces the motion of a single tagged particle over long rime, while the later measures nearly instantaneous averages of motion of many particles. In this way we are able to measure the density and granular temperature profiles of the system. /16/, /38/–/41/.

3.4 Procedure and Setup of the Vibro-Fluidized Bed Experiment

Figure 17 below shows schematics of the experimental setup that we used to study vertical oscillation of granular layers. The device consists of a plastic cup filled with spherical glass beads and fixed at the center of a thin, 0.5 [mm], circular aluminum plate of 170 [mm] diameter that is mechanically coupled to a loudspeaker. A function generator (Good Will Instruments, model GFG-8216A) is used to provide an input sinusoidal signal of adjustable frequency and amplitude to a 500 [W] power amplifier (IMG Stage Line by Monacor® International) which in turn amplifies and transmits the signal to the loudspeaker.

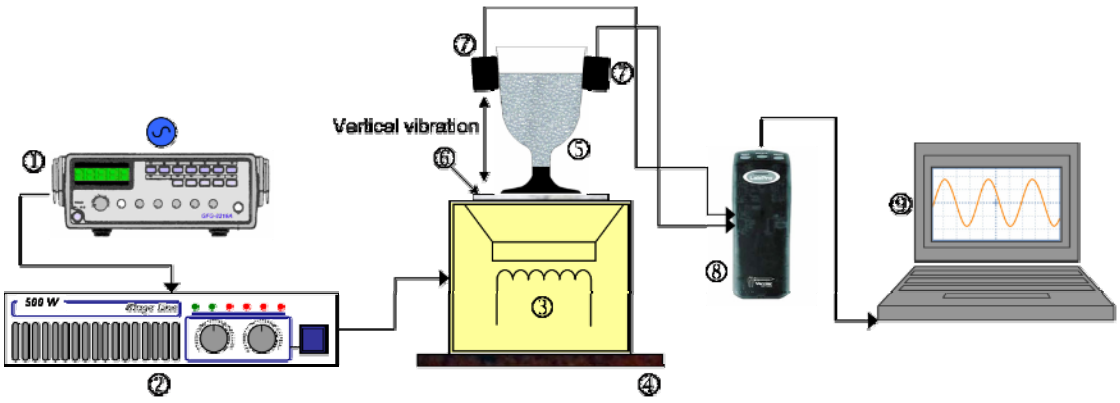

Figure 17 *A schematic drawing of the apparatus used for studying the vertical vibration of glass beads*: ① *function generator*; ② *audio amplifier*; ③ *loudspeaker*; ④ *heavy metal support base*; ⑤ *polystyrene cup containing the glass beads*; ⑥ *thin aluminum plate*; ⑦ *accelerometer*; ⑧ *Vernier LapPro® interface*; ⑨ *laptop computer running Vernier Logger Pro program*.

The acceleration of vibration in the vertical direction could be precisely monitored by means of two accelerometers (Vernier Software & Technology, models LGA-BTA and ACC-BTA) mounted on board of the container. The accelerometers are of two types:

- A Low-*g* (low-gravity) accelerometer measures small accelerations in the range of -5 *g* to +5 *g* with minimal electric noise. *g* is the acceleration due to gravity at the Earth's surface, 9.81 [m/s^2]. The noise is typically on the order of 0.5 [m/s^2] peak to peak and the frequency response of the accelerometer is 0-100 [Hz].
- The 25-*g* accelerometer measures accelerations in the range ±250 [m/s^2] (±25 *g*). The accuracy of this accelerometer type is 2.5 [m/s^2] peak to peak and the frequency response is the same as that of the Low-*g* accelerometer. /42/

Two accelerometers are used because it was not clear beforehand the acceleration range of interest and also for comparison between the results. The measurement of the two accelerometers is nearly the same and within the accuracy range of each sensor. In addition, the accelerometers served as counter weights to balance the cup in the vertical direction. A data acquisition system (Vernier LapPro®) acquires the measured acceleration from the accelerometers and transfers the digitized output via USB link to a laptop computer for analysis with Vernier Logger Pro software.

All vibro-fluidized bed experiments were conducted in a polystyrene vessel which has a variable round cross section with a maximum inner diameter of 65.68 [mm] at the top, and 99.1 [mm] height. The shell thickness of the vessel is 0.95 [mm]. This vessel stands on a 10.73 [mm] height base made from polypropylene (shown in black color in Figure 17. There is no particular reason to adopt this container shape; one can use a rectangular or a circular cylinder as done in most vibro-fluidized bed experiments. It is important to recognize, however, that the geometry of the container has a direct influence on the dynamic behavior of granular materials.

Spherical glass beads (manufactured by Sigmund Linder GmbH, Germany, Type-S SiLi) which have a homogeneous smooth surface with high roundness and elasticity

are accepted as the granular material in the present experiments because they have similar properties to sand, the commonly used material in fluidized bed combustion systems. The properties of these beads are illustrated in Table 7. In each experiment, the glass beads were weighted and the container was filled to a height h_f with bead samples of diameters in the range $0.1 \leq d \leq 1.25$ [mm]. The media was partially compacted by flattening the surface prior every test run. Care was taken to avoid electrostatic effects by sprinkling the container with an antistatic spray and changing the beads whenever they are seen to stick to the container walls.

Table 7 *Material properties of glass beads used in vibration experiments***.** /43/

Properties	**Symbol**	**Value**
Elastic modulus	E	63 [GPa]
Density	ρ	2500 [kg/m^3]
Average bulk density	ρ	1487.5 [kg/m^3]
Roundness	—	≥ 95 %
Chemical composition	SiO_2	70.00 %
	Na_2O	13.1 %
	CaO	8.72 %
	MgO	4.10 %
	B_2O_3	2.65 %
	K_2O	0.27 %
	SO_3	0.21 %
	Others	0.95 %

The height of the granular bed at rest divided by the bead diameter defines the normalized layer depth, which is a measure of the number of particle layers, and it's given by:

$$N_\ell = \frac{h_f}{d} \tag{32}$$

When the power is turned on, the sinusoidal audio signal from the power amplifier causes the loudspeaker to shake the aluminum plate up and down and accordingly at a certain time the glass beads in the plastic cup start to have a periodic macroscopic motion.

The deriving sinusoidal oscillation has the following form:

$$Z(t) = A\sin(\omega t) \tag{33}$$

where, $\omega = 2\pi f$ is the angular frequency, f is the vibration frequency, and A is the amplitude of vibration. A representative profile of the signal obtained from the accelerometers is shown in Figure 18.

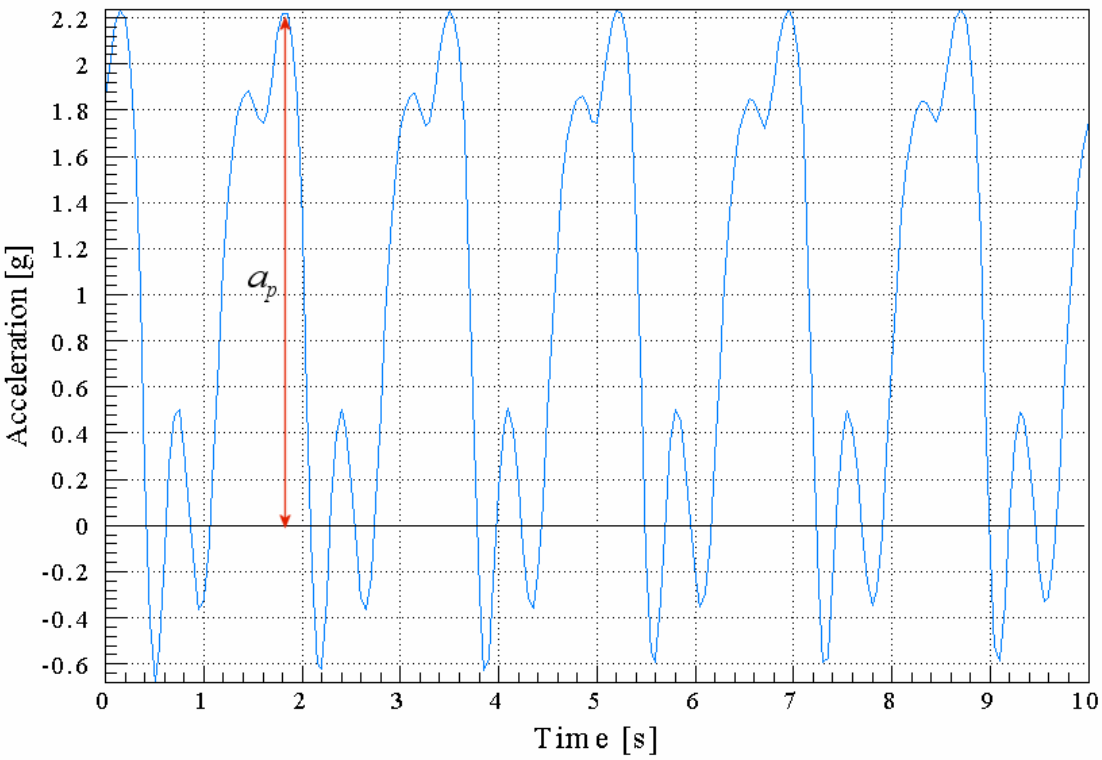

Figure 18 *A typical vibration acceleration signal measured by the accelerometers mounted on the container and plotted in Vernier Logger Pro software.*

The sine wave frequency from the function generator could be controlled to within ± 0.3 [Hz], but the distortion from the original sinusoidal input is due to the dynamic response of the vibrating device under the applied load. The vibration strength can be characterized by the dimensionless acceleration (Froude number):

$$\Gamma = \frac{A\omega^2}{g} = \frac{a_p}{g}, \qquad \left[a = \frac{dZ^2}{dt^2} = -A\omega^2 \sin(\omega t) \right] \tag{34}$$

where a is the acceleration of vibration and $a_p = A\omega^2$ is the peak amplitude of the acceleration. Γ measures the maximal acceleration given to a particle in contact with the vibrating cup and for $\Gamma < 1\ g$, the ground layer will always be in contact with the cup bottom. /44/

While amplitude is the control parameter most cited in the literature about vertical vibration of granular materials, the frequency also has an effect on the flow. Throughout the experiments reported here, Γ is varied by changing ω at fixed A. In a typical run we increased the frequency slowly and observed the evolution of the system from a solid state at rest to a liquid state. The transition occurs when the frequency exceed a certain threshold value f_c that corresponds to a critical Froude number Γ_c and critical amplitude A_c. The experimental results are discussed in the following section

3.5 Experimental Results

The experiments were performed on two granular bed depths: a deep bed and a relatively medium-sized bed. The deep bed has a mass of 143 [g], while the medium size bed has half of the mass of the deep bed, 71.5 [g]. The results of the experiments are summarized in Table 8, in which each data represents the average of five separate experimental runs.

From the first column in this table, note that we have a polydisperse system since the size of the glass beads is variable, and the beads are provided by the manufacturer to have a range of diameters between two fixed values, except for the 100 micron beads. Therefore the calculations in the table are based on the average diameter of the beads

($\bar{d}$). The approximate number of particles in the bed is estimated by using the following equation:

$$N = \frac{m_{\text{bed}}}{m_{\text{particle}}} = \frac{m_{\text{bed}}}{(\pi/6)\rho\bar{d}^3} \tag{35}$$

where m_{bed} is the mass of the bed, and m_{particle} is the mass of a single glass bead.

Table 8 *Summary of the vibro-fluidized experimental results.*

Deep Bed								
Particle Diameter	Average Particle Diameter	Static height of the Bed	Number of Granular Layers in particle diameters	Approximate Number of Particles	Average Peak Critical Acceleration Amplitude	Dimensionless Acceleration	Average Threshold Frequency	VerticalVibration Amplitude
d [mm]	$\bar{d}$ [mm]	h_f [mm]	N_ℓ [−]	N [−]	a_{pc} [m/s^2]	Γ_c [−]	f_c [Hz]	A [mm]
0.1	0.1	66.07	660.70	1.09×10^8	22.22	2.27	38.66	0.38
0.25 − 0.50	0.375	67.25	179.33	2.07×10^6	21.42	2.18	35.75	0.42
0.50 − 0.75	0.625	70.00	112.00	4.47×10^5	18.04	1.84	34.41	0.39
0.75 − 1.00	0.875	70.17	80.19	1.63×10^5	17.54	1.79	34.46	0.37
1.00 − 1.25	1.125	70.30	62.49	7.67×10^4	18.69	1.90	34.30	0.40
Medium Bed								
d [mm]	$\bar{d}$ [mm]	h_f [mm]	N_ℓ [−]	N [−]	a_{pc} [m/s^2]	Γ_c [−]	f_c [Hz]	A [mm]
0.1	0.1	51.42	514.20	5.46×10^7	22.05	2.25	41.95	0.32
0.25 − 0.50	0.375	52.02	138.72	1.04×10^6	21.75	2.22	41.45	0.32
0.50 − 0.75	0.625	52.20	83.52	2.24×10^5	19.43	1.98	40.27	0.30
0.75 − 1.00	0.875	52.28	59.75	8.15×10^4	17.66	1.80	38.81	0.30
1.00 − 1.25	1.125	52.45	46.62	3.84×10^4	18.10	1.85	39.02	0.30

The crossover from solid to a uniform fluidized state under vertical vibration is observed to occur at around $\Gamma_c = 2\ g$ for both deep and medium depth beds, as reflected from the table results. However, there is a quite obvious difference in the critical frequency between the two regimes, at which the system undergoes transition from solid to fluid state.

Above the critical dimensionless acceleration a single peak of granular media is noticed to appear on one side of the container. The heap is associated with a steady particle convection pattern in which particles avalanche down the free top surface of the heap where they are subducted at its lowest point, and then they re-circulate internally back to the peak. de Gennes (1966) has proposed a theoretical approach to this instability based on a series of alternative passive and active regimes:

- Passive regime: when the container is raised up, the beads are compacted so that no possible intergranular motion is allowed and the bead heap can be considered as a solid.
- Active regime: when the container is carried down, with an acceleration a of the container larger than the acceleration of gravity, the bead granular system is fluidized.

In addition, de Gennes introduced a mechanism which limits the increase of bumps at the interface. During the passive fraction of the period, the granular material behaves like a solid. So, the slope of any bump cannot pass the maximum value for the angle of repose of the bead heap at equilibrium. The excess of matter which has been raised up on bumps during the active lapse of time will then flow as an avalanche downward during the passive regime. Hence, de Gennes model predicts the existence of a permanent surface flow of particles, as it is observed experimentally. /45/

The average peak acceleration amplitude at the resonance frequency is calculated from the accelerometers signal over a period of 10 [s]. At this frequency, the container was shaken rigorously and the collision between the particle bed and the container walls produced a high-frequency noise in the accelerometers output signal that could not be isolated. Consequently, the final output signal was sometimes distorted from its

original sinusoidal input and it had strong fluctuations. This may explain the controversial results in the dimensionless acceleration amplitude obtained for the 0.875 [mm] and 1.125 [mm] average bead diameters, since Γ_c (or a_{pc}) appear to decrease with increasing particle diameter (or with decreasing granular layers: $d \propto 1/N_\ell$), see Figure 19. The amplitude of vibration A remains approximately constant throughout the entire experiment, as expected. Figure 20 shows a plot of the dimensionless bed depth against the critical frequency. From this figure it is seen that an increase in the particle depth results in a corresponding increase in the critical frequency. Moreover, it is noticeable the medium bed has a higher critical frequency than the deep bed at the same particle size.

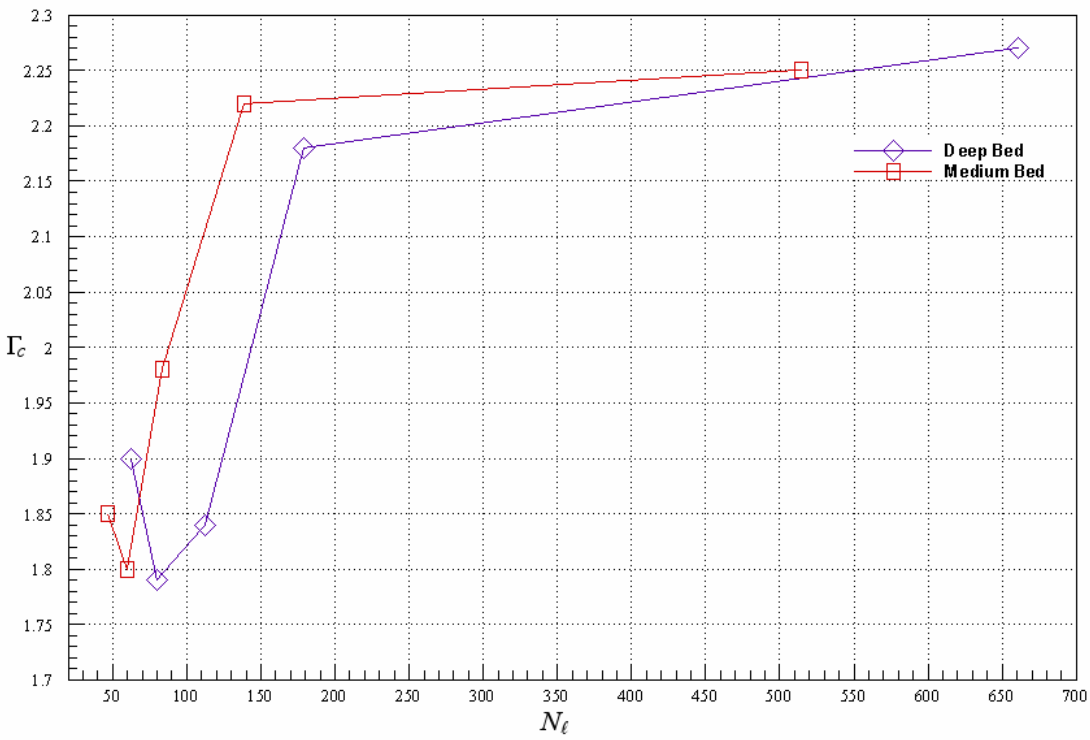

Figure 19 *A plot of the number of granular layers versus the critical dimensionless acceleration for deep and medium-sized beds.*

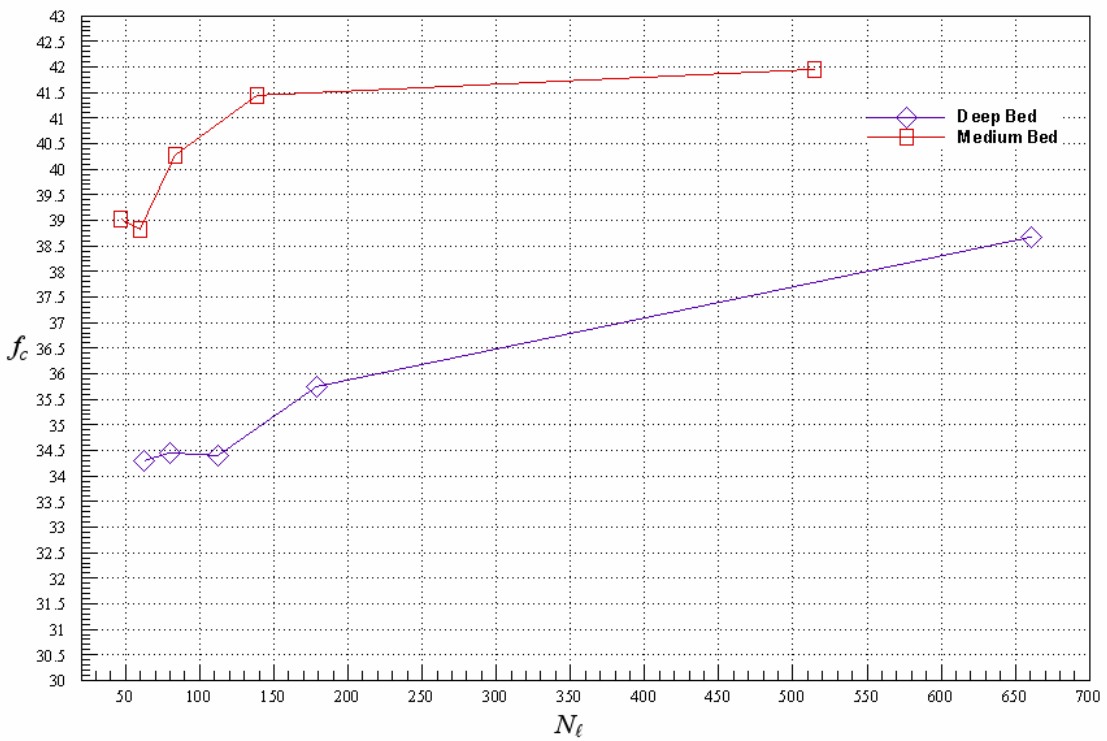

Figure 20 *A plot of the number of granular layers versus the resonance frequency for deep and medium-sized beds.*

3.6 Discrete and Continuum Formulation of Granular Flows

3.6.1 Introductory Remarks

It is well known that in a normal fluid in the gravitational field free convection can occur if the externally applied vertical temperature gradient is directed downwards and its magnitude exceeds a certain value. The mechanism for this convection is buoyancy due to thermal expansion. In vibro-fluidized granular systems some physical mechanisms for convection have been proposed. One is the friction of the grains with the walls of the container for weakly excited systems, and another is the buoyancy (or heat) -driven mechanism for fully-fluidized systems. The theoretical techniques used to describe convection and granular flows have mainly been the continuum hydrodynamic theory and large-scale molecular dynamic simulation that is based on the discrete particle kinetic theory. These models are referred to as granular hydrodynamics. /17/, /46/

3.6.2 Computer Simulation and Modeling Methods

A resurgence in granular materials research occurred in the early 1980s. Part of this renewed interest may be associated with the recent advancements in computer simulations for the study granular flows. Prior to the 1980s, computer processing speed and data storage capabilities were too limited to study systems of thousands of particles. However, with the rapid growth in processor speed, which was followed by a decrease in hard drive and memory costs; and the development of parallel processing, numerical simulations and computer models have become an increasingly effective tool for studying granular materials.

Simulations offer several advantages for studying granular flows. Perhaps the most significant is that the state of the particulate system is known at all times in a simulation. Hence, measurements that might be difficult to make in experiments are easier to perform in simulations; in addition, the interior of a flow can be examined. Simulations can also model environments that are not easily produced in experiments. For example, many simulations are performed with altered gravity environments or with frictionless particles. Reliable simulation tools can provide valuable insights for understanding how granular materials behave and, as a result, accelerate the achievement of substantial industrial process improvements incorporating particle flows. /47/, /49/

Models describing particle flows can be roughly divided into two groups: Lagrangian models and Eulerian models. Lagrangian models describe a discrete phase of the particles and calculate the path and motion of each particle by using specified collision rules for particle interactions. The Eulerian models treat the particle phase as a continuum and the existing phases as interacting continua. These models have their own advantages and disadvantages, depending on the details and environment of each model. /47/, /53/

3.6.3 Lagrangian Models

Lagrangian models are referred to in literature by other names like the Discrete (or distinct) Element Models (DEM); Particle Element Models (PEM) and Discrete

Particle Method (DPM). DEM is analogous to the finite element method in that it represents the macroscopic properties of the material, but unlike the FEM, each element in DEM can move freely. The discrete methods treat the particle flow as an assemblage of particles interacting through their contacts (or collisions). The individual granular particle is considered as an element which obeys the viscoelastic equation (normalized by mass):

$$\frac{\vec{F}}{m} = \ddot{\vec{x}}_i = -\sum_{j=1}^{N} \theta\left(d - \left|\vec{x}_i - \vec{x}_j\right|\right)\left[k_0\left\{\vec{x}_i - \vec{x}_j - d\frac{\vec{x}_i - \vec{x}_j}{\left|\vec{x}_i - \vec{x}_j\right|}\right\} + \gamma\left(\vec{\upsilon}_i - \vec{\upsilon}_j\right)\right] - \vec{g} \tag{36}$$

where the indices i and j indicate the particles, N is the total number of particles, $\vec{x}_i$ is the position vector of the ith particle, $\vec{g}$ is the gravity acceleration, and $\vec{\upsilon}$ is the velocity. Each particle has a diameter d. Because of the Heaviside step function $\theta(\vec{x})$, particles interact only when they contact with each other, which represents the discrete nature of the granular matter. k_0 and γ are the elastic constant and the phenomenological dissipation (damping) coefficient respectively. These viscoelastic material constants give the coefficient of restitution, e, and the collision time t_{col} when the two particles collide:

$$e = \mathrm{e}^{(-\gamma\pi/\omega)}, \qquad t_{\text{col}} = \frac{\pi}{\omega}$$
$$\omega = \left(2k_0 - \gamma^2\right)^{1/2} \tag{37}$$

As mentioned in earlier part of this thesis, various methods have been used to simulate large amounts of particles using interaction models like the one given in the above expression. Molecular Dynamics (MD) simulations of hard and soft particles are perhaps the most common DEM simulation techniques applied to model the granular flow in vibro-fluidized beds. These methods are based on the resemblance of rapid flows of granular materials to classical fluids and the success of kinetic theory of dense gases in understanding equilibrium of fluids. /19/, /48/

Although the concepts of MD simulations are straight forward, there are several important issues that must be considered. First, the simulation environment must be addressed. This includes whether the simulation is two- or three-dimensional, how many particles will be included in the simulations, what types of forces will be considered, and what boundary conditions are most appropriate. Next, consideration must be given as to how to model the particles and forces and what physical constants should be used. Lastly, the numerical scheme for integrating the equations of motion must be addressed. Since in this research we are performing rather Eulerian type of simulations, we will only consider the relevant issues in the Lagrangian simulations, i.e. issues related to friction, restitution coefficient and drag. One is referred, e.g., to /13/, /19/, and /47/ for more details describing the other issues. /13/

Many MD simulations and theoretical analysis of granular media consider frictionless (perfectly smooth) spherical particles. Conversely, MD simulations comparing the behavior of frictional and frictionless particles reveal that smooth particle models only partially capture the physical properties of granular flows and the effect of friction cannot be compensated by increasing the dissipation (decreasing e); thus friction is merely an additional mechanism of dissipation. Even a small amount of friction increases the overall dissipation significantly, not because the frictional dissipation is significant in each collision, but because the friction reduces the grain mobility and increases the overall collision rate. /35/

The restitution coefficient is often taken to be a constant in MD simulations, but a constant value of e can lead to "inelastic collapse", where particles undergo an infinite number of collisions in a finite amount of time. In fact, physically, e must approach unity as the relative normal velocity $\upsilon_n = \upsilon_{ij} = \upsilon_i - \upsilon_j$ approaches zero (the elastic limit). /35/

In vibro-fluidized systems the interaction force between the solid and fluid phases is mainly attributed to the fluid drag, still, the effect of interstitial fluid (e.g. air) is, generally, ignored in molecular dynamics simulations. The fluid drag force acting on individual particles represents the interphase momentum transfer, which is one of the dominant forces in the gas-phase momentum balance. This force depends not only on

the relative velocity between particles and the interstitial fluid, but also on the presence of other particles surrounding them. It is extremely difficult to determine this force analytically and experimentally due to difficulties in describing multibody interactions and in measuring interparticle forces. /13/, /51/, /52/

Figure 21 shows a flowchart of a sophisticated soft particle MD simulation procedure for a vibro-fluidized dilute bed in which friction is taken into account. The forces acting on each particle are initially calculated. Newton's second law is then used to determine the resulting accelerations of each particle, which are then integrated in space and time to give the particles new velocities and positions. The process is repeated until the simulation ends.

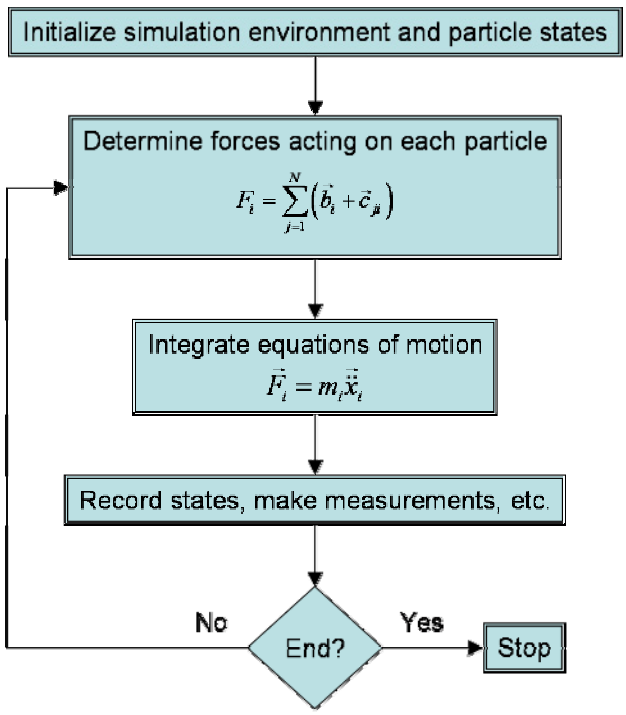

Figure 21 *Flow chart of a soft particle MD computer simulation.* /13/

Extracted from the above MD simulation model, the top snapshots in Figure 22 show the formation of a uniform heap and convection rolls in a deep particle bed that is subjected to vertical oscillations. The bottom snapshots show the steady state shape of the particle bed when it is subjected to both vertical and horizontal vibrations. An asymmetric heap located on one side of the container is similar to what we have

observed in our vibro-fluidized bed experiments and in experiments done by Evesque and Rajchenbach (1989), in addition to the model described by de Gennes. These simulation results clearly affirm that side lateral vibrations of the container are the cause of this peak and it is not due to previous suspicion of construction defects in the container, since even when it was rotated 180º, the peak continued to appear to the same side of the container. /13/

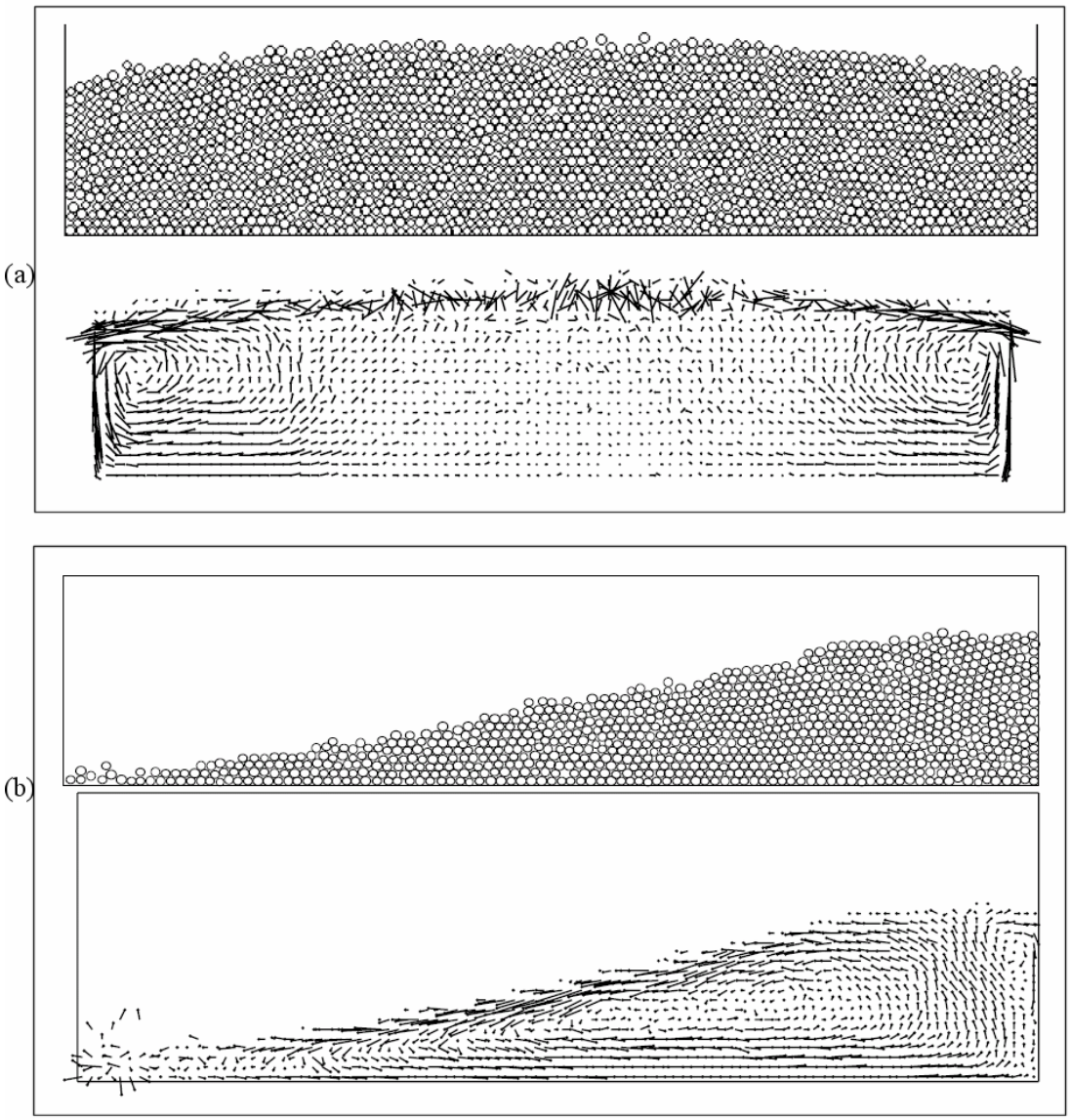

Figure 22 *Snapshot from MD simulations:* (a) *round heap formation in a particle bed and the presence of convection cells along the vertical walls in the same bed,* (b) *asymmetric heap formation when the particle bed is subjected to both vertical and horizontal vibrations, note the appearance of the peak on the right side of the container and the internal re-circulations*. /13/

3.6.4 Eulerian versus Lagrangian Description of Particle Motion

The previous section introduced the Lagrangian approach and MD simulations as useful tools for describing granular flows. These techniques model the system on a microscopic level, deriving individual particle trajectories using Newton's laws and computing the effects of each collision. Averaging over many collisions and particle trajectories gives the macroscopic behavior of the flow. The advantages of using the discrete model include:

- The ability to easily vary the physical properties of the system (e.g. size and density);
- The ability to obtain substantial insight into the fluid dynamic behavior of the particle flow with the associated local phenomena, and hence, by using adapting techniques, these models can be used for testing, validation and improving the constitutive equations for continuum models;
- Less prone to numerical diffusion errors;
- More stable for particle flows with large particle velocity gradients.

/35/, /47/, /53/

A complementary method for understanding granular flows is to model the macroscopic motion directly by a continuum field theory (Eulerian model) that describes the bulk motion of the flow in terms of the density, velocity and temperature fields. Unlike MD simulations, the continuum approach is not limited by particle number. Real industrial systems contain billions of particles, far outside the abilities of MD simulations. The computational demands (memory requirements and calculation time) to track a large number of particles and, consequently, solve the same number of constitutive equations for each particle, are the primary drawbacks of the Lagrangian approach. Therefore, MD simulations are useful for laboratory scale experiments, when the number of particles is not very large. Another drawback of the Lagrangian approach is that empirical data and correlations are required to describe the gas-solid interactions, unless the continuous phase is described using Direct Numerical Simulations (DNS). /35/, /54/

3.6.5 Continuum Theory of Granular Flows

The continuum theory of granular matter consists of partial differential equations similar to the Navier-Stokes equations for Newtonian fluids. In those equations, every grain is treated as a molecule of granular fluid that takes part in the macroscopic flow motion, as well as the random "thermal" motion, but they are modified from the Navier-Stokes equations to include dissipative effects arising from collisions between the grains.

Those equations emerge out of an averaging process over length and time scales that are much larger than typical microscopic scales and much smaller than macroscopic ones. This separation of scales may not occur in granular flows. Indeed, the issue of which are the relevant time and space scales is one of the most important questions to resolve. As schematically sketched in Figure 23, increasing the time and length scales of the models, which is necessary to increase the macroscopic validity and the robustness of the calculations, is related to a decreasing theoretical level with an

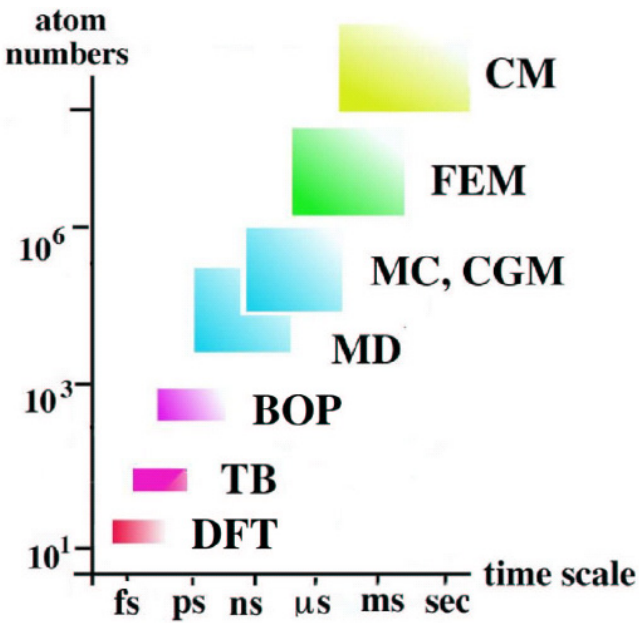

Figure 23 *Length and time scales employed in different structure modeling methods: DFT = Density Functional Theory, TB = Tight-Binding approximations, BOP = Bond Order Potentials, MD = empirical Molecular Dynamics, MC,CGM = Monte-Carlo and Conjugate-Gradient Methods, FEM = Finite Element Methods, CM = Continuum Mechanics*. /55/

increasing number of approximations, and thus to the loss of the respective physical properties in the description of the particle interactions.

For instance, in an ordinary fluid, an observation of pressure is typically carried out over a time spanning an enormous number of collisions so that the individual impacts are averaged out. The variations over space and time in granular flows should be small and occur over long distance, in order that the behavior of local collections of individual particles can be averaged and replaced with small fluid elements. Changes in time for the flow should occur for times long compared to the mean time between particle collisions so that particles moving between fluid elements do not affect the average values in a fluid element. Sufficient separation of scales may only be present for granular flows in the specific circumstances of low density and low dissipation.
/17/, /46/, /35/, /55/

3.6.6 Continuum Modeling of Granular Flows

The quantitative description of large-scale behavior of granular media requires reliable continuum models. Dense slow flows and rapid gas-like flows are useful idealizations for the development of continuum models. Owing to prompt energy dissipation, real systems often exhibit both flow types simultaneously in different spatial domains. One of the open questions is how to model the transition between the two flows accurately.
/10/, /17/

The Eulerian description, through rigorous definitions of averaging procedures, offers a formal methodology for developing numerical methods dealing with direct and indirect particle interaction and fluid turbulence. As a result, continuum models have been incorporated into commercial CFD codes, such as FLUENT and CFX.

Many gas-solid CFD models have been put forth by academic researchers, governments and commercial vendors. Although single-phase flow CFD tools are now widely and successfully applied, multiphase CFD is still at its development stage. The reason is the same as for the Lagrangian approach: lack of understanding and difficulty of describing the complex particle-particle and particle-fluid interactions that develop in turbulent flows. For example, to date there is still no agreement on even the

governing equations. In addition, proposed constitutive models for the solid-phase stresses and the interphase momentum transfer (fluid drag force) are partially empirical. However, the usefulness of CFD modeling for large-scale particle flow processes, like fluidized bed systems, based on the Eulerian and Lagrangian frameworks cannot be denied. These represent the only feasible approaches for performing parametric investigation and scale-up, optimization and design studies. /47/, /52/, /53/, /54/

Figure 24 illustrates qualitative comparison between simulation results, obtained by the Lagrangian and Eulerian approaches, and an experiment of bubble formation in a two-dimensional fluidized bed. /53/

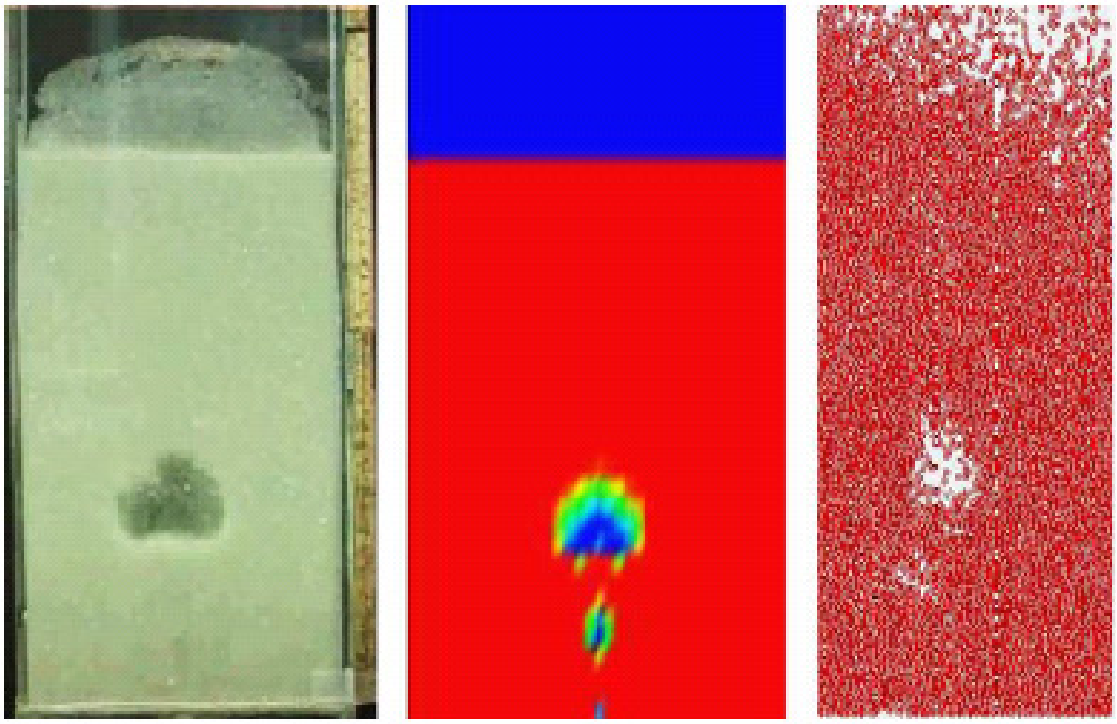

Figure 24 *Comparison of modeling approaches. The picture, which has been taken during experiment on two-dimensional fluidized bed at time t = 520 [ms] (left), is compared to the results obtained from both Eulerian (middle) and Lagrangian (right) numerical simulations.* /53/

3.7 CFD Eulerian Multiphase Model

Based on the Eulerian description of phases, a multiphase CFD model for gas-solid flow is presented. This model follows the Eulerian multiphase model provided with the commercial CFD software, FLUENT, which is the program used in this study for numerical simulations. In this model, there can be no compressible flow, inviscid flow, or chemical reactions. Fluid-fluid interactions described in the Eulerian multiphase model are not relevant for purposes of this work and hence they will not be discussed. /57/

FLUENT uses a multi-fluid granular model to describe the flow behavior of a fluid-solid mixture. The solid-phase stresses are derived by making an analogy between the random particle motion arising from particle-particle collisions and the thermal motion of molecules in a gas, taking into account the inelasticity of the granular phase. As in the case for a gas, the intensity of the particle velocity fluctuations determines the stresses, viscosity, and pressure of the solid phase. The kinetic energy associated with the particle velocity fluctuations is represented by a "pseudo-thermal" or granular temperature which is proportional to the mean square of the random motion of particles.

To change from a single-phase model, where a single set of conservation equations for momentum, continuity and energy is solved, to a multiphase model, additional sets of conservation equations must be introduced. In the process of introducing additional sets of conservation equations, the original set must also be modified. The modifications involve, among other things, the introduction of the volume fractions for the multiple phase, as well as mechanisms for the exchange of momentum, heat, and mass between the phases. /56/

3.7.1 Volume Fractions

The description of multiphase flow as interpenetrating continua incorporates the concept of phase volume fraction, α. Volume fractions represent the space occupied by each phase, and the laws of conservation of mass and momentum are satisfied by each phase individually. The derivation of the conservation equations can be done by

ensemble averaging (time averaged) the local instantaneous balance for each of the phases or by using the mixture theory approach. /3/, /56/

The volume of phase q, V_q, is defined as:

$$V_q = \int_V \alpha_q dV \tag{38}$$

With the constraint that the sum of all the solid phase volume fractions must be unity:

$$\sum_{q=1}^{n} \alpha_q = 1 \tag{39}$$

The effective density of phase q is:

$$\hat{\rho}_q = \alpha_q \rho_q \tag{40}$$

where ρ_q is the physical density of phase q.

3.7.2 Governing Conservation Equations

The laws of conservation of mass, momentum and granular temperature (energy conservation) are satisfied for each phase individually. The dependent variables, i.e. the volume fraction and the momentum, are solved for each phase. Note that in our model we have only one solid phase representing the glass beads in the vibro-fluidized bed and one gas phase that represents the interstitial air between the glass particles. /57/

The general form of the continuity equation for each phase q is:

$$\frac{\partial}{\partial t}\left(\alpha_q \rho_q\right) + \nabla \cdot \left(\alpha_q \rho_q \vec{\upsilon}_q\right) = \sum_{p=1}^{n}\left(\dot{m}_{pq} - \dot{m}_{qp}\right) + S_q \tag{41}$$

where $\vec{\upsilon}_q$ is the velocity of phase q and $\dot{m}_{pq}$ characterizes the mass transfer from the pth phase to q^{th} phase, and $\dot{m}_{qp}$ characterizes the mass transfer from phase q to phase p. By default the source term S_q is set to zero, but one can specify a constant or user-defined mass source. A similar term appears in the momentum and enthalpy equations.

The volume fraction of each phase is calculated from a continuity equation, as solved by FLUENT:

$$\frac{1}{\rho_{rq}}\left(\frac{\partial}{\partial t}\left(\alpha_q\rho_q\right)+\nabla\cdot\left(\alpha_q\rho_q\vec{\upsilon}_q\right)=\sum_{p=1}^{n}\left(\dot{m}_{pq}-\dot{m}_{qp}\right)\right) \tag{42}$$

where ρ_{rq} is the phase reference density, or the volume averaged density of the qth phase in the solution domain.

The solution of this equation for each secondary phase, along with the condition that the volume fractions sum to one, allows for the calculation of the primary-phase volume fraction. This treatment is common to granular flows.

The conservation of momentum for a phase q is:

$$\begin{aligned}&\frac{\partial}{\partial t}\left(\alpha_q\rho_q\vec{\upsilon}_q\right)+\nabla\cdot\left(\alpha_q\rho_q\vec{\upsilon}_q\vec{\upsilon}_q\right)=-\alpha_q\nabla p+\nabla\cdot\bar{\bar{\tau}}_q+\alpha_q\rho_q\vec{g}+\\&\sum_{p=1}^{n}\left(\vec{R}_{pq}+\dot{m}_{pq}\vec{\upsilon}_{pq}-\dot{m}_{qp}\vec{\upsilon}_{qp}\right)+\left(\vec{F}_q+\vec{F}_{\text{lift},q}+\vec{F}_{\text{vm},q}\right)\end{aligned} \tag{43}$$

where $\bar{\bar{\tau}}_q$ is the qth phase stress-strain tensor:

$$\bar{\bar{\tau}}_q=\alpha_q\mu_q\left(\nabla\vec{\upsilon}_q+\nabla\vec{\upsilon}_q^{\text{T}}\right)+\alpha_q\left(\lambda_q-\frac{2}{3}\mu_q\right)\nabla\cdot\vec{\upsilon}_q\bar{\bar{I}} \tag{44}$$

Here, μ_q and λ_q are the shear and bulk viscosity of phase q, $\bar{\bar{I}}$ is the unit tensor, $\vec{F}_q$ is an

external body force, $\vec{F}_{\text{lift},q}$ is a lift force, $\vec{F}_{\text{vm},q}$ is a virtual mass force, $\vec{R}_{pq}$ is an interaction force between phases and p is the pressure shared by all phases.

$\vec{\upsilon}_{pq}$ is the interphase velocity, defined as follows. If $\dot{m}_{pq} > 0$ (i.e., phase p mass is being transferred to phase q), $\vec{\upsilon}_{pq} = \vec{\upsilon}_p$; if $\dot{m}_{pq} < 0$ (i.e., phase q mass is being transferred to phase p), $\vec{\upsilon}_{pq} = \vec{\upsilon}_q$. Likewise, if $\dot{m}_{qp} > 0$ then $\vec{\upsilon}_{qp} = \vec{\upsilon}_q$, if $\dot{m}_{qp} < 0$ then $\vec{\upsilon}_{qp} = \vec{\upsilon}_p$. The interphase force $\vec{R}_{pq}$ depends on friction, pressure, cohesion, and other effects, and is subject to the conditions that $\vec{R}_{pq} = -\vec{R}_{qp}$ and $\vec{R}_{qq} = 0$. The term $\nabla \vec{\upsilon}_q^{\mathrm{T}}$ means:

$$\nabla \vec{\upsilon}_q^{\mathrm{T}} = \frac{\partial \upsilon_{q,i}}{\partial \upsilon_{q,j}} + \frac{\partial \upsilon_{q,j}}{\partial \upsilon_{q,i}} \tag{45}$$

where i and j represent the x and y directions respectively, and the superscript T denotes the velocity vector transposition.

FLUENT uses a simple interaction term of the following form:

$$\sum_{p=1}^{n} \vec{R}_{pq} = \sum_{p=1}^{n} K_{pq} \left(\vec{\upsilon}_p - \vec{\upsilon}_q \right) \tag{46}$$

where K_{pq} (= K_{qp}) is the interphase momentum exchange coefficient.

The lift forces, virtual mass forces, pressure gradients and viscous terms are usually neglected if the solids density is much larger than the fluid density, which is the fact in the present study since: $\rho_{glass} = 2500\ [\mathrm{kg/m^3}] \gg \rho_{air} = 1.225\ [\mathrm{kg/m^3}]$.The lift forces are also small compared to the drag force and hence they are neglected.

The general form of Equation (43) applies for fluid-fluid and fluid-solid systems. The conservation of momentum for fluid phases is similar to Equation (43), and for the sth

solid phase is:

$$\frac{\partial}{\partial t}\left(\alpha_s \rho_s \vec{\upsilon}_s\right) + \nabla \cdot \left(\alpha_s \rho_s \vec{\upsilon}_s \vec{\upsilon}_s\right) = -\alpha_s \nabla p - \nabla p_s + \nabla \cdot \bar{\bar{\tau}}_s + \alpha_s \rho_s \vec{g} + \sum_{l=1}^{N}\left(\vec{K}_{ls}\left(\vec{\upsilon}_l - \vec{\upsilon}_s\right) + \dot{m}_{ls}\vec{\upsilon}_{ls} - \dot{m}_{sl}\vec{\upsilon}_{sl}\right) + \left(\vec{F}_s + \vec{F}_{\text{lift},s} + \vec{F}_{\text{vm},s}\right) \tag{47}$$

where p_s is the sth solids pressure, $K_{ls} = K_{sl}$ is the momentum exchange coefficient between fluid or solid phase l and the solid phase s, N is the total number of phases and $\vec{F}_s$, $\vec{F}_{\text{lift},s}$ and $\vec{F}_{\text{vm},s}$ are as defined for Equation (43).

To describe the conservation of energy in Eulerian multiphase applications, a separate enthalpy equation can be written for each phase:

$$\frac{\partial}{\partial t}\left(\alpha_q \rho_q h_q\right) + \nabla \cdot \left(\alpha_q \rho_q \vec{u}_q h_q\right) = -\alpha_q \frac{\partial p_q}{\partial t} + \bar{\bar{\tau}}_q : \nabla \vec{u}_q - \nabla \cdot \vec{q}_q + S_q + \sum_{p=1}^{n}\left(\vec{Q}_{pq} + \dot{m}_{pq} h_{pq} - \dot{m}_{qp} h_{qp}\right) \tag{48}$$

where h_q is the specific enthalpy of the qth phase, $\vec{q}_q$ is the heat flux, S_q is a source term that includes sources of enthalpy (e.g., due to chemical reaction or radiation), $\vec{Q}_{pq}$ is the intensity of heat exchange between the pth and q^{th} phases, and h_{pq} is the interphase enthalpy. The heat exchange between phases must comply with the local balance conditions $\vec{Q}_{pq} = -\vec{Q}_{qp}$ and $\vec{Q}_{qq} = 0$. The energy equation is not used in our simulations because we don not have any combustion or heat transfer processes in the vibro-fluidized bed. In the future this equation is necessary to be taken into account when a scale-up of a vibro-fluidized bed system from simulation results is required.

3.7.3 Interphase Exchange Coefficient

Since air is the only fluid that is present in the experiments and simulations, the fluid-fluid exchange coefficients are dropped from the following discussion. The fluid-solid exchange coefficient K_{sl} can be written in the following general form:

$$K_{sl} = \frac{\alpha_s \rho_s f_D}{\tau_s} \tag{49}$$

where f_D is a coefficient that includes a drag function (C_D), which is defined according to the exchange-coefficient model being used, and τ_s is the particulate relaxation time, defined as:

$$\tau_s = \frac{\rho_s d_s^2}{18\mu_l} \tag{50}$$

where d_s is the diameter of particle of phase s. Here the subscript l designates the fluid phase, while s is the solid phase. Syamlal-O'Brien (SO) drag law was used in our CFD simulations and hence will be presented in this study. Drag laws, like Wen and Yu (WY), Gidaspow (G), Schiller-Naumann (SN), and others, also exist in FLUENT and their application depends on the details of the granular flow under investigation. Works by Boemer *et al*. have compared the differences between drag function models, however, published literature assessing the different multiphase C_D models in FLUENT with support from experimental measurements is not abundant. /24/, /68/

The Syamlal-O'Brien drag model accounts for increased volume loadings through the use of a drag coefficient which is based on terminal velocities for failing particles in settling or fluidized beds, with correlations that are a function of the volume fraction and relative Reynolds number:

$$\mathrm{Re}_s = \frac{\rho_l d_s \left|\vec{\upsilon}_s - \vec{\upsilon}_l\right|}{\mu_l} \tag{51}$$

The coefficient f_D in Equation (49) is defined in the SO drag model as:

$$f_D = \frac{C_D \,\mathrm{Re}_s\, \alpha_l}{24\upsilon_{r,s}^2} \tag{52}$$

where the drag function has a form derived by Dalla Valle:

$$C_D = \left(0.63 + \frac{4.8}{\sqrt{\mathrm{Re}_s / \upsilon_{r,s}}}\right)^2 \tag{53}$$

where $\upsilon_{r,s}$ is the terminal velocity correlation for the solid phase:

$$\upsilon_{r,s} = 0.5\left(A - 0.06\,\mathrm{Re}_s + \sqrt{\left(0.06\,\mathrm{Re}_s\right)^2 + 0.12\,\mathrm{Re}_s\left(2B - A\right) + A^2}\right) \tag{54}$$

$$\text{where, } \begin{cases} A = \alpha_l^{4.14} \\ B = 0.8\alpha_l^{1.28} & ,\alpha_l \le 0.85 \\ B = \alpha_l^{2.65} & ,\alpha_l > 0.85 \end{cases} \tag{55}$$

The fluid-solid exchange coefficient has the form:

$$K_{sl} = \frac{3}{4}\frac{\alpha_s \alpha_l \rho_l}{\upsilon_{r,s}^2 d_s} C_D\left(\frac{\mathrm{Re}_s}{\upsilon_{r,s}}\right)\left|\vec{\upsilon}_s - \vec{\upsilon}_l\right| \tag{56}$$

This model is appropriate when the solids shear stresses are defined according to Syamlal *et al*.

The solid-solid exchange coefficient K_{ls} is calculated from Syamlal-O'Brien Symmetric model and it has the following form:

$$K_{ls} = \frac{3\left(1 + e_{ls}\right)\left(d_l + d_s\right)^2\left(\frac{\pi}{2} + C_{\mathrm{fric},ls}\frac{\pi^2}{8}\right)}{2\pi\left(\rho_l d_l^3 + \rho_s d_s^3\right)} \alpha_s \rho_s \alpha_l \rho_l g_{0,ls}\left|\vec{\upsilon}_l - \vec{\upsilon}_s\right| \tag{57}$$

where

e_{ls} = the coefficient of restitution

$C_{\text{fric},ls}$ = the coefficient of friction between the lth and s^{th} solid-phase particles

d_l = the diameter of the particles of solid

$g_{0,ls}$ = the radial distribution coefficient

Note that in FLUENT the default value of the friction coefficient is set to zero, which implies smooth particles surface. This may not be the case in real-world granular flows.

3.7.4 Solids Pressure

The solids pressure p_s in Equation (47) is composed of a kinetic term and a second term due to particle collisions:

$$p_s = \alpha_s \rho_s \Theta_s + 2\rho_s \left(1 + e_{ss}\right) \alpha_{ss}^2 g_{0,ss} \Theta_s \tag{58}$$

where e_{ss} is the restitution coefficient for particle collisions. The granular temperature Θ_s is proportional to the kinetic energy of the fluctuating particle motion. The radial distribution function $g_{0,ss}$ is a correction factor that modifies the probability of collisions when the solid granular phase becomes dense. This function may also be considered as the non-dimensional distance between spheres. In the literature there is no unique formulation for this function and FLUENT has a number of options, but for one solids phase FLUENT uses:

$$g_0 = \left[1 - \left(\frac{\alpha_s}{\alpha_{s,\max}} \right)^{\frac{1}{3}} \right]^{-1} \tag{59}$$

This is an empirical formula, where $\alpha_{s,\max}$ is the maximum packing limit, which defines the solid's incompressible condition such that no further decrease in space is possible. A value of 0.63 is the default for $\alpha_{s,\max}$ in FLUENT, but one can modify it during simulation setup.

3.7.5 Solid Shear Stresses

The solids stress tensor contains the shear and bulk viscosities arising from particle momentum exchange due to translation and collision. A frictional component of viscosity can also be included to account for the viscous-plastic transition that occurs when particles of a solid phase reach the maximum solid volume fraction.

The collisional and kinetic parts, and the optional frictional part, are added to give the solids shear viscosity:

$$\mu_s = \mu_{s,\mathrm{col}} + \mu_{s,\mathrm{kin}} + \mu_{s,\mathrm{fric}} \tag{60}$$

The collisional part of the shear viscosity is modeled as:

$$\mu_{s,\mathrm{col}} = \frac{4}{5}\alpha_s \rho_s d_s g_{0,ss}\left(1+e_{ss}\right)\left(\frac{\Theta_s}{\pi}\right)^{1/2} \tag{61}$$

For the kinetic part of viscosity we must use the expression provided by Syamlal *et al*, because we have chosen to work with the SO drag model, see Equation (56) above. This expression is:

$$\mu_{s,\mathrm{kin}} = \frac{\alpha_s \rho_s d_s \sqrt{\Theta_s \pi}}{6\left(3-e_{ss}\right)}\left[1+\frac{2}{5}\left(1+e_{ss}\right)\left(3e_{ss}-1\right)\alpha_s g_{0,ss}\right] \tag{62}$$

The solids bulk viscosity accounts for the resistance of the granular particles to compression and expansion. The default value of bulk viscosity in FLUENT is zero, but it is also possible to write a User-Defined Function (UDF) to evaluate this quantity or select an expression provided by Lun *et al*. In the current study the bulk viscosity is included in a UDF that is written in C++ language.

The frictional viscosity is predominant in dense flow at low deformation rates and the secondary phase volume fraction is near the packing limit. However, since in the vibro-fluidized bed the flow is very rapid, the frictional viscosity is ignored and is not

taken into account in the simulations. The solids shear viscosity computed by FLUENT does not, by default, account for the friction between particles. /58/

3.7.6 Granular Temperature

The granular temperature for the sth solids phase is related to the kinetic energy of the random motion of the particles. It is found through an energy balance that accounts for energy generation via the solids stress tensor, the diffusion of energy, collisional dissipation of energy, and the exchange of energy among the phases present. Granular temperature of species varies spatially through the bed according to the degree of motion. The transport equation derived from kinetic theory takes the following form:

$$\frac{3}{2}\left[\frac{\partial}{\partial t}\left(\rho_s \alpha_s \Theta_s\right)+\nabla\cdot\left(\rho_s \alpha_s \vec{\upsilon}_s \Theta_s\right)\right]=\left(-p_s\overline{\overline{I}}+\overline{\overline{\tau}}_s\right):\nabla\vec{\upsilon}_s + \nabla\cdot\left(k_{\Theta s}\nabla\Theta_s\right)-\gamma_{\Theta s}+\phi_{ls} \tag{63}$$

where

$\left(-p_s\overline{\overline{I}}+\overline{\overline{\tau}}_s\right):\nabla\vec{\upsilon}_s$ = the generation of energy by the solid stress tensor

$k_{\Theta s}\nabla\Theta_s$ = the diffusion of energy ($k_{\Theta s}$ is the diffusion coefficient)

$\gamma_{\Theta s}$ = the collisional dissipation of energy

ϕ_{ls} = the energy exchange between the lth fluid or solid phase and the sth solid phase

3.7.7 Turbulence Models

In comparison to single-phase flows, the number of terms to be modeled in the momentum equations in multiphase flows is large, and this makes the modeling of turbulence in multiphase simulations extremely complex. FLUENT provides three methods for modeling turbulence in multiphase flows within the context of the k-ε models. In addition, FLUENT includes two turbulence options within the context of the Reynolds-Stress Models (RSM).

The k-ε turbulence model options are:

- Mixture turbulence model (default)
- Dispersed turbulence model
- Turbulence model for each phase

The RSM turbulence model options are:

- Mixture turbulence model (default)
- Dispersed turbulence model

The choice of model from either category depends on the importance of the secondary-phase turbulence in the desired application. The RSM dispersed turbulence model was selected during the simulations in FLUENT and accordingly will be discussed in the following section.

3.7.8 RSM Dispersed Turbulence Model

The dispersed turbulence model is used when the concentrations of the secondary phase are dilute and the primary phase turbulence is regarded as the dominant process. Consequently, the transport equations for turbulence quantities are only solved for the primary (continuous) phase, while the predictions of turbulence quantities for dispersed phases are obtained using the Tchen theory. The transport equation for the primary phase Reynolds stresses in the case of the dispersed model is:

$$\begin{aligned}\frac{\partial}{\partial t}\left(\bar{\alpha}\rho\tilde{R}_{ij}\right)+\frac{\partial}{\partial x_k}\left(\bar{\alpha}\rho\tilde{U}_k\tilde{R}_{ij}\right)=&-\bar{\alpha}\rho\left(\tilde{R}_{ik}\frac{\partial\tilde{U}_j}{\partial x_k}+\tilde{R}_{jk}\frac{\partial\tilde{U}_i}{\partial x_k}\right)\\&+\frac{\partial}{\partial x_k}\left[\bar{\alpha}\mu\frac{\partial}{\partial x_k}\left(\tilde{R}_{ij}\right)\right]-\frac{\partial}{\partial x_k}\left[\bar{\alpha}\rho\overline{u_i'u_j'u_k'}\right]\\&+\overline{\bar{\alpha}\,p\left(\frac{\partial u_i'}{\partial x_j}+\frac{\partial u_j'}{\partial x_i}\right)}-\bar{\alpha}\rho\tilde{\varepsilon}_{ij}+\Pi_{R,ij}\end{aligned}\tag{64}$$

Here, the tilde (e.g., $\tilde{R}$) denotes phase-averaged variables while the over-bar reflects time-averaged values, $\tilde{R}_{ij}$ is Reynolds stresses, U is the phase-weighted velocity, u_i' is

the fluctuating velocity component (i = 1, 2, 3), and $\tilde{\varepsilon}$ is the turbulent kinetic energy dissipation rate. The last term of Equation (64), $\Pi_{R,ij}$, takes into account the interaction between the continuous and the dispersed phase turbulences. The variables in Equation (64) are per continuous phase *c* and the subscript is omitted for clarity.

3.8 CFD Simulations and Results

All of the computational modeling and testing in this study were performed in the Laboratory of CFD at Lappeenranta University of Technology. The transient hydrodynamic behavior of a two-dimensional gas-solid vibro-fluidized bed is investigated by using non-steady state Eulerian multiphase model available in the commercial software, FLUENT version 6.2.16 (by Fluent, Inc., USA).

It is good to remember at this point that granular flows are in reality three-dimensional, and 2D simulations only correspond to an approximation of the salient features of the granular flow field. Two dimensional problems require less computational time than the three-dimensional ones, and this is the main reason for using them.

The geometry of the vibrated vessel was first constructed and meshed in the grid generator preprocessor GAMBIT 2.2.30, by Fluent, Inc. The dimensions of the vessel are identical to the plastic cup geometry that was utilized in the experiments. However, by taking full advantage of the axisymmetric nature of the granular flow inside the cell, only half of the vessel's profile required modeling in GAMBIT. This has a further positive impact on minimizing the computational time. The mesh consists of 2652 nodes and 5058 2D triangular elements (Tri-Pave meshing scheme in GAMNIT). The Tri-Pave elements are more flexible for dynamic meshing in FLUENT than the quadrilateral elements, see Figure 25. After the grid was created, it was exported directly to FLUENT, where it is loaded and the boundary, model, and physical property parameters were assigned.

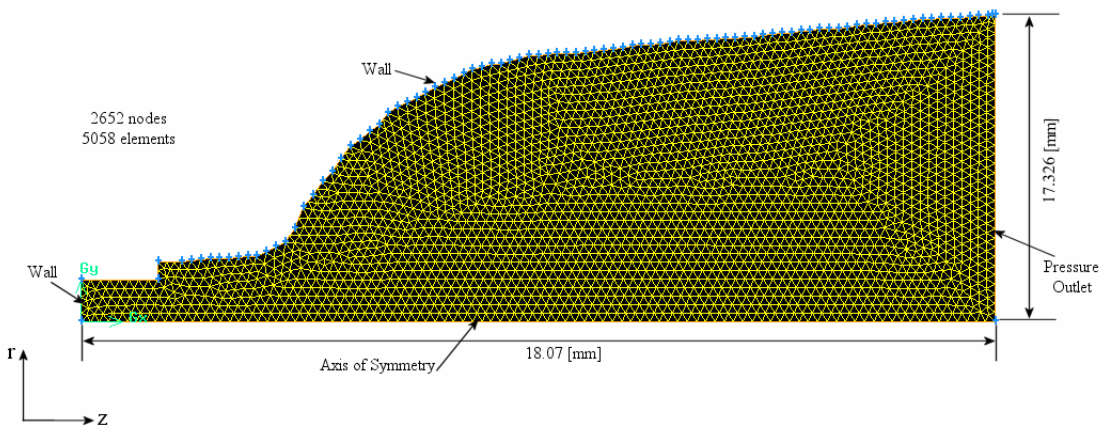

Figure 25 *Axisymmetric vessel model: layout; dimensions and boundary conditions.*

FLUENT uses a finite volume-based algorithm to transform the governing physical equations to algebraic equations that can be solved numerically. In such an approach, the computational domain is subdivided into individual, discrete control volumes, or cells. The governing equations about each cell are then integrated, yielding discrete equations that conserve each quantity on a control-volume basis. /59/

For the Eulerian multiphase calculations, FLUENT uses the Phase Coupled SIMPLE (PC-SIMPLE) algorithm for the pressure-velocity coupling. PC-SIMPLE is an extension of the SIMPLE algorithm to multiphase flows. The solved velocities are coupled by phases, but in a segregated fashion. The coupled solver uses the block algebraic multigrid scheme to simultaneously solve a vector equation formed by the velocity components of all phases. Then, a pressure correction equation is built based on total volume continuity rather than mass continuity. Pressure and velocities are then corrected so as to satisfy the continuity constraint. /56/

Additionally, the grid is divided into a lower zone and an upper zone for specifying initial conditions. At time zero, the lower zone, 0 [mm] < z < 68.9 [mm], is filled with solids at an appropriate volume fraction, while the upper zone contains no solids. Mesh refinement in the lower region is employed to achieve a better resolution of the flow field, and the region adaptation options in FLUENT are used for this purpose. The main simulation parameters and boundary conditions used in FLUENT are summarized in Table 9. The user-defined function contains information about oscillation amplitude and frequency, and also about the granular shear viscosity.

Table 9 *The main solution parameters used in FLUENT simulations.*

Models					
Solver					
	Solver:		Segregated		
	Space:		Axisymmetric		
	Time:		Unsteady		
	Unsteady Formulation:		1st- Order Implicit		
Multiphase	Multiphase Model:		Eulerian		
	Number of Phases:		2		
Viscous	Model:		Reynolds Stress (5 eqn)		
	Reynolds-Stress Options:		Wall Reflection Effects		
	Near-Wall Treatment		Standard Wall Functions		
	RSM Multiphase Model		Dispersed		
Materials		Density [kg/m^3] (Constant)	Viscosity [kg/m·s] (Constant)		
	Air	1.225	1.7894×10^{-5}		
	Sand	2500	1		
Phases	Primary Phase	Air			
	Secondary Phase	Sand			
		Phase Interaction	Drag Coefficient	Collisions	
			Sand–Air Drag Coefficient	Sand-Sand Restitution Coefficient	
			Syamlal-O'brien	0.9 (Constant)	
		Granular Temperature Model	PDE (Partial Differential Equation)		
		Granular Viscosity	UDF		
		Granular Bulk Viscosity	UDF		
		Frictional Viscosity	None		
		Granular Conductivity	Syamlal-O'brien		
		Solids Pressure	Lun *et al*		
		Radial Distribution	Lun *et al*		
		Elasticity Modulus	Derived		
		Packing Limit	0.63		
Operating Conditions	Operating Pressure [kPa]	Gravity [m/s^2]	Variable Density Parameters (Operating Density) [kg/ m^3]		
	101.325	-9.81	1.225		
Boundary Conditions	Zone Name	Type	Phase		
	axis_of_ symmetry	axis			
	default-interior	interior			
	fluid	fluid			
	pressure_outlet	pressure-outlet	Mixture	Gauge Press. [Pa] (Normal to Boundary)	0
			Air	Backflow Turbulent Intensity [%]	10
				Backflow Hydraulic Diameter [m]	0.0654
			Sand	Backflow Granular Temperature [m^2/s^2]	0.0001
				Backflow Volume Fraction	0
	wall_boundary	wall	Mixture	Wall Roughness (roughness constant)	0.5
			Air	Shear Condition	No slip
			Sand	Granular conditions	Johnson Jackson
				Restitution coefficient	0.2
Solve	Solution Controls	Discretization			
		Momentum	First Order Upwind		
		Volume Fraction	First Order Upwind		
		Granular Temperature	First Order Upwind		
		Turbulence Kinetic Energy	First Order Upwind		
		Turbulence Dissipation Rate	First Order Upwind		
		Reynolds Stresses	First Order Upwind		
		Pressure-Velocity Coupling	Phase Coupled SIMPLE		
	Monitors	Residual	Continuity Convergence Criterion:		
			0.001		

Several workstations in the laboratory of CFD equipped with FLUENT were used to run various simulations. Our intention is to examine the effect of changing key factors like particle diameter, frequency and amplitude of vibration, and the inclusion of horizontal vibration, in order to resemble experimental results. Unfortunately, because of time and software license limitations, not all of these cases could be simulated.

Table 10 highlights three representative cases of the simulation. The results of these cases are shown in Figures 26, 27, and 28 respectively. The figures outline the development of the granular flow by tracking the volume fraction profile of sand with time. The blue area in the figures is the air volume fraction and the red area is the sand volume fraction. A thin vertical black line in the middle shows the axis of symmetry.

Table 10 *Simulation cases.*

	Case 1	**Case 2**	**Case 3**
Mean particle diameter, $\overline{d}$ [mm]	0.375	0.375	0.1
Frequency of vibration, f [Hz]	36	45	36
Vertical vibration amplitude, A [μm]	1.5	1.5	1.5
Horizontal vibration amplitude, B [μm]	0.5	0.5	0.5

The first general impression from the simulations is that the flow pattern displays an ideal uniform distribution, without a localized heap formation as was observed in the experiments. This may be due to the fact that the container in the simulations is subjected to homogeneous horizontal and vertical vibrations at constant amplitudes: However, this situation is hard to achieve in experiments, particularly at the resonant frequency when vigorous shaking of the container causes much distortion to the vibration signal. In future, there might be need to apply different vibration signals at different cross sections of the container, for example, low-amplitude horizontal vibration near the bottom of the container and higher amplitude at the top, which requires, then, performing experiments to determine the extent of such amplitudes.

Nevertheless, the current simulations give us impending perceptions from the bed interior that are not possible to be got from experiments.

It is clear from comparison of Figures 26 and 27 with Figure 28 that for relatively smaller particle size, the fluidization is more stable and smooth at the surface of the bed. On the other hand, surface heaps close to the side of the container appear for larger particle size. Notice from Figure 28 the frequent and clear formation of an air bubble at the bottom of the bed; while this behavior is quite weak for the larger particle size, yet, it is still visible.

In essence, during the experiment the bubble formation might have appeared but it cannot be affirmed because of the fast bed expansion, opacity of the bed and small bubble size. High-speed camera and modified experimental setup, especially larger container size, would be necessary if bubble formation is to be tracked. Considering the same particle size at different frequencies, it can be seen from Figures 26 and 27 that there is no significant difference in the behavior of the granular flow when changing from the critical frequency of 36 [Hz] to 45 [Hz].

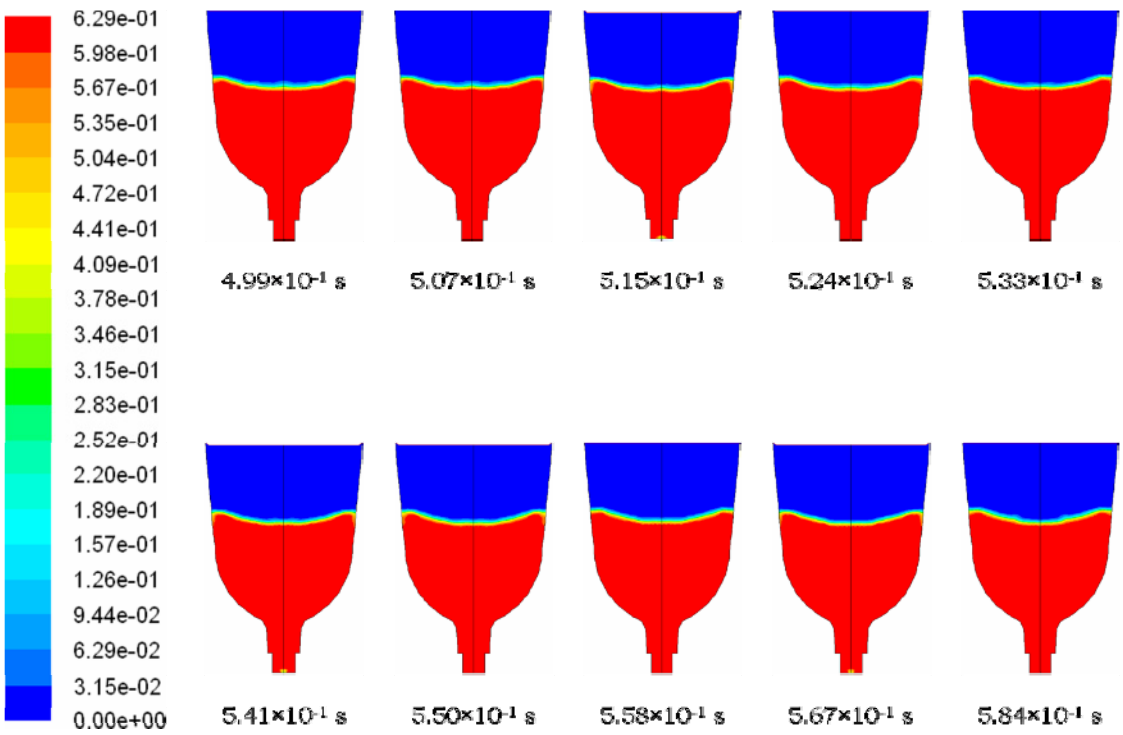

Figure 26 *Contours of sand volume fraction for case 1 in Table10.*

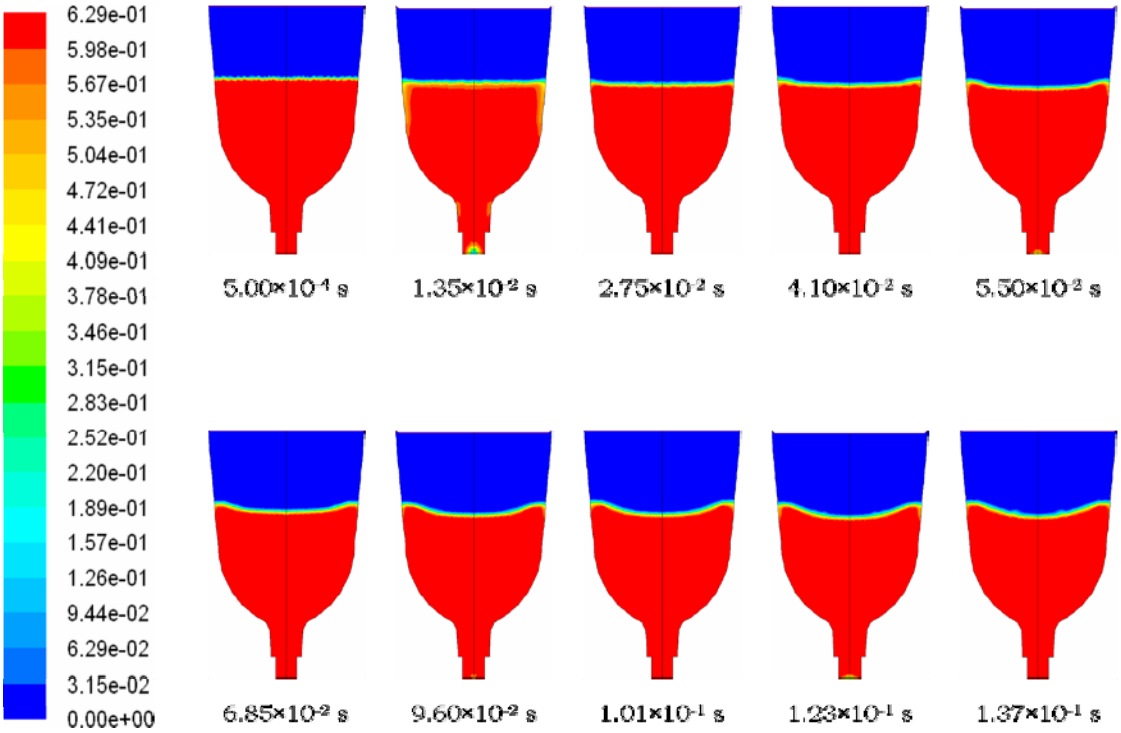

Figure 27 *Contours of sand volume fraction for case 2 in Table 10.*

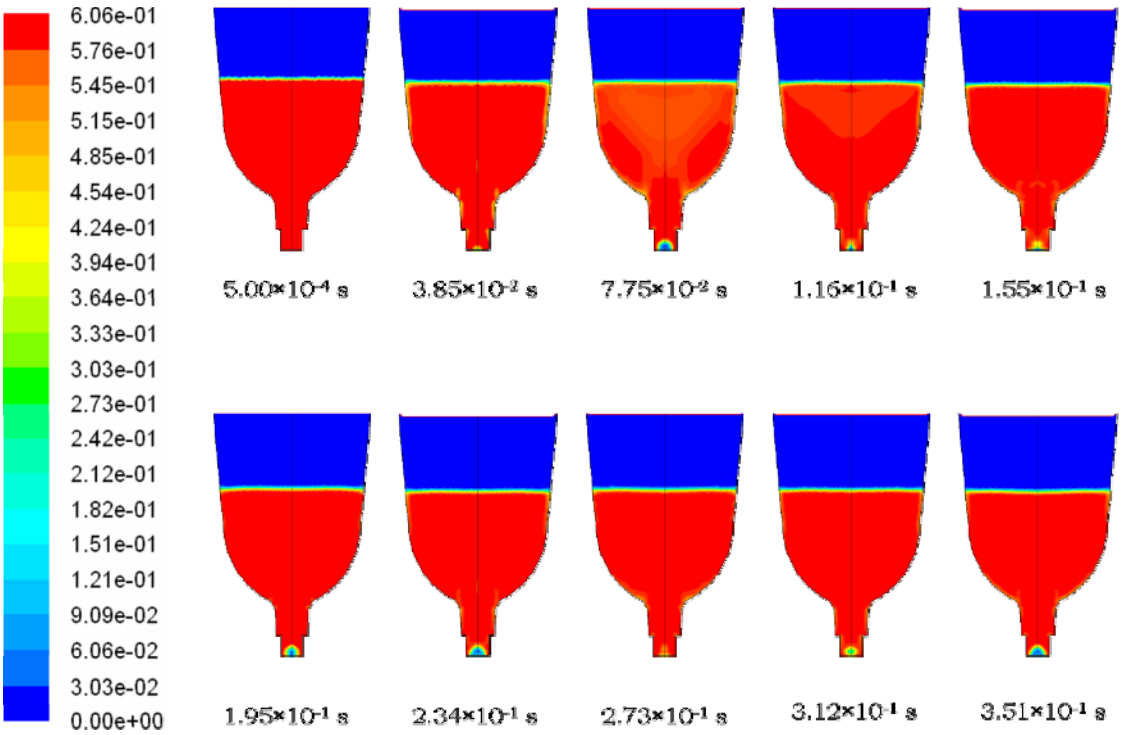

Figure 28 *Contours of sand volume fraction for case 3 in Table 10.*

The velocity profile for sand motion in the bed is illustrated in Figure 29 (subfigures: a to e). The sand flows up along the boundary walls of the container and at some point it changes direction and moves down stream close to the center of the container. The layer of downward moving sand is much thicker than the upward flow, which is an evidence of the strong drag and gravity effects in this region. Convection rolls that take the shape of the container can be easily distinguished. This flow pattern is common in all simulations with combined lateral and vertical vibrations, but it was not detected in simulations where only vertical vibration is applied to the container. As a conclusion, we suggest that horizontal vibration plays a key role in establishing the convection phenomena that appears in the present simulations. However, it must be stressed that this is not a generalization about the phenomena, i.e., convection can still occur in granular beds subjected to vertical vibration only and it is just in this special case for this particular container shape that horizontal vibration induces convection.

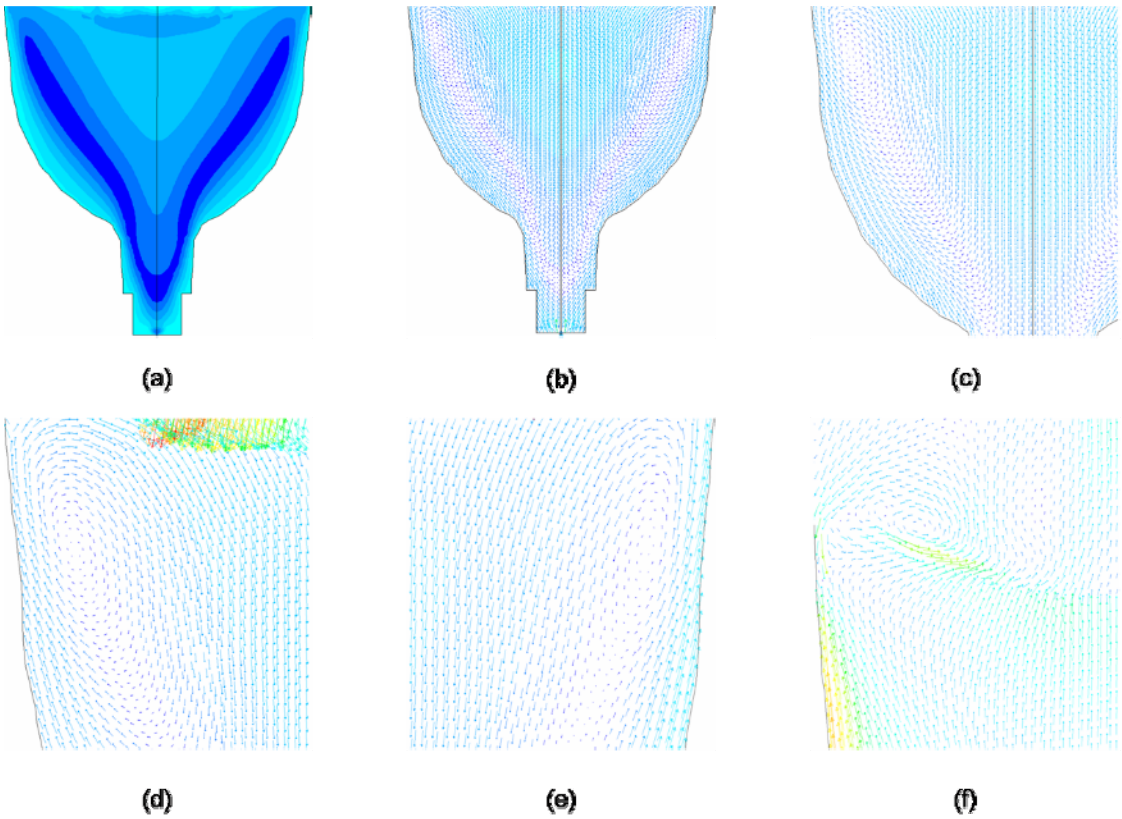

Figure 29 (a) *Sand velocity magnitude contours;* (b) *and* (c) *sand velocity arrows colored by velocity magnitude, scaled 3 times*; (d) *and* (e) *convection rolls at the left and right sides of the container, velocity arrows scaled 3 times;* (f) *air velocity arrows, scaled 3 times*.

Notice also in the same figure the development of velocity gradient fields (clearly in figure 29 a). The dark blue area in this figure shows particles moving at a very small velocity compared with other regions in the flow field. These velocity gradients provoke shear stresses inside the flow

A snapshoot from the air velocity arrows is shown in Figure 29 f. Here, the air moves upward in a direction defined by the interstitial spaces between the particles. The movement of the sand near the surface induces the appearance of air whirls. In addition, this upward air flow is expected to resist the particle down-flow near the center, where drag effects are highest. The air drag force opposing the particle flow in this region is weaker than the gravity force in that region, and, thus, particles continue to move downwards. The situation is more complicated near the wall boundaries where lateral vibration with a high vibration amplitude and frictional contact between particles and container coexist. The relative motion between the air and particles and their velocities determines the shape of the flow. But, the convection rolls that appear in this region are mainly due to the friction resistance between the particles and the container's wall.

The upward direction of air flow seems to be unaffected by the cyclic movement of the container when a steady state flow is achieved. Another thing that can also be dictated from the present simulations is that the air pressure inside the container is obviously higher than the surrounding atmospheric pressure.

By referring to Table 8 and Table 10, it is observed that the vertical vibration amplitudes in the simulation are much lower than the average amplitude that was found from experiments. A simulation run has diverged when we tried to input a vertical vibration amplitude similar to that found for the 0.375 [mm] particle diameter, namely A = 0.42 [mm]. The reason is perhaps related to large deformation of the dynamic mesh in FLUENT that causes continuity divergence problems.

4. MODAL ANALYSIS OF VIBRO-FLUIDIZED BEDS

4.1 Background about Modal Analysis

Modal analysis of vibration is used as a simple and efficient means for characterizing resonant frequencies, which occur when one or more of the resonances or natural modes of vibration of a structure are excited. Running mode analysis to investigate the vibrational behavior of a mechanical system can be simulated by a multiple degree of freedom model. This model is mathematically described with coupled linear differential equations of second degree, with eigenvalues as solutions that determine the mode shapes. Eigenfrequencies and damping values are parameters of the model.

Modal analysis transforms the vibration problem from a difficult-to-solve multiple degree of freedom problem, given by a coupled set of equations of motion in physical coordinates, into a set of decoupled single degree of freedom problem that we know how to solve in modal coordinates. The usefulness of this approach is that the computations of mode shapes matrix representing the solution eigenvalues can be easily automated in a computer code. /60/, /61/, /62/.

4.2 Model Construction in ANSYS Workbench

In this study we performed modal analysis of the sand−container structure by using a software called ANSYS Workbench™ version 10 (by ANSYS, Inc., USA) see Figure 30. The program is used to display an animation of the different mode shapes of the system under conditions of variable friction factors between the sand and the container. Sand is modeled as a discrete elastic mass, whose shape conforms to the shape of the container inner side with very small gap separating the sand from the container. The bulk density of sand is set to 1500 [kg/m^3] and its depth in the container is chosen to be similar to that of the static bed height in CFD simulations and experiments for the average particle diameter: $\overline{d}$ = 0.375 [mm], refer to Tables 8 and 10, and Figure 31.

The material properties of the container and support are chosen to be analogous to the polyethylene properties available from the sample material library in ANSYS Workbench, and the bonded contact type is selected for the cup−support contact

region. The choice of this plastic material instead of the more realistic polystyrene cup and polypropylene base should not have a significant influence on the final results, although it is not predictable.

The “All Tetrahedrons” meshing method for sand, container and its support is defined with a 3 [mm] element size. The environmental loading conditions that act on the system are the standard earth gravity g and a fixed support at the bottom of the container directed in the positive y-axis. The effect of atmospheric pressure is assumed to be negligible.

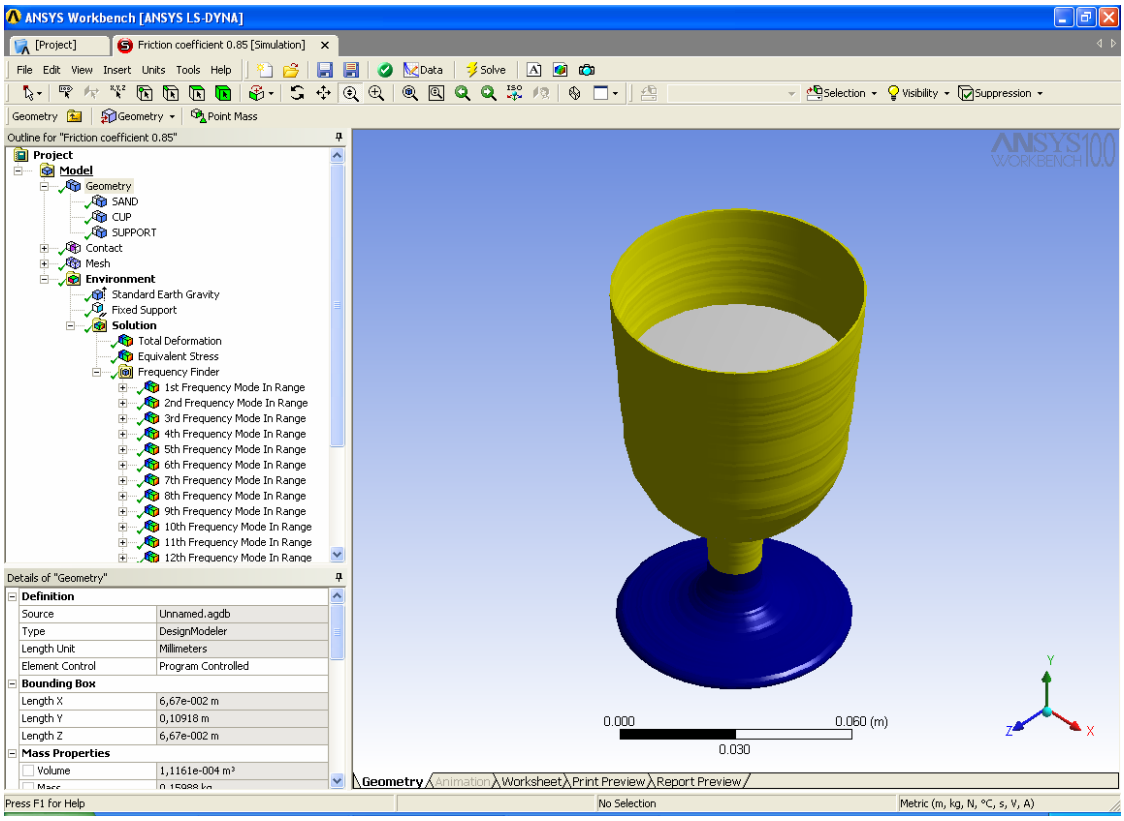

Figure 30 *ANSYS Workbench Simulation Module: user interface.*

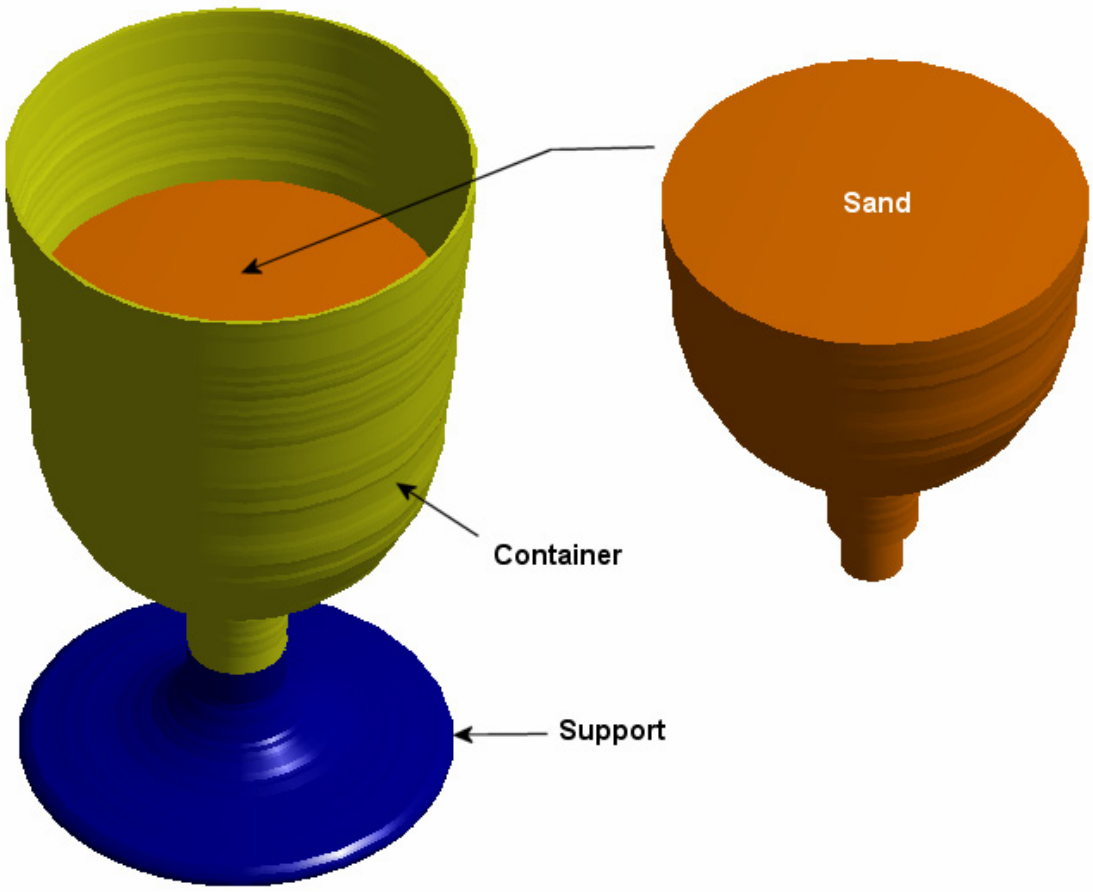

Figure 31 The *profile of sand inside the container where it is modeled as a discrete elastic unit.*

4.3 Results of Modal Simulations

From the simulation solution control menu The Frequency Finder tool is used to animate the deformed shape of the container−sand assembly. Here, the primary goals are to investigate the effect of friction between the sand and the container, besides prediction of a value for the friction factor.

In the series of cross-sectional contour plots shown in Figure 32, the first 10 frequency modes with their associated natural frequencies are shown for 0.50 friction factor. Appendix 2 covers the mode shapes of different friction factors that range from a very small value (almost frictionless) to a high-friction coefficient (rough) between the inner container surface and sand. In these figures the contours represent the relative displacement of the system as it vibrates, but they do not represent actual displacements. Some of the mode shape contours are common for many of the friction

coefficients, like the first and second modes. The general conclusion is that the natural frequency increases with increasing friction coefficient and frequency mode. This can be depicted from Figure 33. /63/

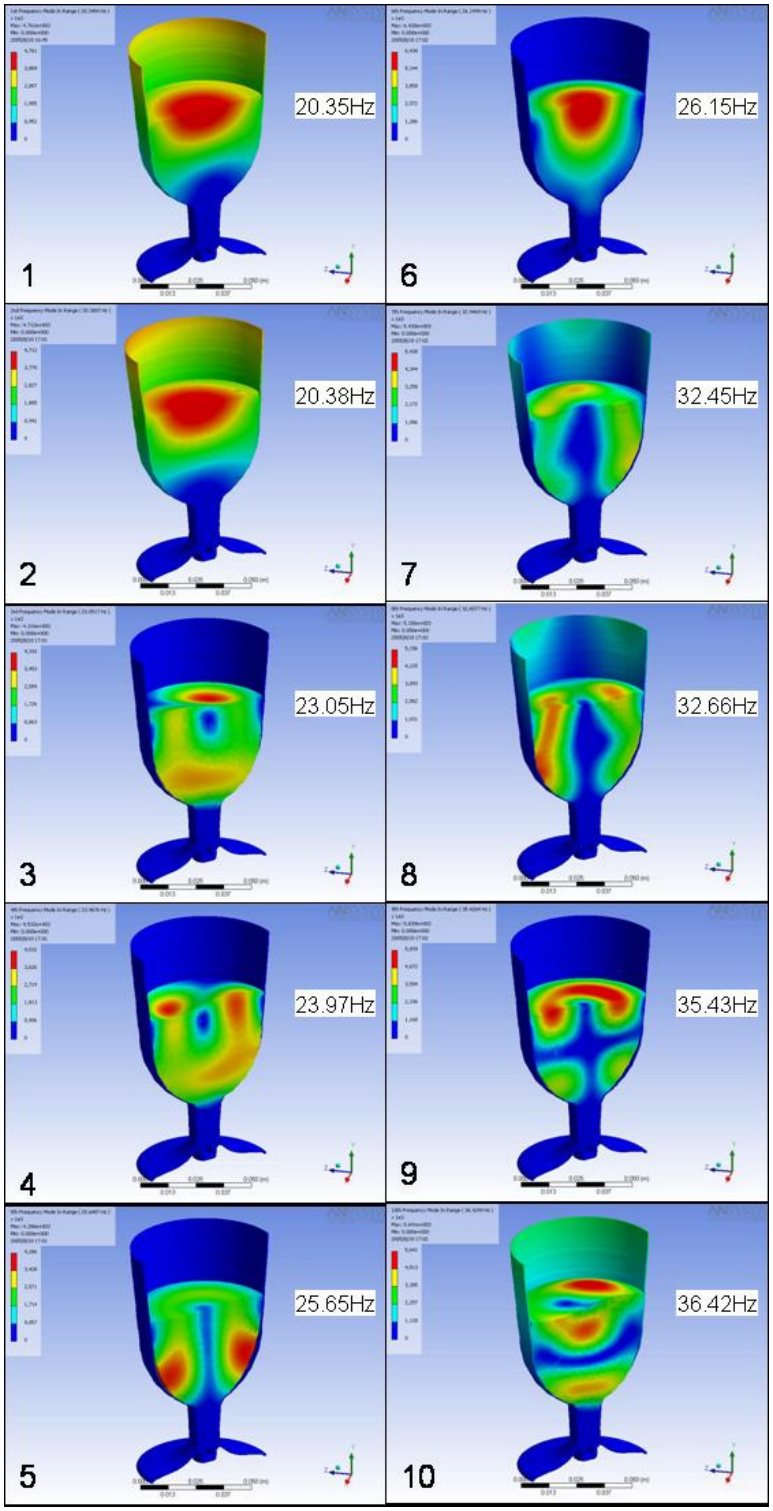

Figure 32 *Contour plots of mode shapes for 0.50 friction factor.*

Resonance occurs when the natural frequency of a system under free vibration without damping coincides with that of forced vibration. This definition can help us in estimating the value of the friction coefficient between sand and container from among the above mentioned range of friction coefficients.

The resonance frequency at which fluidization happens was found experimentally to be 35.75 [Hz] (from Table 8). In Figure 33 the nearest natural frequency which corresponds to this resonant frequency is the 9th mode at 35.43 [Hz], belonging to the 0.50 friction factor. The next friction coefficient (0.60) at the same frequency mode has a natural frequency of 36.75 [Hz], hence, by linear interpolation we estimate that the value of friction coefficient between sand and the container's inner medium is approximately 0.52.

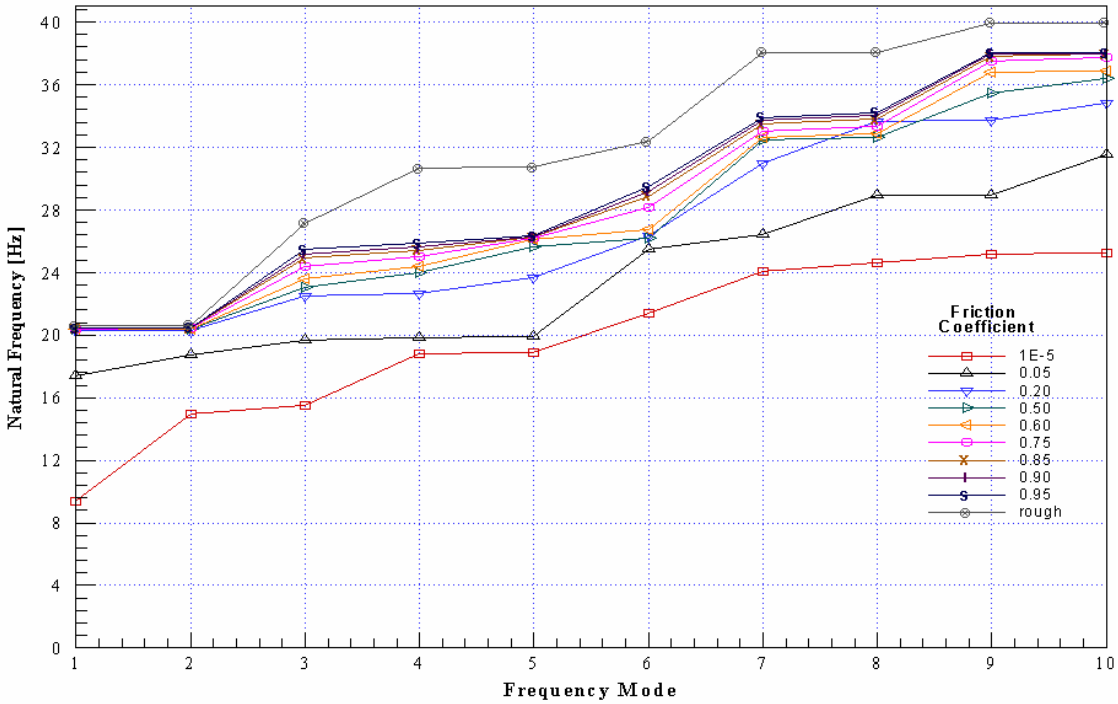

Figure 33 A *plot of the frequency mode versus the natural frequency of the sand−container system, for various friction coefficients.*

5. CONCLUSIONS AND FUTURE WORK

This thesis was devoted to study the vertical vibration of granular materials with special attention to collision, friction, drag force and modeling of granular flows. The main body of the manuscript has been broadly structured into three interlinked paths that integrate each other:

- The literature part was scattered throughout the text to provide a background about the vibration of granular media; and to theoretically and mathematically back up the experiments and simulations.
- The experiments are designed to measure the coefficient of restitution for inelastic collision between glass balls and to explore the effect of changing some key variables on the behavior of vibro-fluidized granular bed.
- Numerical simulations further emphasized the experimental observations and their results enabled us to examine features that are not easy to detect or measure by experiments.

In the subsequent sections a summary of the main points unveiled in this study are presented and it is followed by a discussion about future work in this field.

5.1 Summary of the Thesis Core Points

- The interest in vibration of granular materials emerges from intention to enhance the granular flow properties in different industries.
- Granular materials are unique in that they can behave like solids, fluids, or gases.
- Granular materials studying and research is an interdisciplinary field that requires a comprehensive understanding in many areas like contact mechanics, materials science, fluid mechanics, etc.
- The predominant difference between the continuum description of granular flows and that of conventional fluids is the inelastic energy dissipation in the collision between granular particles due to friction, viscoelasticity, and plastic deformation.
- Restitution coefficient is a very important parameter which will enter in any model that takes into account the inelastic nature of granular materials collisions.

- The restitution coefficient can be measured experimentally from the geometrical assembly of Newton's cradle device and conservation of momentum principle.
- Measurements of distance and velocity by using Vernier ultrasonic motion detector have some limitations, and it is not suitable for collision experiments.
- There is a nonlinear dependence of the restitution coefficient on impact velocity, and it generally decreases with increasing impact velocity.
- Experiments of collision between glass balls indicate that the particle size has a negligible effect on the value of restitution coefficient.
- FEA analysis shows that the Elastic material model of glass is the closest model in agreement with experimental results of restitution coefficient, from the percentage of error stand point. The rule that the viscous damping coefficient plays in modifying the results for Maxwell, Kelvin and Viscoelastic is not accurately clear and, accordingly, further research is necessary in this topic.
- The vibro-fluidized bed experiments encompass many variables like particle's size; shape; distribution and material, container's geometry and material, number of particles, vibration frequency and amplitude, etc. Those variables have many combinations and the effect of only few of them has been studied in this work.
- The transition from the static solid state to the uniform dynamic state in the vibro-fluidized system for medium and deep depths occurs at the approximate value of 2 g of the dimensionless acceleration.
- Lateral vibration has a significant contribution to the formation of single heap on one side of the container in the vibro-fluidized bed experiments. The heap is associated with a steady convection pattern. These observations are consistent with what other researchers have found, both experimentally and by simulation.
- The dimensionless acceleration decreases with increasing particle diameter, while the critical frequency increases with increasing bed depth.
- Lagrangian models describe the granular flows on a microscopic level and they are useful for small scale particle flows.
- The Eulerian approach describes the bulk motion of the flow and it is useful for modeling large scale systems.
- Recognizing the axisymmetric nature of granular flows inside the vibro-fluidized bed facilitates saving computational and modeling times.

- In the two-dimensional CFD simulations, surface heaps appear on both sides of the container for relatively large particle sizes, while that was not the case for small-sized particles.
- The CFD simulations revealed air bubble formation at the bottom of the bed, a behavior that could not be affirmed in the current vibro-fluidized bed experiments. The bubble formation appears clearly for very small particle size, where the interstitial air has a prominent effect.
- Convection rolls mainly stem from the frictional resistance that particles experience at the vessel's wall boundaries.
- Drag and gravity effects are highest in the center of the vibro-fluidized bed.
- Shear stress is induced in the granular flow by the development of particle velocity gradients in the flow field.
- ANSYS Workbench modal simulations demonstrated that the natural frequency of the sand-container system is directly proportional to the friction coefficient. Comparison between the simulations and experimental results make it possible to estimate a value for the friction coefficient. This value is found to be 0.52.

5.2 Future Research Work

Certainly enough, after this elaboration, the open question that might manifest itself is what will happen to a particle placed on top of a vibro-fluidized bed? The particle can be a solid biomass fuel, e.g. plastic or wood, moving in a conventional fluidized bed. This question has been at early stages in this work one of the main objectives, before it was realized that a foundation has to be created in order to address the many topics that evolved.

In future, there will be a demand for making additional vibro-fluidized bed experiments that contain a particle, say a sphere, whose diameter is large in comparison with the granular particle's diameter. Different particle shapes, sizes and materials need to be investigated as well. A relevant matter that has then to be tackled is size segregation. The container dimensions, geometry and material are among those variables that can influence the final result and their inclusion into experiments is vital if the intruder response to vertical vibration is to be closely studied. In this respect, work by other researchers can be extremely useful to avoid duplicated efforts.

There is no doubt that any successful conduction of experimental research requires sophisticated equipments. The use of a mechanical shaker, a high-speed camera, an oscilloscope, reliable motion detectors and accelerometer sensors will definitely improve the credibility of the results.

With regard to future simulations, the focus has to shift to Large Eddy Simulations (LES) because of their promising capabilities in modeling of turbulence in transient flows and bridging the differences between the k-ε turbulence modeling and direct numerical simulations (DNS). Three-dimensional simulations have to be put into consideration in the future with the appropriate adaptive mesh refinement. The simulations should confront the divergence that occurred in the present simulations at high vibration amplitudes, comparable to experimental findings. Needless to say, these simulations must deal with similar particle and container shapes and dimensions as in experiments

Any planned research that will extend the results obtained in this work to fluidized bed combustion has; naturally, to incorporate the effects due to temperature and heat transfer in the future experiments and models. Ultimately, if the method of vertical vibration is applied successfully to new designs of industrial fluidized bed reactors, it will be is projected to increase the heat and mass transfer rates in the bed and reduce the power consumption through efficient energy conversion and by improving the fluidization quality. For example, an adequate understanding of the heaping and convection patterns may result in bed designs that exploit these phenomena to absorb and ingest solid fuel particles in the downward granular flow between the two convection rolls at very high efficiencies. Further, any decrease in the friction between the bed material and its confining walls will have a positive consequence on decreasing the wear down of walls by friction.

In conclusion, the framework of this thesis is ideally suitable as a reference for prospective advanced research in the same area. A Ph.D. study would be, perhaps, the correct level for full scientific assessment of the subject. The above illustrated results and suggestions can the settling point.

REFERENCES

/1/ Kunii, D. 1991. Fluidization Engineering, Second Edition, Butterworth-Heinemann, Boston, ISBN 0-409-90233-0.

/2/ Aranson, I.S. 2003. Periodic and Disordered Structures in a Modulated Gas-Driven Granular Layer, Physical Review Letters, Vol. 90, 134301.

/3/ Schulz, P. 2004. Instability and the Formation of Bubbles and the Plugs in Fluidized Beds, Opuscula Mathematica 24/1, 133.

/4/ Silva-Moris, V.A. and Rocha, S.C.S. 2003. Development of A Vibrofluidized Bed and Fluid-Dynamic Study with Dry and Wet Adipic Acid, Brazilian Journal of Chemical Engineering, Vol. 20, No. 04, 423.

/5/ Schiffer, P. 2001. The Drag Force in Granular Media, Powders and Grains 2001: Proceedings of Fourth International Conference on Micromechanics of Granular Media, ed. Y. Kishino, (A. A. Balkema, Lisse, 2001).

/6/ Pak, H. K. and Behringer, P. R. 1994. Bubbling in Vertically Vibrated Granular Materials, Nature, Vol 371, 15 September 1994, 231– 233.

/7/ Rycroft, Chris H. 2004 Granular flow and random walk methods. Department of Mathematics / Massachusetts Institute of Technology, Massachusetts, USA. [e-document retrieved on 13.9.2005 from: http://www-math.mit.edu/18.366/proj/03/rycroft_granular.pdf].

/8/ Schiffer, P. 1999. Beach Physics: Studies Of Wetting And Drag Force In Granular Media. Physics Department / University of Notre Dame, Indiana, USA. [e-document retrieved on 13.9.2005 from: http://www.nd.edu/~ame/announcements/Schiffer.html].

/9/ Sauer, S. 1997. Modeling of Gas and Particle Mixing in Fluidized Bed Combustion of Biomass. Institute of Energy and Process Engineering / Tampere University of Technology, Tampere, Finland, ISBN 951-722-830-9.

/10/ Hinrichsen H. and Wolf D. E. 2004. The Physics of Granular Media. Wiley-VCH Verlag GmbH & Co. KgaA, Weinheim, ISBN 3-527-40373-6.

/11/ Dechsiri, C. 2004. Particle Transport in Fluidized Beds: Experiments and Stochastic Models. Department of Chemical Engineering / University of Groningen, Groningen, The Netherlands, ISBN 90-367-2154-7.

/12/ Valverde, J. M. *et al* 2001. Effect of Vibration on the Stability of Gas-Fluidized Bed of Fine Powder. Physical Review E, Vol. 64, 021302.

/13/ Wassgren, C. R. 1997. Vibration of Granular Materials. Division of Engineering and Applied Science / California Institute of Technology, California, USA.

/14/ Taguchi, Y-h. 1995. Power law velocity fluctuations due to inelastic collisions in numerically simulated vibrated bed of powder. Europhysics Letters, Vol. 30 (8), 499-504.

/15/ Behringer, R. P. *et al* 2002. Granular Friction, Coulomb Failure, and the Fluid-Solid Transition for Horizontally Shaken Granular Materials. Physical Review E, Vol. 65, 031302.

/16/ Knight, J. B. *et al* 1996. Experimental Study of Granular Convection. Physical Review E, Vol. 65, No. 5, 5726.

/17/ Behringer, R. P. *et al* 1996. Granular Solids, Liquids, and Gases. Reviews of Modern Physics, Vol. 68, Issue 4, 1259–1273.

/18/ Umbanhowar, P. 2003. Shaken Sand — a Granular Fluid? Nature, Vol. 424, 21 August 2003, 886–887.

/19/ Feitosa, K. B. 2004. Inelastic Gas: An Experimental Study of Vibro-Fluidized Dilute Granular Media. Department of Physics / University of Massachusetts, Massachusetts, USA.

/20/ Albert, R. *et al* 1999. Slow Drag in a Granular Medium. Physical Review Letters, Vol. 82, 205.

/21/ Finnish Forest Research Institute 2004, Statistical Yearbook of Forestry 2004, Vammalan Kirjapaino Oy, Vammala, Finland, ISBN 951-40-1946-6.

/22/ VTT Technical Research Centre of Finland 2005, Nuclear Energy in Finland, Helsinki, Finland. [e-document retrieved on 20.9.2005 from: http://www.vtt.fi/pro/pro1/ne_finland2005.pdf].

/23/ White, F. M. 1999. Fluid Mechanics, Fourth Edition, McGraw-Hill Inc., Singapore, ISBN 0-07-069716-7.

/24/ Troshko A and Mohan S. 2005. Drag Laws 101, Fluent News, Fluent Inc, Vol. XIV issue 2, Article # 18 – summer 2005.

/25/ Fox, R. W. and McDonald A. T. 1992. Introduction to Fluid Mechanics, Fourth Edition, John Wiley & Sons, Inc., New York, USA, ISBN 0-471-54852-9.

/26/ Trujillo, L. *et al* 2003. Hydrodynamic Model for Particle Size Segregation in Granular Media. Physica A 330, 525 – 548.

/27/ Cull, T. 1999. What is the equation for the lift of a spinning golf ball? Smooth ball? MadSci Network: Physics. [e-document retrieved on 22.9.2005 from: http://www.madsci.org/posts/archives/jun99/928944018.Ph.r.html].

/28/ Brilliantov, N. V. *et al* 1996. Model for collisions in granular gases. Physical Review E Vol. 53, Number 5, 5382 – 5392.

/29/ Motion detector 2 User's Guide, Vernier Software & Technology, Portland Oregon, USA. [e-document retrieved on 26.9.2005 from: http://www2.vernier.com/booklets/md.pdf].

/30/ Shunying J. and Hayley H. S. 2004. Contact Force Models for Granular Flows. Report No. 04-02, Department of Civil and Environmental Engineering / Clarkson University, New York, USA.

/31/ Soleymani A. 2004. Advanced Topics in Deformation and Flow of Dense Gas-Particle Mixtures. Department of Energy and Environmental Technology / Lappeenranta University of Technology, Lappeenranta, Finland, ISBN 951-764-964-9.

/32/ Zhang, X. *et al* 2002. Modeling the Dependence of the Coefficient of Restitution on the Impact Velocity in Elasto-Plastic Collisions. International Journal of Impact Engineering, 27, 317-341.

/33/ Findley. W. N. 1989. Creep and Relaxation of Nonlinear Viscoelastic Materials, Dover Publications, Inc., New York, ISBN 0-486-66016-8.

/34/ Jeng, D. I. 2002. Poroviscosity: A New Constitutive Relation. Department of Geological Sciences / Virginia Polytechnic Institute and State University, Blacksburg, Virginia, USA.

/35/ Swinney, H. L. and Rericha, E. C. 2004. Pattern Formation and Shocks in Granular gases. Proceedings of The International School of Physics Enrico Fermi Course CLV, "The Physics of Complex Systems (new advances and perspectives)." IOS Press, Amsterdam, The Netherlands.

/36/ Jung, J., Gidaspow, D., and Gamwo, I. K. 2005. Measurement of Two Kinds of Granular Temperatures, Stresses, and Dispersion in Bubbling Beds. Industrial & Engineering Chemistry Research, 44, 1329-1341, 2005.

/37/ Aronson, I. 2004. Physics of Granular Matter: Experiment, Theory, Simulations. Materials Science Division, Argonne National Laboratory, Argonne, Illinois USA.

/38/ Jaeger, H. M. *et al* 1995. Granular Convection Observed by Magnetic Resonance Imaging. Science, Vol. 267, 1632-1634.

/39/ Potapov, A. V. and Campbell, C. S. 1996. Propagation of Elastic Waves in Deep Vertically Shaken Particle Beds. Physical Review Letters, Vol. 77, No. 23, 4760-4763.

/40/ Yang, X., Huan, C., and Candela, D. 2002. Measurements of Grain Motion in Dense, Three-Dimensional Granular Fluid. Physical Review Letters, Vol. 88, No. 4, 044301.

/41/ Yang, X., Huan, C., and Candela, D. 2004. NMR Experiemnts on a Three-Dimensional Vibrofluidized Granular Medium. Physical Review E, Vol. 69, 041302.

/42/ Low-*g* and 25-*g* Accelerometers User's Guide, Vernier Software & Technology, Portland Oregon, USA. [e-document retrieved on 14.10.2005 from: http://www2.vernier.com/booklets/lga.pdf, http://www2.vernier.com/booklets/acc.pdf].

/43/ SiLi Type-S glass beads technical data sheet, Sigmund Linder GmbH, Germany. [e-document retrieved on 15.10.2005 from: http://www.sigmund-lindner.com/upload/7033575429_317.pdf].

/44/ Ristow, G. H. 1994. Granular Dynamics: A Review about Recent Molecular Dynamics Simulations of Granular Materials. In: Annual Review of Computational Physics I, 275-308 D. Stauffer (editor). World Scientific, Singapore.

/45/ Evesque, P. and Rajchenbach , J. 1989. Instability in a Sand Heap. Physical Review Letters, Vol. 62, No. 1, 44.

/46/ Miao, G., Huang, K., Yun, Y. and Wei, R. 2004. Active Thermal Convection in Vibrofluidized Granular Systems. The European Physical Journal B, Vol. 40, 301-304.

/47/ Curtiz, J., and Wachem B., 2004. Modeling Particle-Laden Flows: A research Outlook, American Institute of Chemical Engineers Journal, Vol. 50, No. 11, 2638-2645.

/48/ Taguchi, Y-h. 1995. Numerical Study of Granular Turbulence and the Appearance of $k^{-5/3}$ Energy Spectrum without Flow. Physica D, 80, 61-71.

/49/ Wassgren, C. Computer Simulations. Particulate Sciences Laboratory, Purdue University, Indiana, USA. [e-document retrieved on 2.9.2005 from: http://widget.ecn.purdue.edu/~psl/].

/50/ Wassgren, C., Brennen, C. and Hunt, M. 1996. Vertical Vibration of a Deep Bed of Granular Material in a Container. Journal of Applied Mechanics 63, 712–719.

/51/ Xu, B.H. 2003. Modelling of the Gas Fluidization of a Mixture of Cohesive and Cohesionless Particles by a Combined Continuum and Discrete Model. "KONA" Powder Science and Technology in Japan, No.21, 100-108.

/52/ Taghipour, F., Ellis, N. and Wong, C. 2003. CFD Modeling of a Two-Dimensional Fluidized-Bed Reactor. The Eleventh Annual Conference of the CFD Society of Canada, Vancouver, Canada.

/53/ Chiesa, M., Mathiesen, V., Melheim, J. A., and Halvorsen, B. 2005. Numerical Simulation of Particulate Flow by the Eulerian-Lagrangian and Eulerian-Eulerian Approach with Application to Fluidised Bed. Computers and Chemical Engineering, Vol. 29, Issue 2, , 291-304.

/54/ VanWachem, B., Schouten, J., Krishna, R., van den Bleek, C., and Sinclair, J., 2001. Comparative Analysis of CFD Models for Dense Gas-Solid Systems. American Institute of Chemical Engineers Journal, Vol. 47, No. 5, 1035-1052.

/55/ Scheerschmidt, K. Empirical Molecular Dynamics: Possibilities, Requirements, and Limitations. Max Planck Institute of Microstructure Physics, Halle, Germany.

/56/ Fluent, FLUENT 6.2 User's Guide 2005, Fluent Inc., 2005. New Hampshire, USA, www.fluent.com, www.fluentusers.com.

/57/ Coronella, C. J., Cooper, S. 2005 CFD Simulations of Particle Mixing in a Binary Fluidized Bed. Powder Technology, Vol. 151, Issues 1-3, 27-36.

/58/ McIlvenna, P. and Mossad, R. 2003. Third International Conference on CFD in the Minerals and Process Industries. CSIRO, Melbourne, Australia.

/59/ Schwabacher, G. J. 2000. Computational Fluid Dynamics Testing for Drag Reduction of an Aircraft Laser Turret Department Of The Air Force / Air Force Institute Of Technology, Ohio, USA.

/60/ Inman, D. J. 2001. Engineering Vibration, Second Edition, Prentice-Hall, Inc. New Jersey, USA, ISBN 013-0174483.

/61/ Schillemeit, B. and Cucuz, S. 2002. Comparison of Experimental NVH Analysis Techniques on Automotive HVAC Systems. Society of Automotive Engineers (SAE), SAE World Congress, Michigan, USA. ISSN 0148-7191.

/62/ Schwarz, B. J. and Richardson, M. H. 1999. Experimental Modal Analysis. CSI Reliability Week, Florida, USA.

/63/ ANSYS 2005, Release 10.0 Documentation for ANSYS Workbench., Pennsylvania, USA, http://www.ansys.com/.

/64/ Johnson, K. L. 1985 (reprinted 2001). Contact Mechanics, Cambridge University Press, ISBN 0521347963.

/65/ Marcelli, G. 2001. The Role of Three-Body Interactions on the Equilibrium and Non-Equilibrium Properties of Fluids from Molecular Simulation. Swinburne University of Technology. Victoria, Australia.

/66/ Viscosity. [e-document retrieved on 11.1.2006 from: http://en.wikipedia.org/wiki/Viscosity].

/67/ Bordbar, M. H. 2005. Theoretical Analysis and Simulations of Vertically Vibrated Granular Materials. Department of Energy and Environmental Technology / Lappeenranta University of Technology, Finland, ISBN 952-214-161-5.

/68/ Wong, C. 2003. Two Dimensional Modeling of a Fluid Bed. Department of Chemical and Biological Engineering / The University of British Columbia, Vancouver, Canada.

APPENDICES

Appendix 1 *Experimental results for measuring coefficient of restitution by Newton's cradle device*

Name of Test: Steel-Multisize (Large-Medium)

Measurement No.		**Impact Velocity v_{imp} [m/s]**		**Coefficient of Restitution e**	
1		0.809		0.950	
2		1.040		0.946	
3		1.496		0.904	
Material 1	Steel	m_1	18.9 [g]	d_1	16.6 [mm]
Material 2	Steel	m_2	8.9 [g]	d_2	13.0 [mm]

Name of Test: Multisize Steel (Large-Small)

Measurement No.		**Impact Velocity v_{imp} [m/s]**		**Coefficient of Restitution e**	
1		0.790		0.966	
2		1.102		0.8587	
3		1.283		0.839	
Material 1	Steel	m_1	18.9 [g]	d_1	16.6 [mm]
Material 2	Steel	m_2	2.9 [g]	d_2	9.0 [mm]

(continued)

Name of Test: Monosize Steel (Medium-Small)

Measurement No.		**Impact Velocity v_{imp} [m/s]**		**Coefficient of Restitution e**	
1		0.767		0.990	
2		0.970		0.969	
3		1.400		0.95	
Material 1	Steel	m_1	8.9 [g]	d_1	13.0 [mm]
Material 2	Steel	m_2	2.9 [g]	d_2	9.0 [mm]

Name of Test: Steel-Monosize (Large-Large)

Measurement No.		**Impact Velocity v_{imp} [m/s]**		**Coefficient of Restitution e**	
1		0.816		0.985	
2		1.029		0.960	
3		1.515		0.930	
Material 1	Steel	m_1	18.9 [g]	d_1	16.6 [mm]
Material 2	Steel	m_2	18.9 [g]	d_2	16.6 [mm]

(continued)

(Appendix 1 continued)

Name of Test: Coated Steel-Monosize

Measurement No.	**Impact Velocity v_{imp} [m/s]**	**Coefficient of Restitution e**
1	0.767	0.748
2	0.990	0.622
3	1.328	0.575

Material 1	Coated Steel	m_1	31.2 [g]	d_1	21.8 [mm]
Material 2	Coated Steel	m_2	31.1 [g]	d_2	21.8 [mm]

Name of Test: Coated Steel-Multisize (Coated -Large)

Measurement No.	**Impact Velocity v_{imp} [m/s]**	**Coefficient of Restitution e**
1	0.767	0.633
2	1.048	0.590
3	1.268	0.550

Material 1	Coated Steel	m_1	31.2 [g]	d_1	21.8 [mm]
Material 2	Steel	m_2	18.9 [g]	d_2	16.6 [mm]

(continued)

(Appendix 1 continued)

Name of Test: Coated Steel-Multisize (Coated -Medium)

Measurement No.	**Impact Velocity v_{imp} [m/s]**	**Coefficient of Restitution e**
1	0.700	0.645
2	1.010	0.560
3	1.268	0.508

Material 1	Coated Steel	m_1	31.2 [g]	d_1	21.8 [mm]
Material 2	Steel	m_2	8.9 [g]	d_2	13.0 [mm]

Name of Test: Coated Steel-Multisize (Coated -Small)

Measurement No.	**Impact Velocity v_{imp} [m/s]**	**Coefficient of Restitution e**
1	0.740	0.600
2	0.990	0.540
3	1.276	0.495
4	1.520	0.448

Material 1	Coated Steel	m_1	31.2 [g]	d_1	21.8 [mm]
Material 2	Steel	m_2	2.9 [g]	d_2	9.0 [mm]

(continued)

Name of Test: Coated Steel-Multisize (Coated -Large)

Measurement No.	**Impact Velocity v_{imp} [m/s]**	**Coefficient of Restitution e**
1	0.610	0.888
2	1.048	0.800
3	1.284	0.704
4	1.415	0.686

Material 1	Coated Steel	m_1	31.2 [g]	d_1	21.8 [mm]
Material 2	Glass	m_2	14.4 [g]	d_2	22.2 [mm]

Name of Test: Coated Steel-Multisize (Coated -Medium)

Measurement No.	**Impact Velocity v_{imp} [m/s]**	**Coefficient of Restitution e**
1	0.657	0.690
2	1.038	0.616
3	1.358	0.497
4	1.476	0.485

Material 1	Coated Steel	m_1	31.2 [g]	d_1	21.8 [mm]
Material 2	Glass	m_2	5.3 [g]	d_2	15.9 [mm]

(continued)

Name of Test: Coated Steel-Multisize (Coated -Small)

Measurement No.		**Impact Velocity v_{imp} [m/s]**		**Coefficient of Restitution e**	
1		0.520		0.600	
2		0.670		0.520	
3		0.850		0.490	
4		1.090		0.450	
Material 1	Coated Steel	m_1	31.2 [g]	d_1	21.8 [mm]
Material 2	Glass	m_2	1.3 [g]	d_2	10.0 mm

Name of Test: Glass-Multisize (Large-Medium)

Measurement No.		**Impact Velocity v_{imp} [m/s]**		**Coefficient of Restitution e**	
1		0.560		0.970	
2		0.790		0.968	
3		1.291		0.938	
4		1.390		0.920	
Material 1	Glass	m_1	14.3 [g]	d_1	22.2 [mm]
Material 2	Glass	m_2	5.3 [g]	d_2	15.9 [mm]

(continued)

(Appendix 1 continued)

Name of Test: Multisize Glass (Large-Small)

Measurement No.	**Impact Velocity v_{imp} [m/s]**	**Coefficient of Restitution e**
1	0.560	0.947
2	0.863	0.930
3	1.103	0.924

Material 1	Glass	m_1	14.3 [g]	d_1	22.2 [mm]
Material 2	Glass	m_2	1.3 [g]	d_2	10.0 [mm]

Name of Test: Monosize Glass (Medium-Small)

Measurement No.	**Impact Velocity v_{imp} [m/s]**	**Coefficient of Restitution e**
1	0.52	0.965
2	0.792	0.960
3	0.990	0.950
4	1.188	0.940

Material 1	Glass	m_1	5.3 [g]	d_1	15.9 [mm]
Material 2	Glass	m_2	1.3 [g]	d_2	10.0 [mm]

Appendix 2 *ANSYS Workbench simulation results: frequency mode shapes at different friction coefficients.*

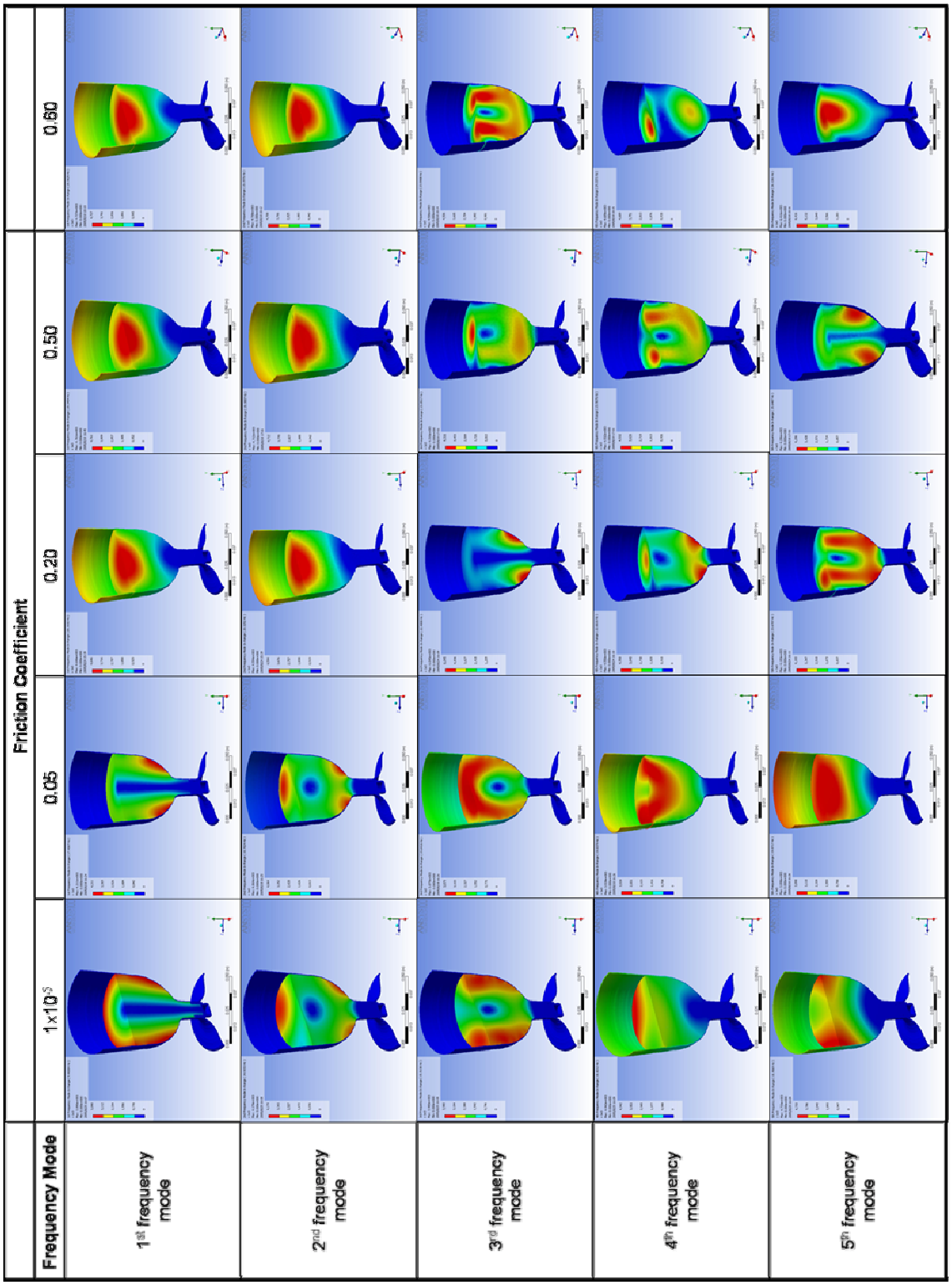

(continued)

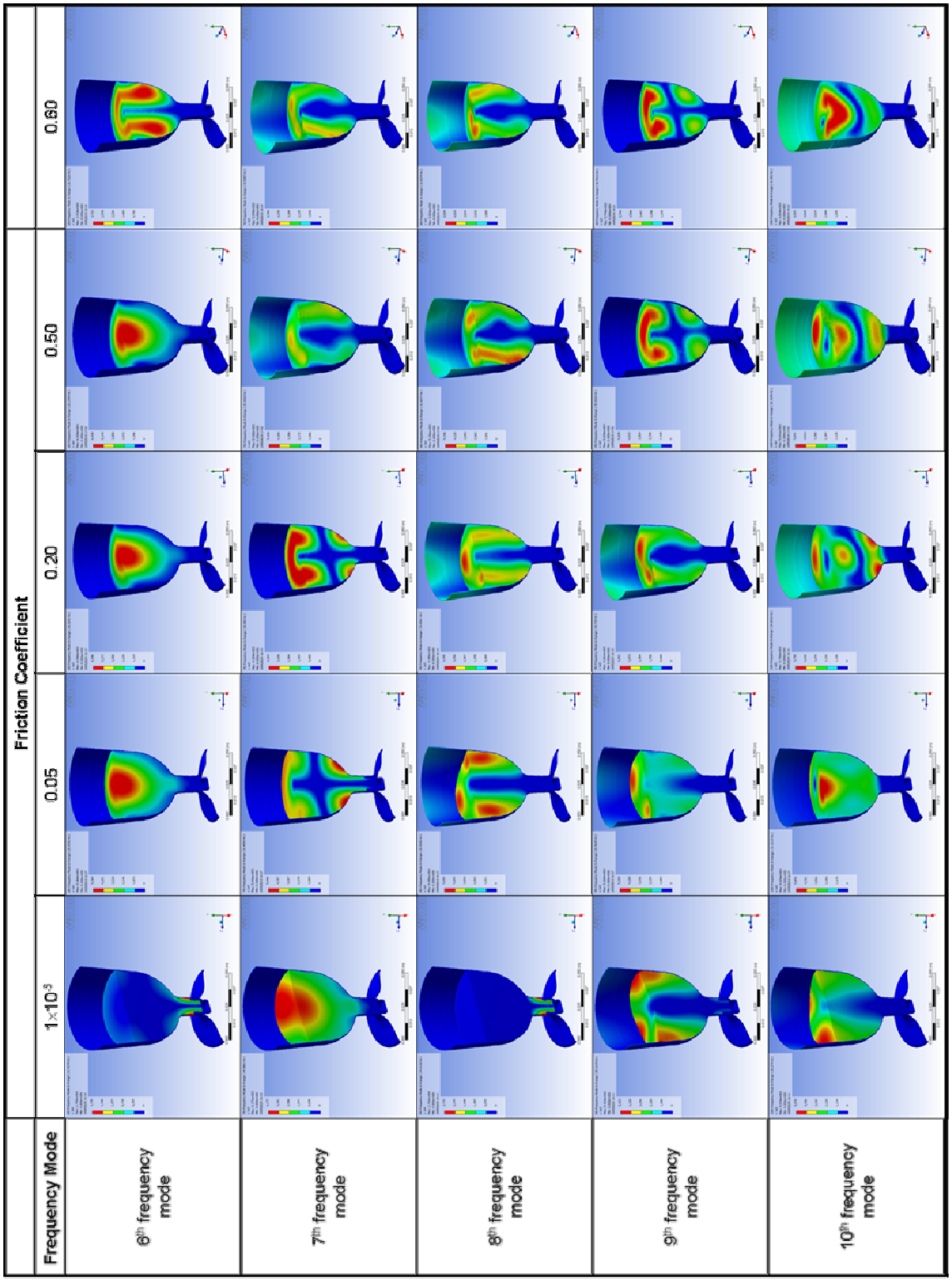
Friction Coefficient
Frequency Mode
1×10⁻³
0.05
0.20
0.50
0.60
6th frequency mode
7th frequency mode
8th frequency mode
9th frequency mode
10th frequency mode

(continued)

(Appendix 2 continued)

	Friction Coefficient				
Frequency Mode	0.75	0.85	0.90	0.95	Rough
1st frequency mode	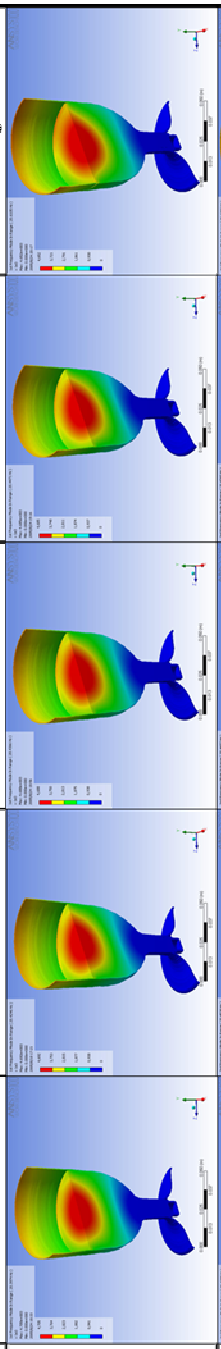				
2nd frequency mode					
3rd frequency mode					
4th frequency mode					
5th frequency mode					

(continued)
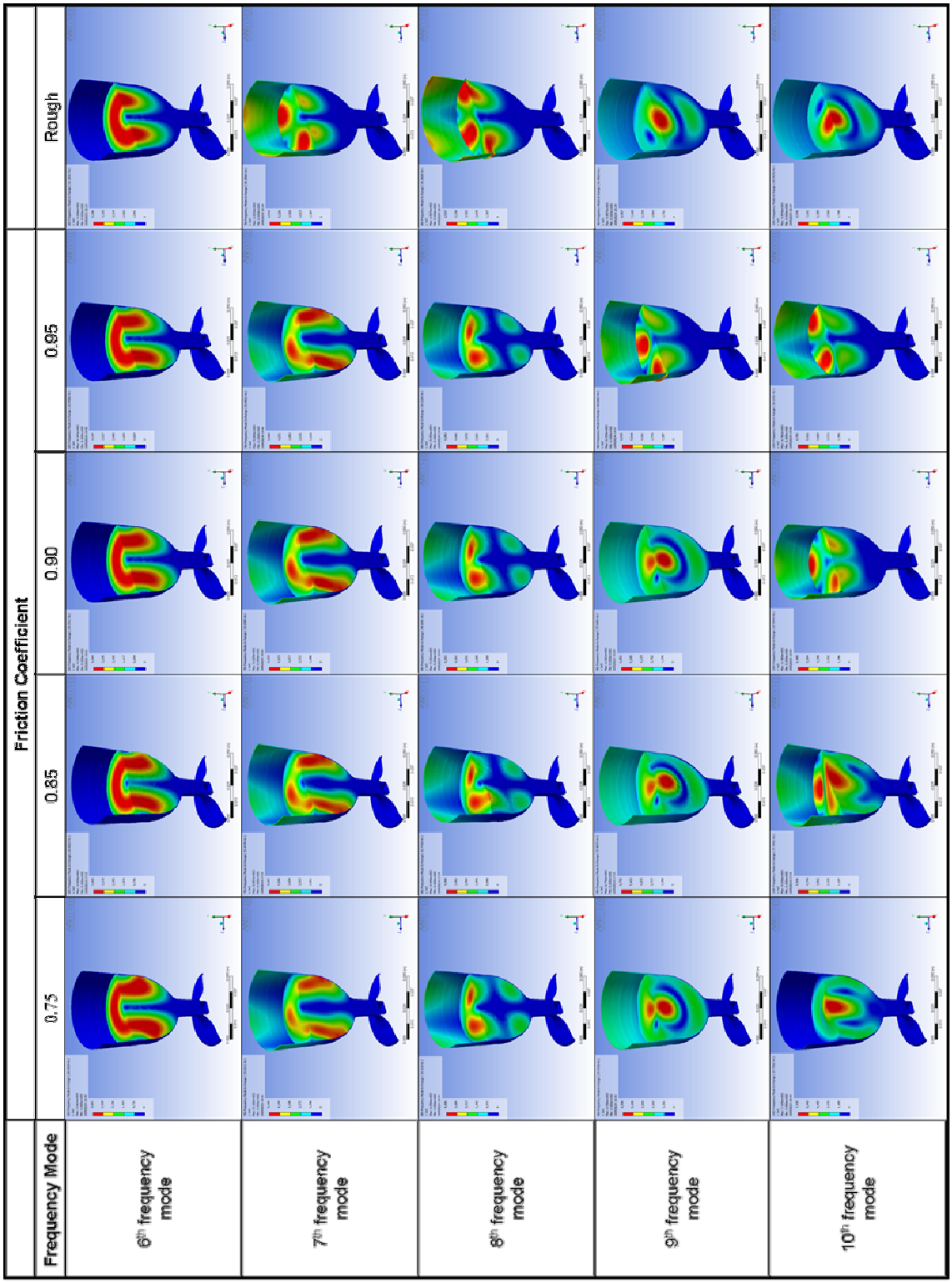
(Appendix 2 continued)